Generation and metrology of ultrashort pulses and their application in attosecond science

Neoricic, Lana

2022

Document Version:
Publisher's PDF, also known as Version of record

Generation and metrology of ultrashort pulses and their application in attosecond science

LANA NEORIČIĆ MACLOT
FACULTY OF ENGINEERING | LUND UNIVERSITY

Generation and metrology of ultrashort pulses and their application in attosecond science

Generation and metrology of ultrashort pulses and their application in attosecond science

by Lana Neoričić Maclot

LUND
UNIVERSITY

Thesis for the degree of Doctor of Philosophy
Thesis advisors: Dr. Cord Louis Arnold, Prof. Anne L'Huillier, Prof. Katalin Varjú
Faculty opponent: Dr. Matteo Lucchini

To be presented, with the permission of the Faculty of Engineering, LTH of Lund University, for public criticism in the Rydberg lecture hall (Rydbergsalen) at the Department of Physics) on Friday, the 10th of June 2022 at 9:15.

Organization	Document name
LUND UNIVERSITY Department of Physics Box 124 SE–221 00 LUND Sweden	**DOCTORAL DISSERTATION** Date of disputation 2022-06-10 Sponsoring organization
Author(s) Lana Neoričić Maclot	

Title and subtitle

Generation and metrology of ultrashort pulses and their application in attosecond science

Abstract

This thesis deals with the dynamical processes in atoms and small molecules initiated by the absorption of ultrashort, coherent light pulses. The studied phenomena take place on the femtosecond (1 fs $= 10^{-15}$ s) and attosecond (1 as $= 10^{-18}$ s) time-scales and critically depend on the properties of the light fields that drive them. We work with infrared (IR) femtosecond laser pulses, which we manipulate through non-linear interactions with matter to either study these interactions themselves or apply them to investigate other light-induced processes.

One part of this thesis focuses on the generation and characterisation of IR pulses spectrally broadened through the Kerr effect. We use a technique called dispersion scan to temporally compress and at the same time measure pulses broadened in gas-filled hollow-core fibres. We propose multiple improvements to this well-established characterisation technique. Further, we investigate femtosecond filamentation in gases, a process with highly complex dynamics involving several non-linear processes including the Kerr effect and ionisation. We develop a method that allows us to measure the electric field of a laser pulse undergoing filamentation in three dimensions, while also scanning along the filament length. Our technique provides access to pulses with desirable characteristics that may be generated at a point inside the filament, simultaneously enabling their measurement and extraction for applications. In addition, this technique opens up the possibility to explore intricate filament dynamics.

In the other part of this work, we up-convert the IR laser pulses into trains of extreme ultraviolet (XUV) attosecond pulses through a non-linear process called high-order harmonic generation. We combine the IR and XUV pulses to study the photoionisation dynamics in different species using a method known as RABBIT (Reconstruction of Attosecond Beating By Interference of Two-photon transitions). In this technique, a target gas is ionised by the XUV field, creating an electron wave-paket (EWP) in the continuum, while a weak IR pulse probes the system. The EWP scatters off the ionic potential, acquiring an additional phase as it propagates. Recording the photoelectron spectrum as a function of the IR-XUV time delay allows us to infer time-resolved information about the ionic potential. We apply this method to investigate the dynamics of different ionisation processes in noble gases (He, Ar, and Xe) and the N_2 molecule. The high spectral resolution of our electron spectrometer allows us to disentangle the contributions from different ionisation channels. In addition, we perform angle-resolved measurements, investigating the coherent superposition of final states with different angular momenta.

Key words

ultrashort, femtosecond, filamentation, dispersion scan, RABBIT, photoionisation, attosecond, interferometry, pump-probe, spectroscopy, photoelectron, wavepacket

Classification system and/or index terms (if any)

Supplementary bibliographical information	Language
	English
ISSN and key title 0281-2762	ISBN 978-91-8039-274-7 (print) 978-91-8039-273-0 (pdf)
Recipient's notes	Number of pages 199 / Price
	Security classification

Generation and metrology of ultrashort pulses and their application in attosecond science

by Lana Neoričić Maclot

LUND
UNIVERSITY

A doctoral thesis at a university in Sweden takes either the form of a single, cohesive research study (monograph) or a summary of research papers (compilation thesis), which the doctoral student has written alone or together with one or several other author(s).

In the latter case the thesis consists of two parts. An introductory text puts the research work into context and summarizes the main points of the papers. Then, the research publications themselves are reproduced, together with a description of the individual contributions of the authors. The research papers may either have been already published or are manuscripts at various stages (in press, submitted, or in draft).

Cover illustration front: Atomic orbitals with n=1-4, l=0-2, m=0-2.

Funding information: The thesis work was financially supported by the Swedish Research Council, LaserLab Europe, European Research Council, and Knut and Alice Wallenberg Foundation.

Department of Physics, Faculty of Engineering, LTH, Lund University

ISBN: 978-91-8039-274-7 (print)
ISBN: 978-91-8039-273-0 (pdf)

Printed in Sweden by Media-Tryck, Lund University, Lund 2022

Media-Tryck is a Nordic Swan Ecolabel certified provider of printed material. Read more about our environmental work at www.mediatryck.lu.se

Printed matter 3041 0903

MADE IN SWEDEN

Abstract

This thesis deals with the dynamical processes in atoms and small molecules initiated by the absorption of ultrashort, coherent light pulses. The studied phenomena take place on the femtosecond (1 fs $= 10^{-15}$ s) and attosecond (1 as $= 10^{-18}$ s) timescales and critically depend on the properties of the light fields that drive them. We work with infrared (IR) femtosecond laser pulses, which we manipulate through non-linear interactions with matter to either study these interactions themselves or apply them to investigate other light-induced processes.

One part of this thesis focuses on the generation and characterisation of IR pulses spectrally broadened through the Kerr effect. We use a technique called dispersion scan to temporally compress and at the same time measure pulses broadened in gas-filled hollow-core fibres. We propose multiple improvements to this well-established characterisation technique. Further, we investigate femtosecond filamentation in gases, a process with highly complex dynamics involving several non-linear processes including the Kerr effect and ionisation. We develop a method that allows us to measure the electric field of a laser pulse undergoing filamentation in three dimensions, while also scanning along the filament length. Our technique provides access to pulses with desirable characteristics that may be generated at a point inside the filament, simultaneously enabling their measurement and extraction for applications. In addition, this technique opens up the possibility to explore intricate filament dynamics.

In the other part of this work, we up-convert the IR laser pulses into trains of extreme ultraviolet (XUV) attosecond pulses through a non-linear process called high-order harmonic generation. We combine the IR and XUV pulses to study the photoionisation dynamics in different species using a method known as RABBIT (Reconstruction of Attosecond Beating By Interference of Two-photon transitions). In this technique, a target gas is ionised by the XUV field, creating an electron wave-paket (EWP) in the continuum, while a weak IR pulse probes the system. The EWP scatters off the ionic potential, acquiring an additional phase as it propagates. Recording the photoelectron spectrum as a function of the IR-XUV time delay allows us to infer time-resolved information about the ionic potential. We apply this method to investigate the dynamics of different ionisation processes in noble gases (He, Ar, and Xe) and the N_2 molecule. The high spectral resolution of our electron spectrometer allows us to disentangle the contributions from different ionisation channels. In addition, we perform angle-resolved measurements, investigating the coherent superposition of final states with different angular momenta.

Popular science summary

Measuring time is the first step to controlling the course, and eventually the outcome, of a process. The need to measure time has been essential to humans for as long as we have existed. Our hunter-gatherer ancestors' survival depended on their ability to predict how much food should be stored for winter, agrarian societies needed to know when to start ploughing their soil, whereas the industrial era brought about intricate mechanisation that required precise synchronisation. Scientific developments of the twentieth century have vastly expanded our possibilities in the field of time metrology. For events far longer than a human lifetime, we now use indirect methods such as measuring the redshift of star light to estimate the age of the universe or radiocarbon dating to determine when the last ice age ended. Events on time scales perceivable by humans, on the other hand, are measured directly, using a stopwatch of some sort. Atomic clocks provide the basis for a standardised definition of a time unit. Their accuracy, combined with the knowledge of the theory of relativity, allows us to synchronise GPS satellites and navigate the Earth, as well as space.

As we seek to observe faster-evolving processes, we become limited by the response time of the apparatus used for observation. Human eyes can resolve events spaced by 15 milliseconds at most, which is why high-definition videos operate at a rate of 60 frames per second. Cameras help us record faster events; scientists can take one image of a frog every millisecond to determine how it uses its muscles to leap and land. If, however, we wish to attach a camera to a microscope and see how a single base replicates in the DNA strand of E. coli, we will be disappointed to learn that, within the time it takes the camera to acquire an image, the entire base-copying process has already taken place. One can then think of applying a stroboscopic method by synchronising a flash of light with the same camera. That way, even though the image acquisition time is one millisecond, the DNA base is exposed for only a fraction of that time, so we now have insight into a short step of the replication event. Finally, if we take a series of images while controlling the delay of the flash with respect to the beginning of the replication, we will end up with a movie showing the sequence of steps we wanted.

This thesis deals with the exploration of even faster events. Belonging to a field today known as *ultrafast science*, it revolves around the observation of electrons as they leave the atom they used to be bound to, kicked out by a high-energy photon. The movement of the outgoing electron forces the remaining electrons out of equilibrium, making them rearrange into a new stable state very fast. Studying this process, called *photoionisation*, provides us with knowledge about how atoms behave. The grand goal would be to earn an amount of understanding that would enable us to *control* this behaviour, thereby influencing the course of chemical reactions and other atomic-scale

processes that ultimately govern the macroscopic world.

Observing the said electron rearrangement requires attosecond imaging resolution ($1\,\text{as} = 10^{-18}\,\text{s}$). A great illustration of this time scale famously states that one attosecond compares to a second the same way a second compares to the age of the universe. In order to trace such unfathomably fast motion, we, scientists, use the stroboscopic method in what we call the *pump-probe* technique. The idea is to use a high-frequency light pulse that we refer to as a "pump" to initiate the photoionisation, while we introduce another pulse at a variable delay to probe the process. For this we need very intense and short pulses, which can only be produced by lasers. State-of-the-art lasers currently deliver infrared (IR) pulses in the femtosecond ($1\,\text{fs} = 10^{-15}\,\text{s} = 1000\,\text{as}$) range, which can be converted into extreme ultraviolet (XUV) attosecond pulses or pulse trains through a process known as *high-order harmonic generation*. Despite the advantage that their short duration has for the temporal resolution of the experiment, these XUV pulses are very weak and hard to manipulate. We therefore most often use them only for the pump, and instead use IR laser pulses to probe the atom at different delays.

The work presented in this thesis concerns three experimental aspects of photoionisation studies: *(i)* using optical processes to tailor laser pulses for different applications, *(ii)* reliable and complete characterisation of these pulses, and *(iii)* combining IR and XUV pulses in a pump-probe scheme to study the photoionisation dynamics of different atoms and molecules. The pieces of work concerning pulse modification and metrology are of technical nature. They propose improvements of existing techniques or ideas of how to combine them in a novel way and thus extend their applicability to new objects of study. The pump-probe experiments, on the other hand, use well-established protocols to disentangle the photoionisation dynamics of atoms or molecules in very specific conditions. As a rule, these studies all required some development of the models used to interpret the experimental data, ever so slightly pushing the boundaries of what we know about how matter reacts to light.

Populärvetenskaplig sammanfattning

Att mäta tiden är det första steget för att styra riktingen, och slutligen resultatet, av en process. Behovet för tidsmätning har varit essentiellt för mänskligheten så länge vi har existerat. Överlevnaden av våra jägar- och samlar-förförfäder var beroende av deras förmåga att förutse hur mycket mat som borde ha samlats in inför vintern, jordbrukar samhällen behövde veta när man borde börja plöja jorden, medans den industriella eran medförde en invecklad automatisering som krävde en mycket nogrann synkronisering. Under 1900-talet har de vetenskapliga bedrifterna kraftigt utvecklat våra möjligheten inom tidsmetrologi. För händelser som långt överstiger människans livspann, använder vi idag indirekta metoder så som beräkning av Hubbles konstant för att bestämma åldern på vårt universum eller genom användandet av kol-14-metoden för att avgöra när den senaste istiden avslutades. Dock för händelser som sker på en tidskala som är begriplig för människan, kan de direkt mätas med hjälp av ett stoppur. Där atomur är grunden för att definiera en standardenhet av tid. Vars noggrannhet, i kombination med kunskapen om relativeitets teorin, tillåter oss att synkronisera GPS satelliter och navigera runt jorden, och rymden likväl.

När vi försöker att observera allt mer snabb-utvecklade processer, blir vi dock begränsade av svarstiden på apparaten som används vid observationen. Människans öga kan endast urskilja händelser som är separerade med max 15 millisekunder, vilket är varför hög-upplösta kameror har en bildfrekvens på 60 bilder per sekund. Kameror hjälper oss att registrera allt snabbare händelser; genom att ta en bild varje millisekund kan vetenskapsmän fastställa hur en groda använder benmusklerna för att hoppa och landa. Om vi, genom att fästa en kamera på ett mikroskop, vill undersöka hur en enskild bas i E. colis DNA replikeras, blir vi besvikna när de visar sig att, under tiden som kameran införskaffar sig bilden, har hela baskopieringsprocessen redan skett. Man kan sedan tänka sig att applicera en stroboskopisk metod genom att synkronisera en ljusblixt med samma kamera. På detta sätt, även om bilden är tagen under loppet av en millisekund, har DNA basen endast blivit exponerat en bråkdel av denna tid, så att vi nu har en inblick över en kort del av händelseförloppet för replikationsprocessen. Till sist, om vi tar en serie av bilder samtidigt som fördröjningen mellan ljusblixten och starten av replikationsprocessen kontrolleras, slutar vi upp med en film som illustrerar det eftersöta händelseförloppet i en red av korta sekvenser.

Denna avhandling är centrerad kring observationer av elektroner när de lämnar den atom de tidigare var bunden till, utknuffade av högenergiska fotoner. Den utknuffade elektronens rörelse tvingar de kvarvarande elektronerna ur jämnvikt, varpå de snabbt måste omordnas till ett nytt stabilt tillstånd. Vid studerandet av denna process, kallad *fotojonisering*, får vi tillgång till information om hur atomerna agerar. Där det slutgiltiga målet är att samla tillräckligt mycket förståelse så att möjligheter för att

kontrollera detta fenomen öppnas, därigenom influera vägen kemiska reaktioner och andra processer på en atomär skala tar, som slutligen styr den makroskopiska världen.

För att observera omordningen av elektronerna krävs attosekundsbildupplösning (1 as = 10^{-18} s). En väldigt bra och illustrativ förklaring på denna tidskala förtydligar hur en attosekund skalas till en sekund på samma sätt som en sekund skalas till åldern av vårt universum. För att, vi forskare skall, kunna spåra sådana ofattbart snabba rörelser, använder vi de stroboskopiska metoder som kallas för *pump-probe* tekniker. Idéen är att använda en högfrekvent ljuspuls som vi kallar ”pump” för att starta fotojoniseringen, medans vi introducerar en annan puls för att sondera processen med en kontrollerad fördröjning. För att åstadkomma detta behöver vi väldigt intensiva och kortvariga pulser, vilket endast kan bli producerat via lasrar. Toppmoderna lasrar producerar för närvarande infraröda (IR) pulser under ett femtosekundsintervall (1 fs = 10^{-15} s = 1000 as), vilket kan konverteras till extrem-ultravioletta (XUV) attosekundsljuspulser eller attosekundspulståg genom en process känd som *generering av harmoniska övertoner* (på engelska: *high-order harmonic generation - HHG*) . Trots de fördelar för tidsupplösningen av experiment som följer av kortvariga pulser, är dessa XUV-pulser väldigt svaga och svåra att manipulera. Vi använder därför endast dem för pumpen, och istället använder IR pulserna för att sondera atomen med olika fördröjningar.

I denna avhandling presenteras arbete som berör tre olika experimentella aspekter av fotojoniseringsstudier: *(i)* användandet av optiska processer för att skräddarsy laserpulser för olika applikationer, *(ii)* tillförlitlig och komplett karakterisering av dessa pulser, samt *(iii)* att kombinera IR- och XUV-pulserna i en pump-probe arrangemang för att studera fotojoniseringsdynamiken i olika atomer och molekyler. Den del av arbetet som berör pulsemodifiering och metroligi är av teknisk natur. De föreslår förbättringar på redan existerande tekniker eller idéer på hur man kan kombinera dem på ett originellt sätt och därmed utöka möjliga applikationer för att studera nya områden. Pump-probe experimenten använder dock väletablerade protokoll för att särskilja fotojoniseringsdynamiken i atomer och molekyler under väldigt specifika omständigheter. I regel, kräver forskning generellt någon form av utveckling av de befintliga modeler som används för att tolka experimentell data, och därmed, om än så lite, utökas gränsen kring vad som redan är känt om hur materia påverkas av ljus.

List of publications

This thesis is based on the following publications:

I **Fast iterative retrieval algorithm for ultrashort pulse characterization using dispersion scans**
M. Miranda, J. Penedones, C. Guo, A. Harth, M. Louisy, **L. Neoričić**, A. L'Huillier, and C. L. Arnold
Journal of the Optical Society of America B 34, 1 (2017)

II **Compact single-shot d-scan setup for the characterization of few-cycle laser pulses**
M. Louisy, C. Guo, **L. Neoričić**, S. Zhong, A. L'Huillier, C. L. Arnold, and M. Miranda
Applied Optics 56, 32 (2017)

III **All-optical measurement of the complete waveform of octave-spanning ultrashort light pulses**
M. Miranda, F. Silva, **L. Neoričić**, C. Guo, V. Pervak, M. Canhota, A. S. Silva, Í. J. Sola, R. Romero, P. T. Guerreiro, A. L'Huillier, C. L. Arnold, and H. Crespo
Optics Letters 44, 2 (2019)

IV **Attosecond timing of electron emission from a molecular shape resonance**
S. Nandi, E. Plésiat, S. Zhong, A. Palacios, D. Busto, M. Isinger, **L. Neoričić**, C. L. Arnold, R. J. Squibb, R. Feifel, P. Decleva, A. L'Huillier, F. Martín, and M. Gisselbrecht
Science Advances 6 (2020)

V **Attosecond electron–spin dynamics in Xe 4d photoionization**
S. Zhong, J. Vinbladh, D. Busto, R. J. Squibb, M. Isinger, **L. Neoričić**, H. Laurell, R. Weissenbilder, C. L. Arnold, R. Feifel, J. M. Dahlström, G. Wendin, M. Gisselbrecht, E. Lindroth, and A. L'Huillier
Nature Communications, 11 (2020)

VI **Attosecond photoionization dynamics in the vicinity of the Cooper minima in argon**
C. Alexandridi, D. Platzer, L. Barreau, D. Busto, S. Zhong, M. Turconi, **L. Neoričić**, H. Laurell, C. L. Arnold, A. Borot, J.-F. Hergott, O. Tcherbakoff, M. Lejman, M. Gisselbrecht, E. Lindroth, A. L'Huillier, J. M. Dahlström, and P. Salières
Physical Review Research 3 (2021)

VII **4D spatio-temporal characterization of ultrashort light pulses undergoing filamentation**
L. Neoričić*, C. Jusko*, S. Mikaelsson, C. Guo, M. Miranda, S. Zhong, F. Garmirian, B. Major, J. M. Brown, M. Gaarde, A. Couairon, U. Morgner, M. Kovačev, and C. L. Arnold,
*these authors contributed equally
Submitted manuscript

VIII **Resonant two-photon ionisation of helium atoms studied by attosecond interferometry**
L. Neoričić, D. Busto, H. Laurell, R. Weissenbilder, M. Ammitzböll, S. Luo, J. Peschel, H. Wikmark-Kreuger, J. Lahl, S. Maclot, R. J. Squibb, S. Zhong, P. Eng-Johnsson, C. L. Arnold, R. Feiffel, M. Gisselbrecht, E. Lindroth, and A. L'Huillier
Manuscript in preparation

Related publications by the author, not included in this thesis:

Saddle point approaches in strong field physics and generation of attosecond pulses
A. Nayak, M. Dumergue, S. Kühn, S. Mondal, T. Csizmadia, N.G. Harshith, M. Füle, M. Upadhyay Kahaly, B. Farkas, B. Major, V. Szaszkó-Bogár, P. Földi, S. Majorosi, N. Tsatrafyllis, E. Skantzakis, **L. Neoričić**, M. Shirozhan, G. Vampa, K. Varjú, P. Tzallas, G. Sansone, D. Charalambidis and S. Kahaly
Physics Reports 388 (2019)

Studying ultrafast Rabi dynamics with a short-wavelength seeded free-electron laser
S. Nandi, E. Olofsson, M. Bertolino, S. Carlström, F. Zapata, D. Busto, C. Callegari, M. Di Fraia, P. Eng-Johnsson, R. Feifel, G. Gallician, M. Gisselbrecht, S. Maclot, **L. Neoričić**, J. Peschel, O. Plekan, K. C. Prince, R. J. Squibb, S. Zhong, P. V. Demekhin, M. Meyer, C. Miron, L. Badano, M. B. Danailov, L. Giannessi, M. Manfredda, F. Sottocorona, M. Zangrando and J. M. Dahlström
Submitted manuscript, arXiv: 2201.10950

Continuous variable quantum state tomography of photoelectrons

H. Laurell, D. Finkelstein-Shapiro, C. Dittel, C. Guo, R. Demjaha, M. Ammitzböll, R. Weissenbilder, **L. Neoričić**, S. Luo, M. Gisselbrecht, C. L. Arnold, A. Buchleitner, T. Pullerits, A. L'Huillier, and D. Busto
Submitted manuscript, arXiv: 2202.06798

List of abbreviations

AMO	atomic, molecular, and optical (physics)
AOPDF	acousto-optical programmable dispersive filter (*Dazzler*)
CAMP	chamber for atomic and molecular physics
cc	continuum-continuum
CCD	charge-coupled device
CM	chirped mirror
d-scan	dispersion scan
EWP	electron wavepacket
FTL	Fourier-transform limit(ed)
HHG	high-order harmonic generation
IR	infrared
MBES	magnetic bottle electron spectrometer
MCP	micro-channel plate
PAD	photoelectron angular distribution
PES	photoelectron spectrum
RABBIT	reconstruction of attosecond beating by interference of two-photon transitions
RPAE	random phase approximation with exchange
SB	sideband
SHG	second harmonic generation
S-O	spin-orbit [splitting]
STC	spatio-temporal coupling
THG	third harmonic generation
Ti:Sa	titanium:sapphire
VMIS	velocity-map imaging spectrometer
XUV	extreme ultraviolet
3/4D	three/four-dimensional

Contents

Chapter 1

Introduction

1.1 Studying electron dynamics of photoionisation on their natural time-scale

Charge redistribution within atoms and molecules governs the macroscopic world through chemical reactions. It is therefore of immense interest to understand and learn to control atomic-scale charge dynamics. To find out what kind of tools we need to tackle this task, we must first determine how fast these dynamics are. Quantum mechanics provides a very simple expression for the time scale of inter-atomic processes:

$$\Delta t \sim \hbar/\Delta E, \tag{1.1}$$

where ΔE is the spacing between the energy levels characteristic of the observed process and $\hbar$ is the Planck constant. As an illustration, the ro-vibrational energy level spacing in molecules lies in the millielectronvolt (meV) range, whereas the electronic level spacing in atoms is typically several electronvolts. In consequence, chemical reactions and phase transitions take place on the femtosecond ($1\,\text{fs} = 10^{-15}\,\text{s}$) time scale. In case of photoionisation, one of the two primary subjects of this thesis, ΔE corresponds to the ionisation potential and ranges from $1-100$ eV, requiring attosecond ($1\,\text{as} = 10^{-18}\,\text{s}$) resolution to be properly observed in time.

A well-established way to experimentally achieve this is to employ a so-called *pump--probe* scheme, where one short laser pulse initiates the dynamics (colloquially, to *"pump"* the system) and a second one is sent at a variable delay to probe the system at different stages of its evolution. This approach was initially applied using two delayed

femtosecond pulses to analyse transition states in chemical reactions, marking the beginning of femtochemistry[1]. Conceived in the 1980's by Ahmed Zewail, it was soon recognised as a technique with an enormous potential and Zewail was awarded the Nobel prize in chemistry in 1999. In parallel with the development of femtochemistry, non-linear optics was taking a huge turn, discovering a way of generating coherent light pulses in the sub-femtosecond regime using table-top setups*. Late 1980's thus also saw the invention of high-order harmonic generation (HHG)[2,3], a non-linear up-conversion process transforming infrared (IR) laser pulses into coherent extreme ultraviolet radiation (XUV). Its spectral composition was proven to support attosecond light bursts in 2001[4]. As such, HHG is capable of securing the resolution needed to disentangle electron dynamics of photoionisation in pump-probe experiments.

Among several complementary techniques[5], this thesis presents a pump-probe method called RABBIT (short for reconstruction of attosecond beating by interference of two-photon transitions, sometimes also cited as RABITT), invented in 2001, where a laser pulse is split in two so as to simultaneously provide a femtosecond IR probe and, through HHG, an XUV pump consisting of multiple attosecond pulses[4,6]. Over the past two decades, this technique has been thoroughly tested and successfully applied in a number of photoionisation dynamics studies in atoms[7,8,9,10,11,12], molecules[13,14,15,16], and solids alike[17,18].

1.2 Tailoring light

In thinking about pump-probe experiments (or any other spectroscopic scheme, for that matter), a very important question naturally comes to mind: to what extent can we control the light we apply? Being a non-linear process, HHG critically depends on the parameters of the driving laser pulses. Ideally, one would want to shape them at will, adapting their duration and spectrum to the needs of different experiments. While removing spectral content can often be achieved relatively simply in the IR-visible domain (using filters or mechanically blocking parts of a beam dispersed by a grating), the opposite requires frequency conversion through a non-linear process. The most straightforward way to spectrally broaden intense ultrashort pulses is to force self-phase modulation, a non-linear effect where a pulse propagating through a medium experiences an intensity-dependent refractive index, resulting in the generation of new frequencies. This thesis discusses experimental implementations of this idea, most of which rely on pulse confinement in a gas-filled waveguide. A special focus is given to the notable exception: the technique called *femtosecond filamentation*, where pulse propagation is self-guided. The dynamics involved in the filamentation

*as opposed to large-scale facilities producing high-brilliance X-ray radiation: synchrotrons, which had already long been in operation, or free-electron lasers.

process are rather rich and complex, making it a very interesting, albeit challenging object of study.

In order to optimise a pulse, one first needs to accurately characterise it and understand what kind of correction can be applied to make it better suited for the given purpose. This task is rather arduous in the femtosecond domain due to the fact that detection devices capable of providing direct real-time response to the electric field do not (currently) exist. The way of overcoming this issue is to engage the pulse of interest in some sort of non-linear interaction with a material and observe the ensuing optical response. Owing to the fact that non-linear processes are highly sensitive to the driving pulse characteristics (spectral intensity and especially phase), the latter can be deduced from the measured response signal by numerical pulse-retrieval algorithms based on models of the interaction. A number of femtosecond laser pulse diagnostic techniques have been proposed [19]. This thesis focuses on the dispersion scan (d-scan), a method for inferring the spectral phase of a pulse by analysing the signal of its second harmonic, generated while varying the amount of dispersion that the measured pulse experiences. Compact, robust, fast, and modular, it offers a means of direct feedback for laser pulse optimisation.

1.3 Scope of this work

This thesis has two main directions: *(i)* ultrashort IR pulse generation and metrology, and *(ii)* generation and application of trains of attosecond XUV pulses for photoionisation studies.

Along the first direction, effort has been made to further improve the existing d-scan pulse characterisation technique. In Article I, we introduce a novel pulse retrieval algorithm that converges significantly faster than the previously proposed ones. We test it against pulses from two different sources and prove its robustness for cases of faulty measurements. In Article II, we propose an innovative geometry for the single--shot variant of d-scan, making the design simpler and more compact compared to its predecessor. Article III presents an extension of the d-scan technique for octave-spanning pulses only, where we demonstrate the first d-scan-based retrieval of the complete electric field of the pulse, including the offset between the field and the pulse envelope.

Further work on ultrashort pulse metrology was done within the scope of a project concerning a comprehensive characterisation of a femtosecond filament. Unlike numerous previous experiments, this study succeeds to capture the electric field of the filamenting pulse in all three dimensions, while also scanning along the filament length. The presented technique allows the study of otherwise elusive filament dynamics in

an unprecedented amount of detail. This work is summarised in Article VII.

The second subject of the thesis revolves around electron correlations initiated by photoionisation. In Article IV we use RABBIT to point at the limits of the Franck-Condon principle, which states that molecular nuclei can be considered motionless during electronic transitions. We do so by probing vibrationally resolved photoionisation time delays in molecular nitrogen caused by transient electron trapping in the $3\sigma_g^{-1}$ shape resonance, demonstrating that the distance between the nuclei indeed changes as the electron makes its way out of their potential. Article V presents a study of photoionisation from the $4d$ shell in xenon. Using RABBIT, we measure the time delay between phootoelectrons corresponding to two spin-orbit split states of the Xe^+ ion over a large energy range. Using time-frequency analysis, we disentangle two interfering ionisation mechanisms: a spectrally broad, short-lived giant dipole resonance, and a narrow resonance close to the $4d$ ionisation threshold, brought about by spin--flip transitions. Article VI summarises a study of photoionisation around the so-called Cooper minima in argon, where the partial ionisation cross-section for either available angular channel experiences a local minimum. We measure the delay between electrons from the 3s and 3p shells and identify the presence of strong shake-up processes that need to be taken into account to numerically model the 3s-3p delay. Finally, in Article VIII, we study resonant two-photon ionisation via the $1s3p$, $1s4p$, and $1s5p$ Rydberg states of helium. Using a velocity-map imaging spectrometer to record the photoelectron angular distribution, and a magnetic bottle electron spectrometer for high-energy-resolution measurements, we disentangle the interplay between the *s* and *d* angular ionisation channels.

The organisation of this thesis is the following. Chapter 2 explains the process of high-order harmonic generation and discusses the spectral and temporal properties of the resulting attosecond pulse trains. Chapter 3 begins with a description of ultrashort pulses capable of driving HHG, followed by an introduction to their interaction with matter. The emphasis is on processes involved with spectral broadening, particularly on femtosecond filamentation. The last part of Chapter 3 is dedicated to ultrashort pulse metrology and presents our results on spectro-temporal pulse reconstruction using d-scan (Articles I-III) and four-dimensional filament characterisation (Article VII). The focus of the thesis then shifts towards laser-assisted photoionisation, Chapter 4 providing the necessary theoretical framework and presenting the relevant experimental apparatus. Chapter 5 deals with photoionisation dynamics, introducing the concept of photoionisation time delays and presenting the results of experiments on N2 (Article IV), Xe (V), Ar (VI), and He (VIII), conducted in the course of this thesis. Finally, Chapter 6 gives a summary of the presented work and offers a perspective on future research.

Chapter 2

High-order harmonic generation

As mentioned in Chapter 1, resolving atomic or molecular electron dynamics requires the use of light pulses with below-femtosecond duration. Given that time and frequency represent a Fourier pair, the minimal duration of a light pulse is determined by its bandwidth. This property can be conveniently quantified using the time-bandwidth product, specific to the shape of the spectral density function: for example,

$$\mathrm{TBP}_{\mathrm{Gauss}} = \Delta\nu\Delta\tau = 0.44 \tag{2.1}$$

This simple formula expresses the fact that reaching attosecond pulse durations entails making use of the extreme ultraviolet (XUV) spectral region since a longer-wavelength carrier could not support the required bandwidths.

Table-top sources of coherent radiation extending into the XUV region are based on a frequency-upconversion technique called high-order harmonic generation (HHG) [2,3]. In this technique, a high-power laser beam is focused into a rare gas target *, leading to the generation of high-order odd harmonics of the fundamental field frequency. Unlike the low-order parametric frequency upconversion processes (second and third harmonic generation), where the radiation intensity exponentially falls off with the harmonic order, HHG produces an output spectrum where the initial intensity decrease is followed by a plateau that can extend over tens of harmonics before exhibiting a final sharp drop towards the cut-off frequency (see Fig. 2.1). This makes it clear that HHG cannot be treated within the perturbative framework like its low-order counterparts.

*The technique has recently been extended to solid [20] and liquid [21] targets.

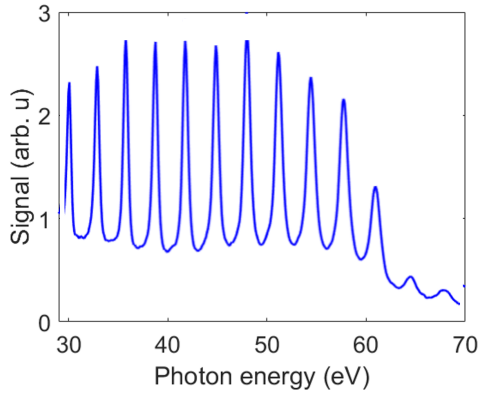

Figure 2.1: Experimental HHG spectrum. A plateau region, featuring approximately constant conversion efficiency, is followed by a sharp efficiency-drop called cut-off. The lowest-order harmonics, which exhibit perturbative behaviour, are rarely used in experiments and are thus usually not recorded.

2.1 The single-atom response

On the single-atom level, the interaction of an intense light field beyond the perturbative regime has been described by a semi-classical three-step recollision model[22,23*], illustrated in Fig. 2.2. In the first step, the atomic potential gets bent by a linearly polarised laser field, permitting an electron to tunnel out into the continuum. The second step describes the motion of the freed electron: it first gets accelerated away from the parent ion, but then reverses its direction of travel as the field changes sign. Having a non-zero probability of returning into the vicinity of the ion, in the third step the electron may recombine. It thereby emits a photon with the energy $\Omega = I_p + E_k$, where I_p is the ionisation potential of the atom and E_k the kinetic energy of the electron upon return. The process repeats every half-cycle of the laser field, resulting in periodic bursts of light. In the frequency domain, this corresponds to a frequency comb (more detail in Sect. 2.3).

The movement of the electron in the linearly polarised field** $F = F_0 \cos(\omega t)$ can be described classically:

*A fully quantum-mechanical approach was developed soon after[24]. The author restricts the discussion to the semi-classical model as it is perfectly suitable to explain the main properties of the HHG process relevant to the discussed subjects.

**It was long believed that HHG from circularly polarised driving fields was impossible due to the lateral drift of the electron in the continuum, which would prevent it from recombining with the parent ion. However, recent studies[25,26,27] have shown that generation of circularly polarised high-order harmonics is in fact feasible. This thesis will only address linearly polarised fields since they were used in all of the presented experiments.

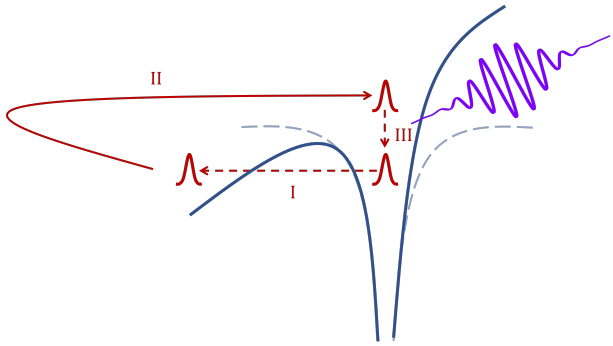

Figure 2.2: Three-step model. An electron is (I) liberated via tunnel ionisation when the external field lowers the atomic barrier, (II) accelerated by the same field, (III) recombined with the parent ion as the field sign reverses. Upon recombination, energy equal to the sum of electron kinetic energy and I_p is released in the form of a photon.

$$m_e \ddot{x}(t_i, t) = eF_0 \cos(\omega t), \tag{2.2}$$

where m_e stands for the electron mass, e its charge, F_0 is the field amplitude and ω its central frequency. Assuming that the electron is freed with a zero velocity and placing the centre of the coordinate system at the point of ionisation, one can integrate Eq. 2.2 twice to obtain the dependence of the spatial coordinate on time:

$$x(t_i) = 0, \;\; \dot{x}(t_i) = 0 \tag{2.3}$$

$$\dot{x}(t_i, t) = -\frac{eF_0}{m_e \omega}\left[\sin(\omega t) - \sin(\omega t_i)\right] \tag{2.4}$$

$$x(t_i, t) = \frac{eF_0}{m_e \omega^2}\left[\cos(\omega t) - \cos(\omega t_i) + (\omega t - \omega t_i)\sin \omega t_i\right], \tag{2.5}$$

where t_i is the ionisation time, referenced to the beginning of a cycle of the driving field. Figure 2.3 illustrates the trajectories that electrons may take for different values of t_i. If the atom is ionised while the instantaneous electric field amplitude is large ($t_i \leq \mathrm{T}/4 = \pi/(2\omega)$), the electron gets driven far away from the atom before the field changes sign. As a consequence, the recombination probability drops down to virtually zero. Of those trajectories that do end with recombination, one can distinguish between two branches leading to the same final energy spectrum: *(i)* $\pi/(2\omega) = \mathrm{T}/4 < t_i < \mathrm{T}/3 = 2\pi/(3\omega)$ - *long trajectories*, and *(ii)* $2\pi/(3\omega) = \mathrm{T}/3 \leq t_i \leq \mathrm{T}/2 = \pi/\omega$ - *short trajectories*. The kinetic energy of the electron upon recombination can be expressed as

$$E_k = 2U_p\big[\sin(\omega t_r) - \sin(\omega t_i)\big]^2, \tag{2.6}$$

where t_r is the time of recombination and

$$U_p = \frac{e^2 F_0^2}{4 m_e \omega^2} \sim \lambda^2 I \tag{2.7}$$

the ponderomotive potential, i.e. the cycle-averaged quiver energy a free electron acquires an AC field with the strength F_0. In the expression above, λ designates the wavelength, and I the intensity. The two trajectory branches merge for $t_i \approx \mathrm{T}/3$, corresponding to the recombination time $t_r \approx 0.95\mathrm{T}$, where the energy maximum is attained:

$$E_k = I_p + 3.17 U_p. \tag{2.8}$$

The expression above[28] is referred to as the HHG cut-off law. It expresses the fact that, in order to generate broadband XUV spectra, one needs to employ high laser intensities and long central wavelengths.

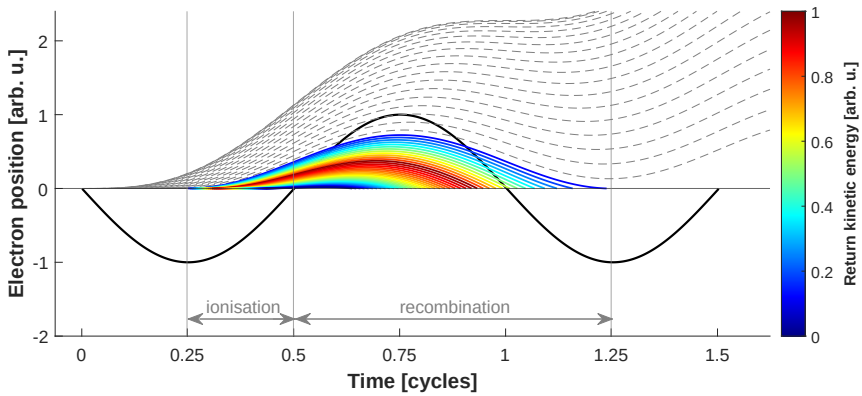

Figure 2.3: Classical electron trajectories in HHG. Black: driving electric field (arbitrary units). Colour: long and short recombining trajectories, resulting in photon emission. Gray: trajectories of electrons that do not return to the parent ion. The depicted process repeats every half-cycle of the laser field.

2.2 Macroscopic response

The macroscopic high-order harmonic field represents a superposition of radiation from many emitters, and thus depends on their mutual coherence. Therefore, this

aspect must complement the single-atom response in order to fully describe the HHG process.

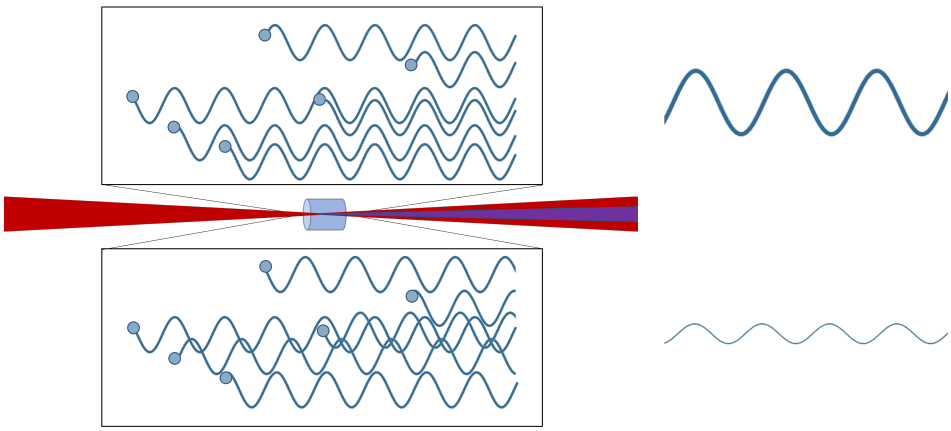

Figure 2.4: Phase-matching. Mutually coherent emission from many emitters results in a substantial increase of light intensity.

As illustrated in Fig. 2.4, a substantial HHG build-up demands a high level of phase synchronisation between individual emitter atoms, called phase-matching. It is convenient to describe this synchronisation using the k-vector approach. To ensure efficient harmonic generation, one needs to match the wavevector of the generat*ed* field to the sum of the wavevectors of the generat*ing* field. The common way of quantifying phase-matching is in terms of the harmonic-order-dependent wave-vector mismatch, $\Delta\mathbf{k}(q) = q\mathbf{k} - \mathbf{k}_q$, (in further text: Δk) where q denotes the harmonic order and $\mathbf{k}$ the wave-vector of the fundamental field. Restricting the considerations to the laser propagation direction, Δk can be decomposed into four contributions:

$$\Delta k = \Delta k_n + \Delta k_e + \Delta k_d + \Delta k_{\mathrm{G}}. \tag{2.9}$$

Δk_n (positive) and Δk_e (negative) are caused by the dispersion due to neutral atoms and plasma, respectively. Δk_d (negative before the laser focus, positive after) originates from the intensity dependence of the dipole phase, acquired in the continuum by the electron. Δk_G (negative) is the result of the so-called Gouy phase, a geometrical phase due to the focusing of the laser beam.

For a given generation medium and geometry (focal length used for laser beam focusing, along with the length of the generation medium), the two critical parameters are gas pressure and ionisation rate. Given that $\Delta k_{n/e}$ is proportional to the pressure and aiming to phase-match short trajectories in configurations where the medium is

centered close to the focus ($\Delta k_d \approx 0$ to a good approximation), one needs to attain the following balance[29]:

$$p\Big[\frac{\partial \Delta k_n}{\partial p} + \frac{\partial \Delta k_e}{\partial p}\Big] + \Delta k_{\mathrm{G}} = 0 \tag{2.10}$$

Equation 2.10 defines the phase-matching pressure and expresses the fact that there is an upper limit for the ionisation rate (typically a few percent[29]) set by $|\Delta k_n| = |\Delta k_e|$, above which phase-matching is not possible.

From a practical point of view, achieving a large harmonic yield relies on the daily adaptation of the experimental conditions that influence the sources of phase (mis)match. Due to its linear relationship with $\Delta k_{n/e}$, small changes in gas pressure will not have a dramatic effect on the phase-matching. In daily experimentation, the pressure is usually set to a value pre-determined for the chosen generation medium (as high as possible in order to increase the number of emitters, yet below the level for significant plasma build-up that could destroy the phase-matching, and which scales linearly with pressure for constant intensity[29]). The main adjustment is done by changing the intensity, which affects all four factors of Δk. Δk_n and Δk_e are affected through the change in the ionisation rate. Namely, as more and more atoms in the generation gas are ionised, the density of neutrals decreases whereas that of free charges increases, which causes a change in refractive index, and consequently the phase mismatch. Δk_d has a more complicated relationship with intensity[30] and exhibits a strong dependence on the electron trajectory. Since electrons following long trajectories spend more time in the continuum than their short-trajectory counterparts, they will acquire a larger dipole phase. While $\Delta k_{d,short}$ can be neglected compared to other Δk components, $\Delta k_{d,long}$ varies a lot with intensity. This stronger dependence on intensity also results in a greater divergence of long trajectories, as well as significant phase variations with harmonic order, making long trajectories less convenient for many applications. Unless the experiment poses special requirements, the intensity is chosen so that only the short trajectories are phase-matched.

The last parameter routinely adjusted in HHG is the position of the focus, which has a substantial effect on the harmonic beam divergence. Their relation originates from the variation of the frequency-dependent dipole phase $\Phi(\Omega)$ in the radial direction r[30]. This leads to strong chromatic aberrations, especially when the medium is located before the laser beam focus. In daily work only fine adjustments of the generation medium position are done (typically $\sim 1\%$ of the focal length applied).

2.3 Time and frequency aspects of high-order harmonic radiation

The HHG process described by the single-atom response in Sect. 2.1 repeats upon each half-cycle of the driving IR field. In case of a long laser pulse comprising many optical cycles, the ensuing XUV radiation is emitted in the form of a train of attosecond pulses (APT)* due to the interference of radiation generated by different half-cycles of the IR. This can be seen as a temporal analogon of multi-slit interference, sketched in Fig. 2.5, where the number of "slits" corresponds to the number of driving field half--cycles that contribute to harmonic emission and the resulting fringe pattern represents the HHG spectrum. It should be noted that, HHG being a strongly nonlinear process, only the most intense half-cycles of the IR pulse can be efficiently up-converted. This results in a temporal narrowing of the XUV APT envelope compared to that of the driver. The XUV frequency comb features only odd-order harmonics** of the IR field, which can be explained by the fact that centro-symmetric materials, such as inert gases often used for HHG, do not support even-order optical non-linearities[37]. It is worth mentioning that the bandwidth of the harmonics can be manipulated by varying the bandwidth of the driver. Assuming Fourier-transform limited (FTL) driving pulse duration, decreasing the input bandwidth is equivalent to pulse lengthening in time due to the time-bandwidth relation (Eq. 2.1). This has the effect of increasing the number of "slits" in the temporal interference picture shown in Fig. 2.5, and consequently leads to a decrease in harmonic bandwidth. This fact is exploited so as to meet the requirements of specific experiments. A typical experimental HHG spectrum is shown in Fig. 2.1.

(Nearly-)single-cycle driving pulses present a special case where the number of temporal slits is 1 or 2. The resulting HHG spectrum is (nearly) continuous and corresponds to one or two attosecond pulses.

Experimentally speaking, APTs are much easier to produce since commercially available ultrafast lasers typically deliver many-cycle IR pulses. In order to create single attosecond pulses (SAPs), two mutually non-exclusive approaches may be taken: **(i)** generating harmonics from somewhat longer driving pulses but suppressing emis-

*For the sake of consistency with general literature, the author will refer to trains of attosecond pulses as *attosecond pulse trains* (APT). It should, however, be noted that this term is misleading, as it is the individual pulses in the train that have attosecond duration, while the duration of the train as a whole is of the same order of magnitude as that of the driving pulse (fs).

**The symmetry of the HHG process can be broken by adding a secondary generation field, such as the second harmonic of the fundamental[31,32] or even a static field[33,34]. The other symmetry sustaining the presence of only odd harmonics in the HHG spectrum, inversion symmetry of the generation medium, is characteristic of atomic and molecular gases, liquids and amorphous solids, but broken in oriented molecules[35] and crystalline solids[36].

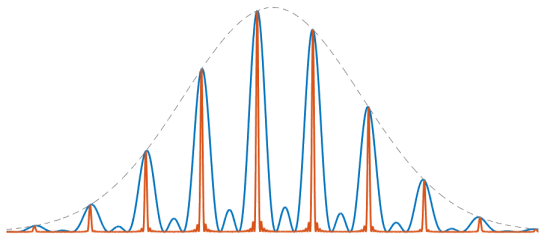

Figure 2.5: Multi-slit interference. Patterns resulting from three- (blue) and twenty-slit (red) interference, originating from a pulse with a Gaussian temporal distribution (gray dashed line).

sion outside a chosen half-cycle, known in literature as *gating*[38,39,40,41], or (**ii**) applying a spectral broadening scheme in combination with a compressor to obtain a nearly-single-cycle driving pulse. In general, both approaches rely on the control of the phase offset between the carrier and the envelope of the IR field[42]. Chapter 3.6 offers detail on some of the spectral broadening techniques for generating supercontinua supporting single-cycle pulses.

Attosecond pulses created via HHG (APTs as SAPs) carry intrinsic dispersion. As can be seen in Fig. 2.3, different frequencies are generated at different instances, leading to a variation of instantaneous frequency across the pulse, referred to as *attochirp*. Its origin is the dipole phase acquired by the electron in the continuum. Approximating the return kinetic energy of the electrons as a linear function of recombination time (valid in the plateau region of the harmonic spectrum), the intensity-dependent part of the dipole phase for short trajectories can be expressed as[43*]:

$$\Phi(\Omega) = \frac{\gamma}{I}(\Omega - \Omega_p)^2, \tag{2.11}$$

where Ω is the harmonic energy, γ is a constant equal to $1.03 \times 10^{-18}\,\mathrm{s^2Wcm^{-2}}$ for a central laser frequency $\omega = 1.55$ eV, I is the laser intensity, and $\Omega_p = I_p/\hbar$, where I_p is the ionisation potential of the generation medium. The dependence of Φ on Ω causes a group delay according to:

$$\mathrm{GD_{XUV}} = \frac{\partial\Phi}{\partial\Omega} = \frac{2\gamma}{I}(\Omega - \Omega_p) \tag{2.12}$$

The attochirp is the derivative of $\mathrm{GD_{XUV}}$ with respect to frequency - the group delay dispersion of the attosecond pulse:

*The expression for the dipole phase most commonly found in literature[44] is $\Phi(\Omega) = \alpha_q I$, $\Omega = q\hbar\omega$, which holds if $(\Omega - \Omega_p) \sim I$, i.e. in the harmonic plateau region.

$$\mathrm{GDD_{XUV}} = \frac{\partial^2 \Phi}{\partial \Omega^2} = \frac{2\gamma}{I} \tag{2.13}$$

The typical value of attochirp lies in the range of a few to few tens of as/eV. It can be partially compensated by metallic filters used to block the remaining laser radiation after generation (more details in Sect. 2.4).

Another source of deviation from the Fourier transform limit comes from the fact that the dipole phase depends on intensity, which itself is a function of time. This effect is thus more pronounced the shorter the pulse train, i.e. the steeper the gradient $\partial I/\partial t$. Given that individual harmonics result from the interference of many attosecond pulses from a train, each harmonic in the generated spectrum exhibits a form of dispersion called *femtochirp*. This effect is more pronounced for the highest-order harmonics from short trajectories. While the attochirp leads to a stretching of individual pulses in a train, the femtochirp instead affects the train envelope, resulting in an unequal spacing of the attosecond pulses[44].

2.4 High-order harmonic generation setup in Lund

The laser system providing pulses used for HHG in the Lund Attolab is presented in detail in Sect. 3.2.1. The pulses propagate several meters in air before entering vacuum, which entails a pre-compensation of their spectral phase (mostly second-order) using an acousto-optical programmable dispersive filter. Just before entering the first vacuum chamber ("generation chamber" in Fig. 2.6), the beam is sent through an aperture towards an $f = 50$ cm focusing mirror at a small angle. So focused, it passes through a 0.5 mm-thick window before reaching an intensity that could result in significant phase distortions due to non-linear effects in glass or air. Approximately at its focus, it enters a $6 - 10$ mm-long gas cell with an inner diameter of 1 mm, where a noble gas (neon, argon, krypton or xenon) is released at a 1 kHz repetition rate by a pulsed valve (*Attotech*). The exact position of the gas cell with respect to the focus is adjusted in three dimensions via automated translation stages. The ambient pressure in the generation chamber is kept at about 10^{-3} mbar.

The generated harmonic beam continues to travel collinearly with the remaining IR, reaching a second vacuum chamber (10^{-6} mbar), where the IR is blocked by a $100 - 200$ nm-thick metallic filter (typically aluminium, but also zirconium, indium or titanium for special purposes). The filter also has the role of compensating some of the attochirp, since the used materials have negative dispersion in the XUV spectral range. The filtered harmonic beam is sent on a gold-coated $f = 30$ cm toroidal mir-

ror at grazing incidence before leaving the chamber through a differential pumping stage.

The XUV enters the interaction chamber, where its focus meets a continuous jet of target gas dispensed through a nozzle. The XUV ionises the gas, generating photoelectrons to be collected by a detector (not depicted in Fig. 2.6). Various information about the studied gaseous species is inferred from the recorded electron kinetic energy distribution. To avoid any contamination, the pressure is kept at about 10^{-8} mbar.

As the absorption in the target gas has minimal effects on the HHG spectrum, its monitoring is done after the interaction. The first diffraction order from a flat-field grating is sent on a micro-channel plate (MCP) followed by a phosphor screen. The latter is imaged with a charge-coupled device (CCD camera), providing a live reading of the XUV spectrum, instrumental as a direct feedback for HHG optimisation.

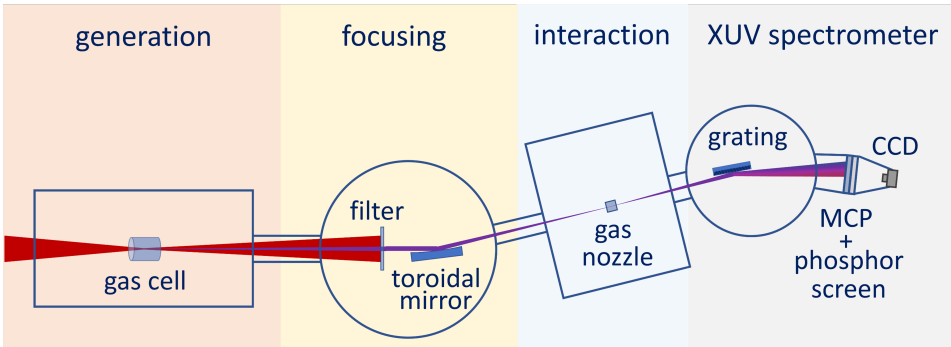

Figure 2.6: Schematic of the HHG setup in the Lund Attolab. The general HHG beamline layout, found in most HHG labs in the world, is indicated by the four coloured rectangles.

Chapter 3

Coherent pulses in the femtosecond regime

This thesis concerns the interaction of intense, ultrashort laser pulses with matter. The process of their generation, as well as their interaction with media, strongly depend on their spectrum and duration. This chapter discusses femtosecond infrared pulses, which can be converted into extreme ultraviolet pulses in the attosecond regime, as described in Chapter 2.

The term *ultrafast optics*, although in essence quite arbitrary, can be said to describe dealing with light pulses that need to be handled in special ways in order to preserve their spatio-temporal properties. This chapter aims to explain the ways in which ultrashort pulses may behave differently from their long counterparts, starting by their mathematical description to emphasise their important features. After that, it presents the main technologies that allow the production of femtosecond pulses in the many-optical-cycle regime and continues by discussing the ways their spectrum can be expanded so as to support even shorter pulse durations. The final part of the chapter discusses how to compress these pulses down to a few optical cycles, while at the same time performing their characterisation.

3.1 Mathematical description of ultrashort pulses

Ultrashort laser pulses can be conveniently described by their amplitude A and phase φ, in the time or frequency domain:

$$U(t) = A(t)e^{-i\varphi(t)} \tag{3.1}$$

$$\tilde{U}(\omega) = \tilde{A}(\omega)e^{i\tilde{\varphi}(\omega)} \tag{3.2}$$

The two descriptions are equivalent. One can easily switch from the temporal to the spectral form by applying a Fourier transform:

$$U(t) = \mathcal{F}^{-1}\{\tilde{U}(\omega)\} = \frac{1}{2\pi}\int \tilde{U}(\omega)e^{i\omega t}d\omega \tag{3.3}$$

$$\tilde{U}(\omega) = \mathcal{F}\{U(t)\} = \int U(t)e^{-i\omega t}dt \tag{3.4}$$

Given that time and frequency are Fourier-conjugate variables, the minimal duration of a light pulse is determined by its bandwidth. The wider its spectrum, the shorter the pulse can become if optimally compressed. Due to the direct correlation of the pulse shape in the time and frequency domains expressed in Eq. 3.3 and 3.4, the temporal properties of ultrashort pulses are inevitably very sensitive to dispersion. In other words, the shorter a pulse is, the harder it is to keep it short as it propagates through a medium. It is common to describe dispersion via the Taylor expansion of the spectral phase around a central frequency ω_0 (usually, the carrier frequency of the pulse of interest):

$$\tilde{\varphi}(\omega) = \tilde{\varphi}_0 + \tilde{\varphi}_0'\,(\omega-\omega_0) \;+\; \tilde{\varphi}_0''\,\frac{(\omega-\omega_0)^2}{2!} \;+\tilde{\varphi}_0'''\,\frac{(\omega-\omega_0)^3}{3!} + \ldots \tag{3.5}$$

The different dispersion orders $\tilde{\varphi}^{(n)}$ have a different influence on the pulse in the time domain:

$\tilde{\varphi}_0$ - *carrier-envelope phase* (CEP) - describes the phase offset between the electric field and the peak of the pulse envelope due to a difference in group and phase velocities of the pulse; practically relevant only for nearly-single-optical-cycle pulses (see Sect. 2.3)

$\tilde{\varphi}_0' = \left.\dfrac{\partial\tilde{\varphi}}{\partial\omega}\right|_{\omega_0}$ - *group delay* (GD) - results from a linear spectral phase and as such corresponds to a translation in time; has no effect on the temporal shape of the pulse

$\tilde{\varphi}_0'' = \left.\dfrac{\partial^2\tilde{\varphi}}{\partial\omega^2}\right|_{\omega_0}$ - *group delay dispersion* (GDD) - introduces a frequency-dependent time translation and thus alters the pulse in the time domain; results in a linear chirp

for Gaussian pulses, non-linear otherwise; positive (negative) values define the region of normal (anomalous) dispersion

$\tilde{\varphi}_0''' = \left.\frac{\partial^3 \tilde{\varphi}}{\partial \omega^3}\right|_{\omega_0}$ - *third-order dispersion* (TOD) - introduces a complicated relation in the time domain between pulse components of different frequencies.

The influence of different dispersion orders on the pulse in the time domain is illustrated in Fig. 3.1.

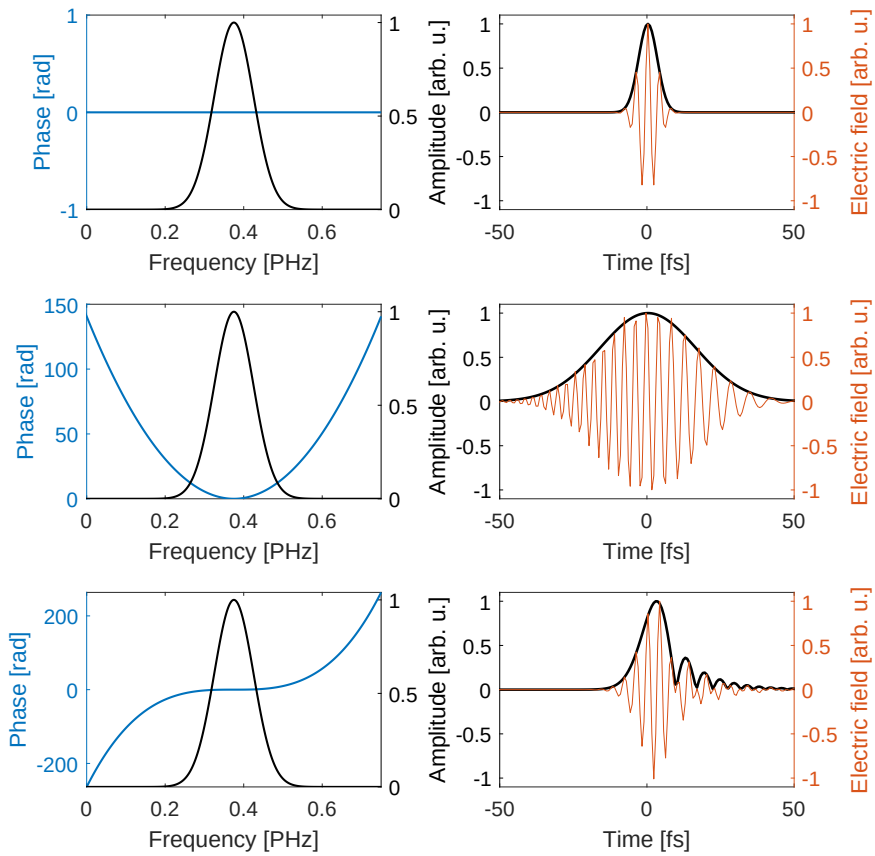

Figure 3.1: Impact of spectral phase on pulse shape and duration. Left column: spectrum (black) and spectral phase (blue); right column: pulse amplitude in time (black), electric field (red). From top to bottom row: Fourier transform limited pulse, pulse with GDD only, pulse with TOD only.

3.2 Ultrashort pulse lasers

State-of-the-art table-top sources of ultrashort pulses are femtosecond lasers with mode-locked oscillators. Their principle of operation is to have a great many modes oscillating in the cavity, resulting in a substantial coherent buildup over a short period of time where their phases are synchronised, as shown in Fig. 3.2. The pulse duration depends on the gain bandwidth and shape of the spectral density function. The equipment used in most of the experiments described in this thesis is a Titanium:Sapphire (Ti:Sa) amplification chain producing a nearly Gaussian output spectrum with a ≈ 100 nm FWHM bandwidth centred around $\lambda_0 = 800$ nm and a Fourier-transform-limited pulse duration of ≈ 21 fs.

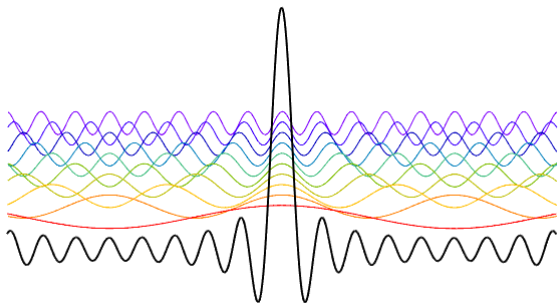

Figure 3.2: Principle of mode-locking. Superposition of all cavity modes leads to a short, intense burst of light where their phases are synchronised, and low-power output elsewhere.

To avoid gain medium damage while reaching powers on the level of 100 GW ($1\,\mathrm{GW} = 10^9\,\mathrm{W}$), it is necessary to use chirped pulse amplification[45]. The initial step is to stretch the pulse from the oscillator in time using a dispersive element such as glass or an arrangement of gratings. The pulses are said to be positively chirped (low frequencies preceding the high ones) and their peak power is reduced, making them safe to amplify. Upon leaving the gain medium, the pulses are re-compressed by imparting negative dispersion using a pair of gratings. A schematic of the process is shown in Fig. 3.3.

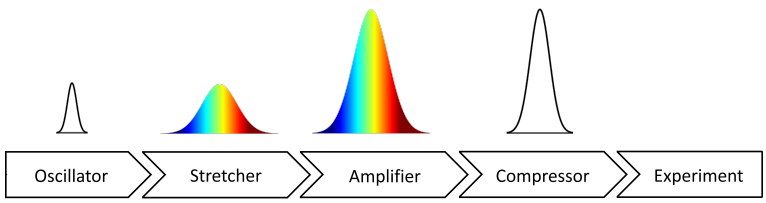

Figure 3.3: Principle of chirped pulse amplification. Oscillator pulses are stretched so they can be safely amplified and re-compressed with reflective optics after amplification.

3.2.1 Laser set-up in the Lund Attolab

Most of the experiments presented in this thesis (except Article III) were conducted using the same laser, shown in Fig. 3.4. The system is based on a *FemtoLasers Rainbow* oscillator delivering 7 fs pulses with a spectrum ranging from 600−1000 nm and energy of 2.5 nJ at a 76 MHz repetition rate. Stretching to about 400 ps is done using a single grating in combination with a retro-reflector and imaging (Öffner triplet configuration [46]). After stretching, the pulses are sent through an acousto-optical programmable dispersive filter (AOPDF), *Dazzler* from *Fastlite* (in further text: Dazzler), which enables spectral shaping and fine-tuning of the dispersion up to the fourth order. One can opt for reducing the spectral bandwidth, which allows for the tuning of the central wavelength across the original spectral profile of the oscillator pulses. Amplification then takes place in several stages, all based on Ti:Sa crystals. The first is a multi-pass pre-amplifier, followed by a regenerative amplifier, both of which are pumped at 1 kHz with a *Photonics DM 30-527* frequency-doubled neodymium-doped yttrium-lithium-fluoride (Nd:YLF) laser, increasing the pulse energy to about 0.4 mJ. Inside the regenerative amplifier, a second AOPDF, *Mazzler* from *Fastlite*, is applied to compensate for the gain narrowing. The next amplification stage is a three-pass amplifier pumped with the same Nd:YLF laser. The final amplification is done in a cryogenically cooled (−150° C) crystal pumped by a *Continuum Terra* laser, resulting in a pulse energy of ≈6 mJ. A pair of holographic gratings compresses the pulses to a Fourier transform limited duration of about 21 fs for an unreduced bandwidth, 750−850 nm. The diffraction efficiency of the gratings limits the final output energy to about 3.5 mJ.

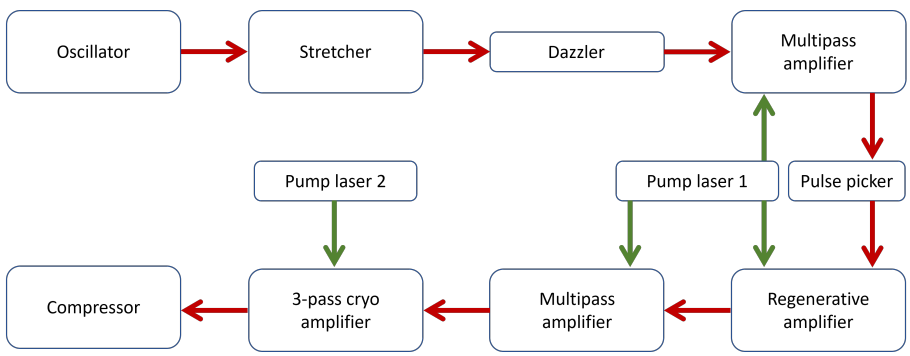

Figure 3.4: Schematic of the laser system in the Lund Attolab. Based on CPA, the chain consists of an oscillator, stretcher, several amplification stages and a grating compressor.

3.3 Medium response to intense ultrashort pulses

As pointed out in Sect. 3.1, the broader the spectrum of a pulse, the shorter the minimal duration it supports. A highly desirable feature of intense ultrashort pulses lies in the fact that it is possible to broaden their spectrum through non-linear interactions with media. The mechanism most widely employed for this spectral broadening is self-phase modulation, the temporal manifestation of the Kerr effect. To understand its principle, it is instructive to examine the response of a medium to a strong electric field. Electric polarisability of a material is a non-linear function of the applied electric field strength, which can be expressed as[37]:

$$P(t) = \epsilon_0 \big[\chi E(t) + \chi^{(2)} E^2(t) + \chi^{(3)} E^3(t) + ... \big], \tag{3.6}$$

where ϵ_0 is the vacuum permittivity, $\chi^{(n)}$ the n^{th}-order electric susceptibility, and $E(t) = E_0 \cos(\omega_0 t)$, with ω_0 as the field frequency. It can be shown[37] that even orders of polarisability vanish identically in centrosymmetric media (gases, liquids, amorphous solids, some crystals). Using that fact and the identity
$\cos^3(\omega t) = \frac{1}{4}\cos(3\omega t) + \frac{3}{4}\cos(\omega t)$ and restricting the above expansion to the third order, one can rewrite Eq. 3.6 explicitly:

$$P = \frac{1}{4}\epsilon_0 \chi^{(3)} E_0^3 \cos(3\omega_0 t) + \epsilon_0 \Big(\chi^{(1)} + \frac{3}{4}\chi^{(3)} E_0^2 \Big) E_0 \cos(\omega_0 t). \tag{3.7}$$

The two terms in Eq. 3.7 describe two different classes of processes that take place when an intense electric field interacts with a high-$\chi^{(3)}$ material. The first one refers to third harmonic generation (THG), a parametric process adequately described using perturbation theory (i.e. should not be regarded in view of the HHG process presented in Ch.2). The second term in Eq. 3.7 addresses the non-linear response of the medium at the frequency of the input field and will be the focus of this exposition. The effective susceptibility can then be written as:

$$\chi = \chi_{\mathrm{L}} + \chi_{\mathrm{NL}} = \chi^{(1)} + \frac{3}{4}\chi^{(3)} E_0^2 \tag{3.8}$$

and the corresponding effective refractive index as:

$$n = \sqrt{(1+\chi)} \approx 1 + \frac{1}{2}\Big(\chi^{(1)} + \frac{3}{4}\chi^{(3)} E_0^2 \Big). \tag{3.9}$$

Using $I = \frac{1}{2} n_0 \epsilon_0 c E_0^2$, where I is the intensity of the incident light, c the speed of light, and n_0 is the linear refractive index of the medium, one can obtain:

$$n(r,t) = n_0 + \frac{3}{4n_0^2 \epsilon_0 c} I(r,t) = n_0 + n_2 I(r,t). \tag{3.10}$$

From here it is evident that intense light fields induce an intensity-dependent change of the refractive index, known as the Kerr effect. In practise, only ultrashort laser pulses have enough intensity to induce a measurable third- or higher-order polarisability (Eq. 3.6). The rapid variations of their intensity distributions in space and time result in substantial spatial and spectral reshaping.

Self-phase modulation

Under the condition formulated in Eq. 3.10, a laser pulse propagating in a Kerr medium will experience a time-dependent instantaneous frequency according to:

$$\omega(t) = \frac{\partial \varphi(t)}{\partial t} = \omega_0 - \frac{2\pi L}{\lambda_0} n_2 \frac{\partial I}{\partial t}, \tag{3.11}$$

where φ is the temporal phase, ω_0 the input field carrier frequency, λ_0 the corresponding wavelength, and L the medium length. The phase shift induced by the time-dependence of the refractive index thus up-chirps the pulse as it gets spectrally broader. This is illustrated in Fig. 3.5.

Self-focusing

In the spatial domain, a linear dependence of the refractive index on intensity has the effect of a focusing lens, illustrated schematically in Fig. 3.6. The attribute commonly used to describe the dynamics of this effect is the characteristic self-focusing length L_{SF}, over which the accumulated non-linear phase changes by a unit value[47]:

$$L_{\mathrm{SF}} = \frac{1}{n_2 k_0 I_0}, \tag{3.12}$$

where $k_0 = 2\pi/\lambda_0$, and I_0 is the peak intensity.

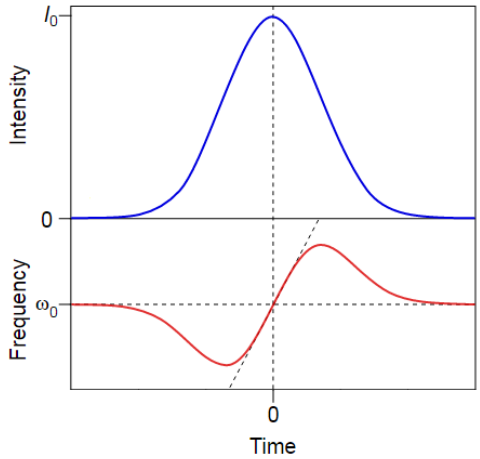

Figure 3.5: Self-phase modulation. The intensity-dependent refractive index causes a phase variation in time, leading to a shift of the instantaneous frequency across the pulse.

The accumulated non-linear phase is described by the *B*-integral:

$$B = k_0 \int_0^z n_2 I(z)\ \mathrm{dz} \tag{3.13}$$

For pulses with power in excess of the critical value P_{cr}*, self-focusing overcomes diffraction effects, leading to a collapse of the beam towards its centre. The critical power takes the following form [48]:

$$P_{\mathrm{cr}} = \frac{\alpha \lambda_0^2}{4\pi n_0 n_2}, \tag{3.14}$$

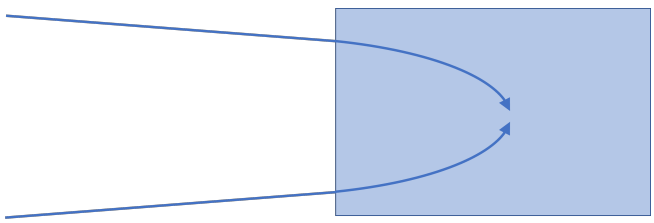

Figure 3.6: Schematic illustration of self-focusing. The light-induced transverse refractive index gradient has the same effect as a focusing lens. If diffraction effects cannot prevail, self-focusing leads to beam collapse towards the centre.

*It has been shown [48] that the solutions of the wave equation in self-focusing conditions possess a radial scale invariance provided that the beam has radial symmetry. Hence a critical power, rather than a critical intensity.

where α is a constant specific to the beam profile. The value of P_{cr} may range from $\sim$MW for solids to $\sim$GW for gaseous media. A positive feedback loop is inherent to self-focusing, so the process can only be arrested once the propagation medium gets damaged or de-focusing effects take over. More on the latter in Sect. 3.4.2.

3.4 SPM-based supercontinuum generation

Laboratories with many-cycle femtosecond lasers, like the one in the Lund Attolab, may obtain few-cycle pulses through postcompression. The principle is to exploit SPM to broaden the spectrum, and then apply negative dispersion using, most commonly, chirped mirrors[49]. As evident from Eqs. 3.10 and 3.11, for a given laser wavelength, the extent of spectral broadening depends on the choice of the propagation medium (through n_2), the propagation length and peak pulse intensity, as well as the pulse duration. Even though solid materials posses substantially higher n_2 than gases*, they are not the best choice for high-energy pulses due to their low self-focusing threshold and ensuing damage. Typically, solid broadening media are used for pulses in the microjoule range, while millijoule pulses are broadened in air or inert gases, safe and easy to use. In the following, the author will present the two general classes of practical solutions for SPM-based supercontinuum generation in gases.

3.4.1 Gas-filled hollow waveguides

Many schemes have been proposed to contain the generation gas for maximal output bandwidth and power. The first high-throughput device demonstrated in 1997 to produce below-5-fs pulses at $\lambda_c = 800$nm was a hollow-core fibre (HCF) made of fused silica and filled with Ar or Kr[52]. It has since been discovered that the throughput can be vastly augmented while producing a three-octave bandwidth using structured fibres[53,54]. The invention of hollow planar waveguides[55,56] allowed an increase of the input energy by providing a larger-area propagation mode compared to fibres. Multi--pass cells, originally designed with bulk silica as the broadening medium[57], have also been adapted to use with noble gases[58,59], allowing a continuous accumulation of the non-linear phase.

For mJ-energy pulses and kHz repetition rates (typical for Ti:Sa-based lasers operating around $\lambda_c = 800$ nm) the most common post-compression waveguide still remains

*For example, $n_2 \approx 4 \cdot 10^{-23}\mathrm{m}^2/\mathrm{W}$ for air[50], $n_2 \approx 3.5 \cdot 10^{-20}\mathrm{m}^2/\mathrm{W}$ for fused silica[51] at $\lambda = 800$ nm.

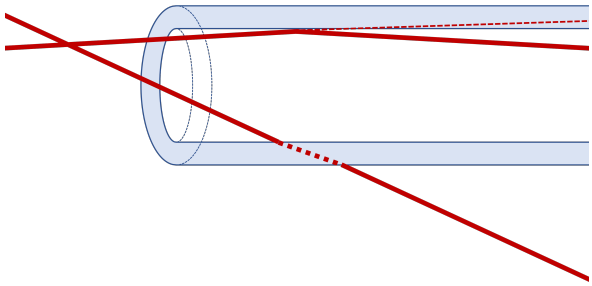

Figure 3.7: Hollow-core fibre operation principle. Light is guided through the gas-filled core via grazing incidence reflections with minor losses. Rays entering the fibre at larger angles suffer high reflection losses.

the hollow-core fibre. Propagation of light through an HCF mainly takes place via grazing-incidence reflections off the inner walls of the higher-refractive-index cladding ($n_{\text{gas}} \approx 1$ for air[60] and noble gases[61,62], while $n_{\text{FS}} \approx 1.45$[63] at $\lambda = 800\,\text{nm}$), as illustrated in Fig. 3.7. This entails a loose-focusing scheme. Owing to the geometry of the HCF, the fundamental hybrid mode, EH_{11}, has substantially lower losses than higher-order modes[64,65], providing a clean output mode. Its intensity profile is

$$I_{\text{EH}_{11}}(r) = I_0 J_0^2 \, \frac{2.405\, r}{a}, \tag{3.15}$$

where J_0 is the 0^{th}-order Bessel function of the first kind, and a the inner radius of the fibre. The beam profile of a Ti:Sa laser is Gaussian to a good approximation:

$$I_{\text{Gauss}}(r) = I_0 \, \exp\Big(-\frac{2r^2}{w_0^2}\Big), \tag{3.16}$$

so the coupling efficiency can be calculated as

$$\eta = \int_0^\infty U_{\text{EH}_{11}}(r)\, U_{\text{Gauss}}(r)\, dr, \tag{3.17}$$

where $U_{\text{EH}_{11}}$ and U_{Gauss} are the normalised modes' amplitudes. The highest coupling efficiency, $\eta_{\text{max}} = 98\%$ can be found for $w_0 \approx 0.65\, a$. For a given Gaussian laser beam radius w, and wavelength λ, this sets a clear focusing criterion[66]:

$$w_0 = \frac{\lambda f}{\pi w} \implies f = \frac{0.65\, a\, \pi w}{\lambda} \tag{3.18}$$

In order to assess the transmission of an HCF, one needs to take into account the propagation losses. They can be expressed using the attenuation constant[65]:

$$\alpha = \left(\frac{2.405}{2\pi}\right)^2 \frac{\lambda^2}{a^3} \frac{\nu^2 + 1}{\sqrt{\nu^2 - 1}}, \tag{3.19}$$

where ν is the ratio between the refractive indices of the cladding and the gas. The transmission of an HCF with the length L is:

$$T = \eta\, e^{-\alpha L}. \tag{3.20}$$

This analysis reveals most of the practical considerations HCFs entail. In order to maximise the spectral broadening, one needs to use long fibres (see Eq. 3.11). However, this comes at the cost of energy throughput according to Eq. 3.20. Using a larger core mitigates the losses, which scale as the inverse cube of the radius (Eq. 3.19), but at the same time, this lowers the light intensity, thus diminishing the spectral broadening (Eq. 3.11).

It is important to add that partial ionisation of gas inside the HCF has a significant influence on the pulse dynamics. Substantial ionisation causes coupling to higher-order fibre modes, leading to additional losses.

HCFs were used for spectral broadening in Articles I-III.

3.4.2 Spectral broadening upon self-guided propagation

As pointed out in Sect. 3.3, a laser beam with a power in excess of P_{cr} (Eq. 3.14) collapses towards its centre. This causes a rapid increase in intensity, eventually passing the threshold for multiphoton ionisation (MPI). The leading edge of the pulse leaves behind a plasma wake for the trailing edge to diffract on. The front of the pulse eventually loses energy to MPI and plasma generation is quenched, restoring the refractive index of the neutral gas and allowing self-focusing to happen again. For a special set of conditions, self-focusing and plasma diffraction can take multiple turns in governing the beam propagation, which is then forced to take place in re-focusing cycles until too much power is lost to MPI, diffraction, and dispersion. This type of propagation, sketched in Fig 3.8, where the beam size stays small over distances considerably longer than the Rayleigh length, is referred to as *filamentation*. This feature sustains the high intensity needed for SPM, leading to substantial spectral broadening. Spectra spanning up to three octaves have been generated by means of filamentation[67].

The cross-section of a filament consists of two distinct regions: a brilliant, white central part called the *filament core*, and a lower-intensity reservoir capable of exchanging energy with the core, as demonstrated theoretically[68] and experimentally[69]. In the far field, one can visually discern the core and a surrounding array of colourful rings, referred to as *conical emission* due to their high divergence. The order of the colours is reversed compared to the one present in ordinary light diffraction: lower wavelengths have a more pronounced divergence than higher ones.

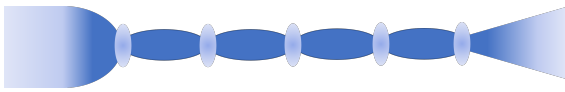

Figure 3.8: Principle of filamentation. Self-guided propagation is sustained by a dynamic balance between self-focusing and plasma de-focusing, resulting in the appearance of re-focusing cycles. This sketch should be considered a rough approximation as it does not take into account the polychromaticity of the pulse undergoing filamentation and the effects resulting from it.

In cases where $P_{\text{in}} >> P_{\text{crit}}$, the filament may split into several separate components. In this scenario, laser beam profile imperfections provoke local self-focusing, creating nucleation cites for individual filaments[70].

The fact that the filamentation process is essentially sustained by a dynamical competition between self-focusing and plasma defocusing inherently limits the intensity in the filament core[71]. The so-called *clamping intensity* can be assessed knowing that the multiphoton absorption rate scales as I^{K}, where I is intensity and K the number of absorbed photons. It can be shown[47] that for a Gaussian pulse

$$I \sim \left(\frac{\sigma_{\text{K}}\rho_n\tau}{2n_2\rho_c}\right)^{\text{K}-1}, \tag{3.21}$$

where σ_{K} is the K-photon absorption cross-section, ρ_n the density of neutral atoms, τ the laser pulse duration, and ρ_c the critical plasma density above which it becomes opaque. For femtosecond pulses at $\lambda = 800$ nm this corresponds to $I \sim 10^{13}$ W/cm^2.

Due to the high intensities involved, as well as the large bandwidths present from the very beginning and expanding thereafter, filament dynamics are highly non-linear and rather intricate. Effects with the greatest impact on the spectro-temporal reshaping are explored in the following.

Self-steepening

As pointed out in Sect. 3.3, under the condition of normal dispersion, the peak of an intense laser pulse will experience a higher refractive index than the edges. This has long been known[72] to cause a slowing down of the peak with respect to the group velocity and consequently a steepening of the trailing edge of the pulse. This steep edge promotes generation of higher frequencies in the spectrum.

Plasma blueshifting

The plasma generated through MPI at the leading edge of the laser pulse alters the refractive index of the medium according to[73]:

$$n_p(r,t) = n_0 - \frac{\rho_e(r,t)}{2\rho_c}, \quad \rho_c = \frac{\epsilon_0 m_e \omega_0^2}{e^2}, \tag{3.22}$$

where ρ_e is the density of free electrons, ρ_c the critical value of plasma density at which it becomes opaque, ϵ_0 vacuum permittivity, m_e electron mass, e its charge and ω_0 the angular frequency of the light. The degree of gas ionisation changes rapidly along the leading edge of the pulse, causing a decrease in the refractive index of the medium. The electron recombination time is much longer than the laser pulse, making the increase in electron density monotonous over the pulse duration. According to Eq. 3.11, the SPM-related frequency shift can be expressed as

$$\Delta\omega = -2\pi L \, \frac{\partial n_p}{\partial t} = \frac{\pi L}{\rho_c} \frac{\partial \rho_e}{\partial t}, \tag{3.23}$$

demonstrating what is known as plasma blue-shifting.

Pulse splitting

An interesting phenomenon often observed in filamentation is the splitting of the driving pulse in two components separated in time, the earlier one featuring a lower--frequency spectral content than the later one. This behaviour can be interpreted within the framework of dynamic spatial replenishment[74,75]. This approach abandons the static picture of self-guided propagation, where energy from the input laser pulse propagates in the form of "light bullets", corresponding to the sketch in Fig. 3.8. Instead, it describes filament dynamics as governed by photon absorption from the leading edge of the pulse and subsequent filament replenishment from the trailing

edge. Namely, the front edge, red-shifted due to the sign of its intensity gradient (Eq. 3.11), generates plasma. The free charges in turn cause a diffraction of the blue--shifted trailing edge, delaying its self-focusing (that is, longitudinally shifting its onset). As the pulse centre gets attenuated by MPI, two distinct peaks start to be discernible in the temporal profile of the pulse. The effect is enhanced in media with pronounced GDD. The components of the split pulse may or may not undergo subsequent splitting, depending on the exact propagation conditions.

3.5 Pulse characterisation and compression down to the few--cycle regime

The spectral broadening techniques described in the previous section generally do not yield pulses with a flat spectral phase. Despite their shortened Fourier-transform limit, their duration after broadening will in fact often be approximately equal to the duration of the initial laser pulse (or even longer due to dispersion). The spectral phase of pulses that underwent SPM is largely of the second order, with additional components that cannot be described in terms of orders in the Taylor expansion given in Eq. 3.5. To achieve a short pulse duration, this phase needs to be compensated using suitable optical components, such as chirped mirrors[49] or transparent materials with an adequate dispersion profile. The one thing crucial for obtaining the shortest possible duration (also known as optimal *compression*) of a given pulse is to be able to properly characterise it and identify the corrections that need to be made. This section presents state-of-the-art methods for pulse characterisation, focusing on dispersion scan, which was used in Articles I-III, and VII.

3.5.1 Spectro-temporal pulse characterisation

Due to a lack of detectors fast enough to directly measure the duration of femtosecond pulses, ultrashort pulse characterisation instead relies on inducing a non-linear interaction between a material and the measured ("fundamental") pulse. The phase--sensitivity of exploited non-linearities provides a means for inferring the spectral phase of the fundamental from the optical response of the medium.

Plenty of techniques have been proposed for spectro-temporal ultrashort pulse characterisation[19]. Frequency-Resolved Optical Gating (FROG)[76,77,78] consists in performing spectrally resolved autocorrelation, generating a spectrogram of the form $S(\omega, t)$ and retrieving the electric field (excluding the carrier-envelope offset) using a mathematical procedure[79]. A different approach is used in Spectral Phase Interferometry for Direct Electric field Reconstruction (SPIDER)[80], where the measured pulse interferes

with a spectrally sheared replica of itself. The pulse is retrieved from the interference pattern of the two time-delayed sheared pulses, without the need of using iterative algorithms. In another technique, called Mutiphoton Intrapulse Interference Phase Scan (MIIPS)[81], a pulse is characterised by being subject to a set of different spectral phase curves and determining which one provides the best compression. The phase is applied using a pulse shaper (for example, Dazzler, see Sect. 3.2.1) or simply the grating compressor from a CPA laser. The spectral phase of the pulse is found by generating its second harmonic (in the following, second harmonic generation will be abbreviated as SHG) in a crystal and finding dispersion parameters that lead to local enhancements of the SHG signal, indicating that the spectral phase is locally flattened by the added dispersion (more detail below). A prominent technique named *dispersion scan* (d-scan), based on the MIIPS principle and jointly developed by Lund and Porto Universities, is given the focus in this section. This technique proposes simultaneous compression and characterisation of femtosecond pulses[82,83] and will be presented in detail in the following.

Principle

The concept of d-scan* is to record the second harmonic of the measured pulse as a function of the dispersion in the fundamental. A retrieval algorithm is used to reconstruct the pulse form from the recorded $\tilde{I}_{\mathrm{SHG}}(\omega, z)$ spectrogram (z is the thickness of the material used to introduce the dispersion).

Propagating a pulse through a dispersive medium can be described by applying a frequency-dependent phase term to Eq. 3.4:

$$\tilde{U}(\omega, z) = \tilde{A}(\omega) e^{i\tilde{\varphi}(\omega)} e^{ik_0(\omega) n(\omega) z}, \tag{3.24}$$

where k_0 is the vacuum wavenumber, n the refractive index of the medium, and z the distance travelled through it. The field of its second harmonic as a function of z can be modelled in the time domain as the square of the fundamental:

$$U_{\mathrm{SHG}}(t, z) = U(t, z)^2 = \Big(\mathcal{F}^{-1}\big[\tilde{U}(\omega, z)\big]\Big)^2 = \frac{1}{2\pi}\Big(\int \tilde{U}(\omega, z) e^{i\omega t} d\omega\Big)^2 \tag{3.25}$$

*This chapter presents the originally conceived d-scan based on SHG as the non-linear interaction of choice. Variants based on THG[84,85], cross-polarised wave generation[86,87], and self-diffraction[88] have also been proposed.

The experimentally measured quantity, however, is the spectral intensity of the second harmonic:

$$\tilde{I}_{\mathrm{SHG}}(\omega, z) = \left|\mathcal{F}\left[U_{\mathrm{SHG}}(t, z)\right]\right|^2 = \frac{1}{(2\pi)^2}\left|\int_{-\infty}^{\infty}\left(\int_{-\infty}^{\infty}\tilde{U}(\Omega, z)\, e^{i\Omega t} d\Omega\right)^2 e^{-i\omega t} dt\right|^2 \tag{3.26}$$

It should be noted that the above expression is based on the assumption of a frequency--independent non-linear response of the SHG medium. This is not realistic for ultrashort pulses since any SHG crystal will have a finite phase-matching bandwidth. Another assumption is a perfect spectral response of the spectrometer used to measure the signal. Expression 3.26 therefore needs to be corrected by applying a spectral filter, obtained through d-scan calibration:

$$\tilde{I}_{\mathrm{SHG,\,corr}}(\omega, z) = \tilde{I}_{\mathrm{SHG}}(\omega, z)\, \tilde{C}(\omega) \tag{3.27}$$

An example of a d-scan spectrogram, as well as the corresponding retrieval, can be seen in Fig. 3.9.

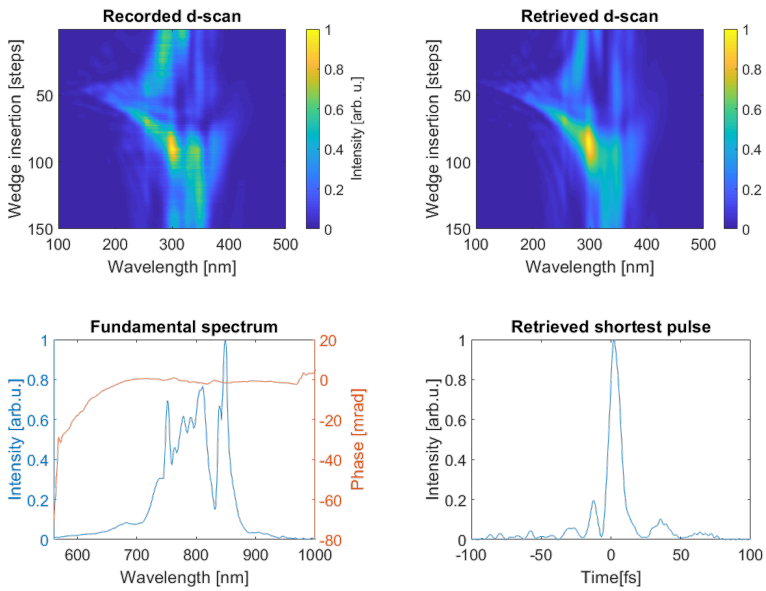

Figure 3.9: Recorded d-scan and pulse retrieval. Pulse with an initial duration of about 20 fs, spectrally broadened by filamentation and compressed by CMs, measured to be 10.2 fs long.

Retrieval

The pulse retrieval consists of finding the spectral phase which, when applied to the measured fundamental spectrum, best recreates the measured SHG traces. A guess--phase curve is applied to the fundamental, $\tilde{I}_{\mathrm{SHG}}(\omega, z)$ is simulated according to Eq. 3.26 and the RMS error between the measured and simulated trace is calculated:

$$G^2 = \frac{1}{N_m N_k} \sum_{m,k} (I_{\mathrm{meas}}(\omega_m, z_k) - \mu_m I_{\mathrm{retr}}(\omega_m, z_k))^2, \tag{3.28}$$

where I_{meas} and I_{retr} are the measured and simulated spectrogram, and

$$\mu_m = \sum_k \left[I_{\mathrm{meas}}(\omega_m, z_k) I_{\mathrm{retr}}(\omega_m, z_k) \right] / \sum_k I_{\mathrm{retr}}(\omega_m, z_k)^2 \tag{3.29}$$

is a minimization factor that is updated upon every iteration of the algorithm. Older d-scan implementations[82,83] relied on the Nelder-Mead[89], or downhill simplex, non--linear least squares algorithms for the minimisation of G. This type of retrieval is reliable and robust to noise, yet somewhat slow. An alternative proposed in Article I is an iterative generalised-projections retrieval algorithm. The principle is to impose a set of mathematical constraints on the retrieved pulse so as to reduce G in each iteration. This approach significantly shortens the retrieval convergence time, and is even applicable to cases where the fundamental spectrum is uncalibrated or missing. For a good overview of the different retrieval solutions, as well as the d-scan technique in general, the reader is referred to a recent article by Sytcevich et al[90].

Practical implementations

I Sweeping d-scan

The original implementation of the d-scan[82,83], sketched in Fig. 3.10, was suited to high repetition rate ($\geq$ kHz) pulse sources. The recorded signal is an average over many shots, smearing out any shot-to-shot instabilities and allowing the possibility to arbitrarily increase the integration time for better statistics.

After adequate attenuation, the measured pulses pass through a chirped mirror[49] (CM) compressor. The total number of reflections on the CMs is adapted so as to impart the negative dispersion needed to coarsely compensate the GDD of the pulse. The pulse also passes through a pair of small-angle (5–10°) glass wedges, one of which

is mounted on a motorised translation stage for very precise control of the inserted glass thickness, i.e. dispersion. Thereafter the pulses are sent on a focusing mirror at a small angle. An SHG type I crystal is placed in the focus of the beam and the generated second harmonic is collected by a spectrometer. The remaining fundamental is strongly attenuated using a polariser.

The pulse characterisation measurement consists in scanning the wedge insertion around the empirically determined point of maximal pulse compression. A piece of software is used to control the position of the translation stage holding the movable wedge, while recording the second harmonic signal with a spectrometer. The result is an $\tilde{I}_{\mathrm{SHG}}(\omega, z)$ spectrogram that traces the pulse's transition from long (uncompressed due to positive GDD; only SHG present), to short (optimally compressed with the given compressor dispersion; phase-matching enables sum-frequency generation), and long again (uncompressed due to negative GDD; sum-frequency generation suppressed once more). For an unambiguous pulse retrieval it is important that the entire trace be recorded. The amount of second- and third-order dispersion in the set-up should be adapted to get the "cleanest" possible pulse (with as few complicated phase features as possible) since this facilitates the retrieval. This is achieved by adjusting the number of bounces on the CMs (bringing the pulse closer to its FTL duration at the d-scan), changing the material of the wedges (accommodating for pulses of different FTL durations by adapting the dispersion tuning range) or adding pieces of material into the beam path. The wedge insertion step size and acquisition time at each step are adjusted in order to obtain smooth traces and increase the signal-to-noise ratio. The spectrogram is usually complemented by a measurement of the fundamental spectrum, which is often necessary for pulse retrieval (more detail below).

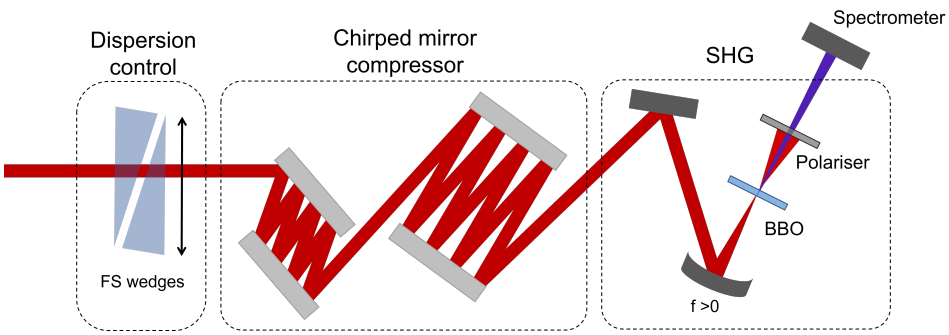

Figure 3.10: SHG d-scan scheme. One static and one movable glass wedge provide fine dispersion control. Coarse compression is done using chirped mirrors in a double-angle configuration, found to significantly reduce spectral phase oscillations [91]. The beam is sent on a focusing mirror at a small angle (greatly increased in the figure for ease of illustration) and SHG takes place in a crystal in the focus. The remaining fundamental is removed using a polariser. A spectrometer records the SHG signal as the insertion of a wedge is scanned.

Sample d-scan traces as a function of the dominant dispersion order of the pulse are shown in Fig. 3.11, illustrating how intuitive their interpretation is. This feature makes d-scan a desirable in situ diagnostic tool for pulse optimisation. The sweeping d-scan was used in Articles I-III, and VII.

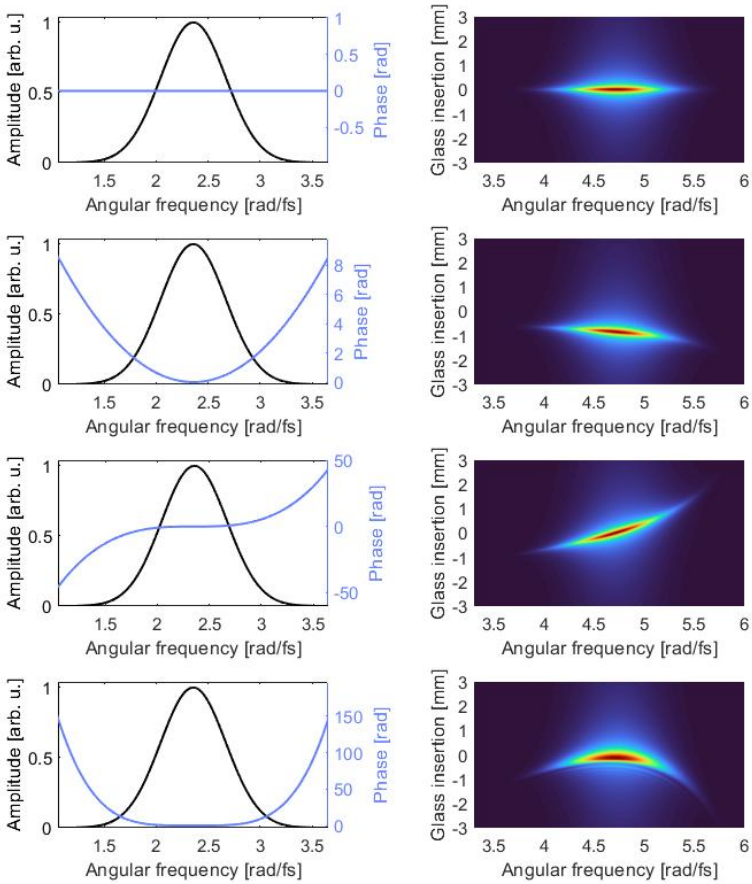

Figure 3.11: D-scan traces of pulses with different dispersion orders. Left: spectrum and spectral phase of the pulse; right: corresponding simulated d-scan traces. From top to bottom: Fourier transform limited pulse, pulse with second, third, and fourth order dispersion.

II Single-shot d-scan

High-power (TW) ultrashort-pulse lasers operate at low repetition rates ($\leq$ 100 Hz). For them, the sweeping version of the d-scan is not a good choice because integration

over many laser shots averages out any shot-to-shot fluctuations, resulting in a wrong trace. The solution is to apply the d-scan principle to one single laser shot at a time.

To have a single pulse undergo a continuous range of dispersion values, one can have different spatial parts of the pulse pass through different amounts of glass. This is simple enough to do by selecting the centre of the beam with an iris, expanding it using a telescope to ensure a large degree of spatial homogeneity, and sending the beam through a prism.

In the first practical demonstration of the single-shot d-scan [91], the beam passes through a horizontal slit and then through a prism. The hind face of the prism is imaged onto a BBO crystal, where SHG takes place. Cleaned from the fundamental by a polariser, the second harmonic beam is re-imaged onto the entrance slit of an imaging spectrometer. An alternative design, detailed in Article II, has been proposed by our group at Lund University. The novelty consists in focusing the beam into the BBO in an *off-axis* geometry, thereby introducing strong astigmatism, which permits to use the first focal plane for SHG, and the second one for imaging. This scheme reduces the number of optical components, making the set-up simpler and more compact.

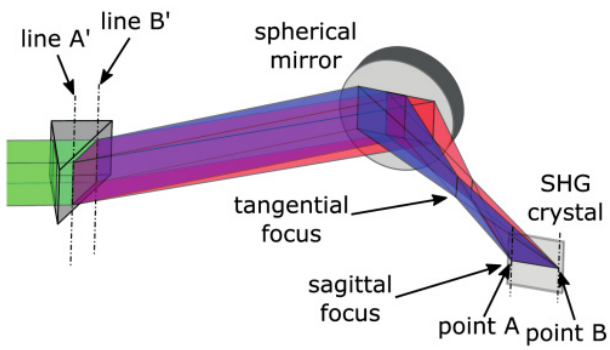

Figure 3.12: A new design for the single-shot d-scan. The beam is focused in an off-axis geometry, causing strong astigmatism. Imaging is done in one focal plane, and SHG in the other. Reproduced with permission from Article II.

In Article II, we test the performance of the proposed design by comparing it with the well-established sweeping d-scan. We do so by characterising pulses from a Ti:Sa-based laser, spectrally broadened in an HCF (see Sect. 3.4) so as to span from 450 to 1000 nm. As shown in Fig. 3.13, spectrograms of the same pulses were recorded by the standard d-scan with moving wedges and by the newly presented version of d-scan in both multi-shot and single-shot configurations. The recorded traces (as well as the resulting time-domain pulse retrievals) show an excellent degree of mutual agreement, validating our novel d-scan solution.

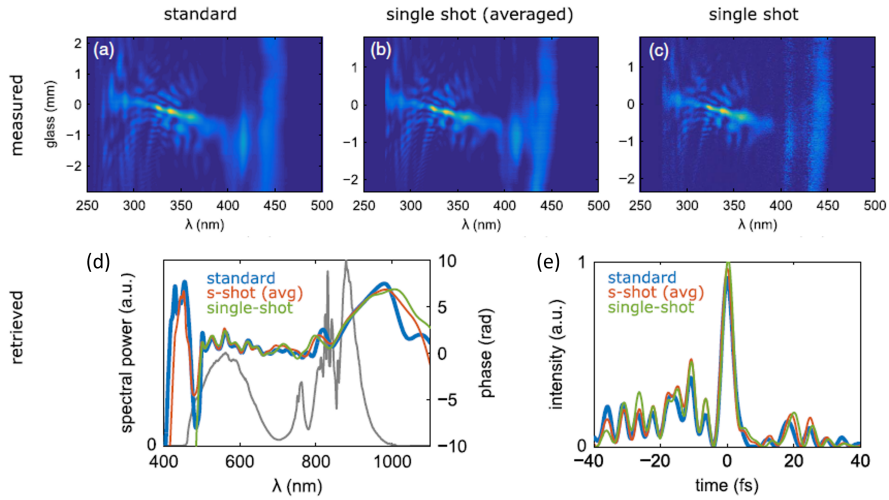

Figure 3.13: Comparison between single-shot and sweeping d-scan performance. D-scan spectrograms produced using (a) standard sweeping d-scan (fused silica wedges), (b) single-shot d-scan while integrating over about 15 pulses, (c) single-shot d-scan applied to one individual pulse. The retrieved spectral phase (d) and temporal profile of the pulses (e) are in excellent agreement. Grey line in (d): spectrum of the studied HCF-broadened pulse. Adapted from Article II.

CEP-sensitive d-scan

In the presented d-scan implementations, the fact that SHG yields photons with a polarisation perpendicular to that of the fundamental beam is exploited to strongly attenuate the residual fundamental signal using a polariser. This is particularly important in case of octave-spanning spectra, where the fundamental in part spectrally overlaps the second harmonic. Although any phase contamination is prevented by virtue of their perpendicular polarisations, the spectral density measurement can be affected if some of the fundamental signal remains unfiltered.

For some applications, however, this inconvenience can be turned into a benefit by forcing an interference between the fundamental and second harmonic beams by combining them with a polariser, thereby generating a CEP-dependent interference signal in the spectral overlap region. As we show in Article III for pulses broadened in a hollow-core fibre to feature octave-spanning spectra, the sensitivity to CEP can be exploited for a complete reconstruction of the electric field waveform. This is of particular importance for experiments using nearly-single-cycle pulses because in this regime the CEP critically affects the pulse properties, as illustrated in Fig 3.14.

The principle of the CEP-dependent d-scan can be understood by examining the second harmonic of a fundamental pulse U_{F}, writing the CEP separately for clarity:

$$U_{\mathrm{F}}(t) = A_{\mathrm{F}}(t)\, e^{-i\varphi(t)}\, e^{i\varphi_0} = E_{\mathrm{F}}(t)\, e^{i\varphi_0} \tag{3.30}$$

$$U_{\mathrm{SHG}}(t) = U_{\mathrm{F}}(t)^2 = E_{\mathrm{F}}(t)^2\, e^{2i\varphi_0} \tag{3.31}$$

Delaying the second harmonic with respect to the fundamental by Δt and going into the spectral domain by Fourier transforming according to Eq. 3.3, one obtains:

$$\tilde{U}_{\mathrm{SHG}}(\omega) = \mathcal{F}[E_{\mathrm{F}}(t)^2]\, e^{2i\varphi_0 - i\omega\Delta t} \tag{3.32}$$

The pattern of interference between the fundamental and harmonic pulses will follow the CEP- and delay-dependence:

$$\tilde{I} = |\tilde{E}_{\mathrm{F}}|^2 + |\tilde{E}_{\mathrm{SHG}}|^2 + 2|\tilde{E}_{\mathrm{F}}|\,|\tilde{E}_{\mathrm{SHG}}|\,\cos(\varphi_0 + \omega\Delta t) \tag{3.33}$$

The standard d-scan pulse retrieval algorithm, described in Sect. 3.5.1, models only the intensity, not the phase, of the SHG signal. The complete pulse-form can be determined by first performing this simplified retrieval on the entire spectrogram, and then applying a more sophisticated one, based on Eq. 3.32, only in the overlap region. The phase as pre-determined by the standard d-scan is used as input, letting CEP be the only parameter to iterate upon until convergence.

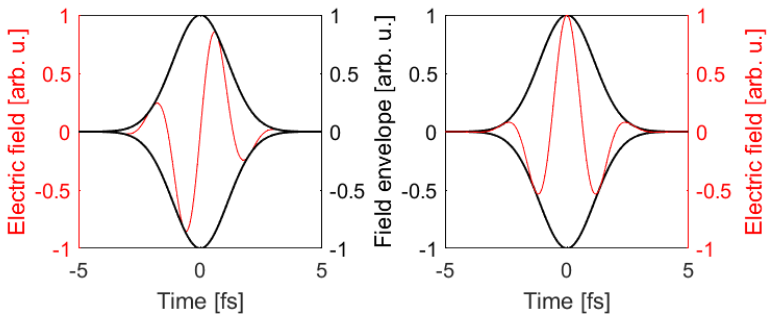

Figure 3.14: Effect of CEP on nearly-single-cycle pulses. The same electric field envelope can have one or two dominant half-cycles. Left: $\varphi_0 = \pi/2$, right: $\varphi_0 = 0$.

In Article III, we apply the above observations to reconstruct the electric field waveform of a pulse from a Ti:Sa-based laser, spectrally broadened in an HCF. The total span of its spectrum was $400-1000$ nm, leading to a significant overlap between the fundamental and its second harmonic. The effective spectral region where the ensuing interference fringes could be analysed was however limited to about $450-470$ nm,

where the intensities of both signals were sufficient for a reliable measurement, as indicated in Fig. 3.15 (c). After determining the spectral phase of the measured pulse using the standard d-scan retrieval, we determine the CEP using Eq. 3.32, allowing us to calculate the exact electric field waveform. The result is shown in Fig. 3.15 (d).

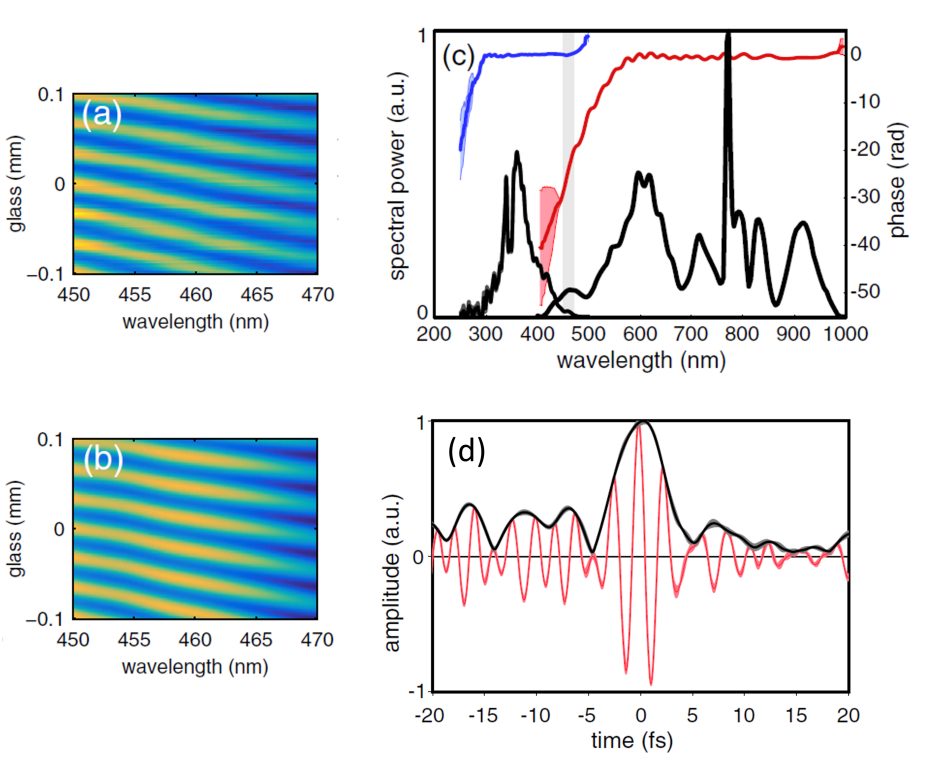

Figure 3.15: CEP-dependent d-scan. (a) Experimental spectrogram, zoom-in on the region of overlap between the fundamental and the second harmonic. (b) Simulated spectrogram (same zoom). (c) Measured spectral intensity (black) and retrieved spectral phase of the fundamental (red) and the second harmonic pulse (blue). Gray shaded area: region of reliable spectral phase retrieval for both pulses. (d) Reconstructed temporal domain amplitude (black) and electric field waveform (red). Adapted from Article III.

3.5.2 Spatio-temporal ultrashort pulse characterisation: Fourier-transform spectrometry

The electric field of optical pulses is frequently described as a product of a purely spatial and a purely temporal component,

$$U(x, y, t) = U_0 \times R(x, y) \times T(t). \tag{3.34}$$

This approximation often breaks down for short pulses, where so-called spatio-temporal couplings (STCs) can have a rather pronounced effect on the pulse properties. Examples of STCs are spatial chirp (coupling between transverse position and frequency), wavefront rotation (transverse position and time), and several other effects. For a great introduction to STCs, the reader is referred to works of the Trebino group[92,93].

The techniques presented or referenced in Sect. 3.5.1 address the issue of spectro-temporal pulse characterisation by implicitly assuming the validity of Eq. 3.34 (spatially integrating the entire pulse or selecting its central portion for the measurement). Several schemes capable of recording STCs have been proposed, offering the addition of spatial information[94,95,96]. In the following, the focus is on the technique for 3D electric field characterisation developed at Lund University[97]. The principle is to infer spatially resolved phase information about a pulse by having it interfere with a well-characterised, spatially homogeneous reference pulse. The practical realisation of the idea is illustrated in Fig. 3.16. The measured pulse is sent into an interferometer, where in the sample arm it travels unaltered, while in the reference arm it gets very tightly focused, dramatically expanding after the focus. This manipulation ensures a large degree of homogeneity and a nearly perfectly spherical wavefront around the reference pulse centre. The two pulses are recombined and their interference pattern is recorded on the chip of a CCD camera. Equipping the reference arm with a translation stage allows to scan the delay between the pulses, generating an interferogram $I(x, y, \tau)$ for each pixel of the camera. Fourier transforming the data along the time axis gives the frequency-domain information needed to reconstruct the measured pulse as described below. Knowing the distance of the focus of the reference beam to the CCD chip allows to calculate the curvature, which can be numerically removed. The measurement is finalised by sending the centre of the reference pulse for d-scan characterisation.

If spatial resolution is available and the reference pulse is fully known, the field of the measured pulse can be deduced from the recorded interference signal $I(x, y, \tau)$. The first step is to Fourier transform $I(x, y, \tau)$ and select a relevant frequency range around the carrier frequency of the pulse, obtaining $A(x, y, \omega)$. The electric field of the measured pulse is then obtained as

$$\tilde{U}(x, y, \omega) = \frac{|A(x, y, \omega)|\, e^{i\tilde{\varphi}(x,y,\omega)}}{\tilde{U}_r(\omega)}\, e^{i\tilde{\varphi}_r(\omega)}, \tag{3.35}$$

where $\tilde{\varphi}$ stands for the phase and $\tilde{U}_r(\omega)\exp\{-i\tilde{\varphi}_r(\omega)\}$ for the electric field of the reference pulse.

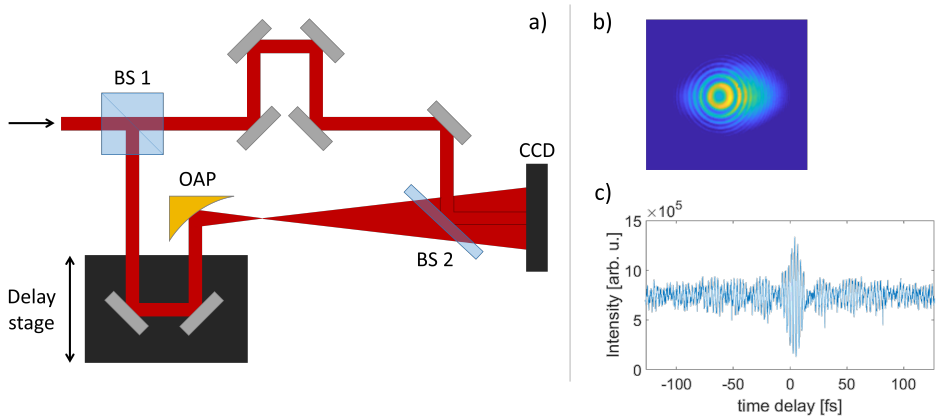

Figure 3.16: Spatially resolved Fourier transform interferometry. a) Experimental set-up. The first beamsplitter (BS 1) divides the pulse in two. One pulse replica remains unchanged, while the other is strongly focused by an off-axis parabolic mirror (OAP, $f = 25$ mm) before recombination on the second beamsplitter (BS 2). The resulting interference pattern (b) is recorded by a camera (CCD) as a function of the delay between the two pulses, yielding a spatially resolved interferogram. c) Interferogram from a single pixel of the CCD.

3.6 4D characterisation of pulses undergoing filamentation

Femtosecond filamentation, described in Sect. 3.4.2, is widely used as a THz-[98], supercontinuum-[99] or few-cycle pulse source[100,101,102]. It has been applied for diverse purposes such as control of electric discharge in air[103] and atmospheric analysis[104]. The fact that it involves an intricate interplay between several non-linear effects makes filamentation a very interesting, albeit challenging, system to operate or model. At the same time, the empirical approach to its study is hindered by the high intensities in the core, which force the experimentator to take their measurements in the far field.

Article VII presents a method capable of full spatio-temporal characterisation of filamenting pulses, including scanning along the length of the filament. In this work, we circumvent the impossibility of placing a detector in the near field by terminating the filament with a sharp pressure gradient[105] at any chosen point, letting the pulses propagate linearly thereafter. 3D electric field detection is performed in the far field by means of spatially resolved Fourier-transform spectrometry[97], described in the previous section, enabling numerical (back)propagation of the filament pulses to any plane of interest, including the termination point. The experimental layout can be seen in Fig. 3.17.

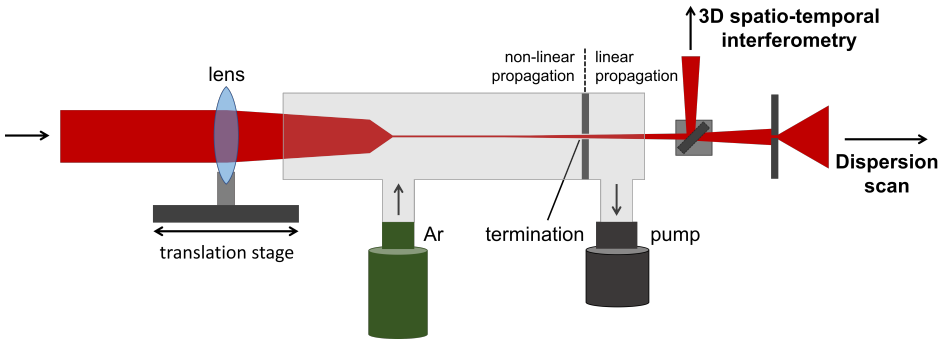

Figure 3.17: Filament generation and characterisation. The filament is formed by focusing Fourier-transform limited pulses in an argon-filled tube, and terminated at a pinhole drilled by the laser pulses in the same configuration in vacuum. The focusing lens is mounted on a translation stage, serving to move the focus with respect to the termination point, effectively arresting the filament at a variable position. The filament pulses reach the exit of the tube through vacuum and are sent for characterisation

Prior to numerical propagation, the recorded field, $\tilde{U}_{\text{rec}}$, needs to be treated to take into account the spectral phase of the reference pulse, $\tilde{\varphi}_r$, and its residual curvature, yielding the field in the plane of detection, d:

$$\tilde{U}_d(x,y,\omega) = \tilde{U}_{\text{rec}}(x,y,\omega)\, e^{i[\tilde{\varphi}_r(\omega) - \sqrt{L^2+x^2+y^2}\, k(\omega)]}, \tag{3.36}$$

where L is the distance from the focus in the probe arm to the CCD chip and $k(\omega)$ the frequency-dependent wavenumber. The propagation from plane d to an arbitrary plane z is done using the Fourier plane wave propagator K_z, applied to the angularly decomposed field $\tilde{U}_d(k_x,k_y,\omega)$, where k_x and k_y are the transverse wavenumbers:

$$\tilde{U}(x,y,\omega;z) = \mathscr{F}^{-1}\{\tilde{U}_d(k_x,k_y,\omega)\; e^{-iK_z(d-z)}\}, \quad K_z = \sqrt{K(\omega)^2 - k_x^2 - k_y^2}, \tag{3.37}$$

where $K(\omega)$ accounts for dispersion, meaning that Eq. 3.37 needs to be applied separately for each material the pulse traverses.

In Article VII we demonstrate the validity and sensitivity of our method by back-propagating the pulses to the filament termination point and tracing the filament dynamics along its length. The upper row of Fig. 3.18 shows the spectral evolution as reconstructed from the recorded d-scan measurements (a), and simulated using the numerically integrated unidirectional pulse propagation equation for the carrier-resolved electric field [106,107] (b). The experimental and simulated data show a good degree of macroscopic agreement on spectral broadening caused by SPM. The spectrum reaches a final width of $575-925$ nm, mostly extending towards lower wavelengths as

the filament length increases, indicative of a strong influence of plasma blueshifting. In the temporal domain, the pulse can be seen to split in two components (bottom row of Fig. 3.18), with a final delay of about 20 fs, consistent with the theoretical predictions. This feature is a signature of dynamic spatial replenishment.

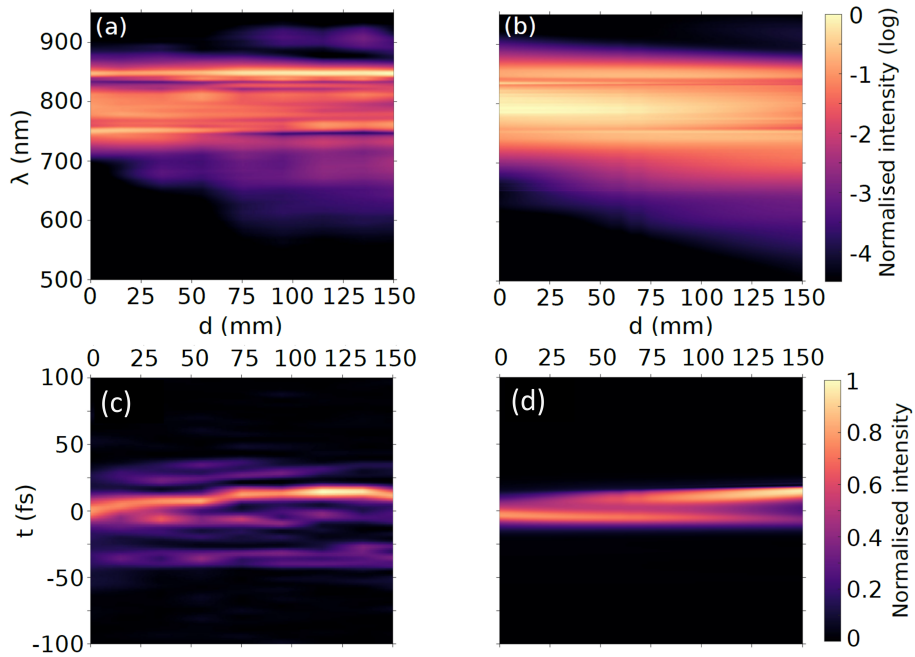

Figure 3.18: Pulse evolution along the filament length. Top: spectral evolution, bottom: temporal evolution. Left: interpolation from measurements at 9 points along the filament length, right: calculations.

By recording the electric field in 3D, the technique offers the possibility to fully reconstruct and visualise pulses from any point inside the filament, propagated to any other point in space. Fig. 3.19 shows such a visualisation of a pulse from a 150-mm-long filament.

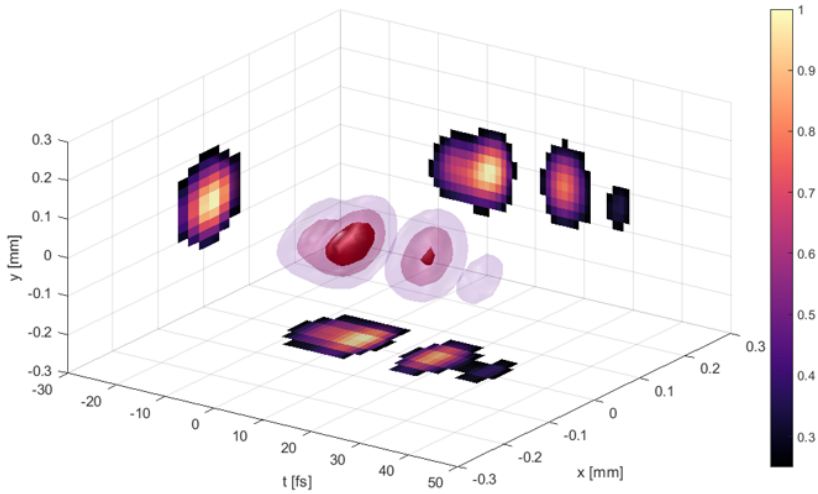

Figure 3.19: 3D view of the pulse undergoing filamentation. The characterised pulse has visibly split in two components, one appearing at 0 fs and the other around 18 fs.

However intuitive, a global picture may obscure important detail. We thus further exploit the potential of our characterisation scheme to examine the inhomogeneities across the profile of a pulse backpropagated to the termination point, for an arbitrarily chosen filament length. We do so by performing a short-time-Fourier-transform time-frequency analysis on selected pixels, gaining insight into the spectral content of the different features in the temporal profile of the pulse. Fig. 3.20 displays the pixel-wise time-frequency decomposition of the pulse from a 150-mm-long filament. The pre-pulse at -50 fs, absent from simulations and likely originating from an optical component such as a coating, is seen to have a frequency distribution unaltered by propagation, demonstrating that it does not participate to the non-linear dynamics. The main pulse, arbitrarily aligned to 0 fs, has a clearly broadened spectrum and a blue-shifted central frequency. As evident from the insets in Fig. 3.20, the relative intensity of the two pulses varies across the beam profile, most notably in the horizontal direction.

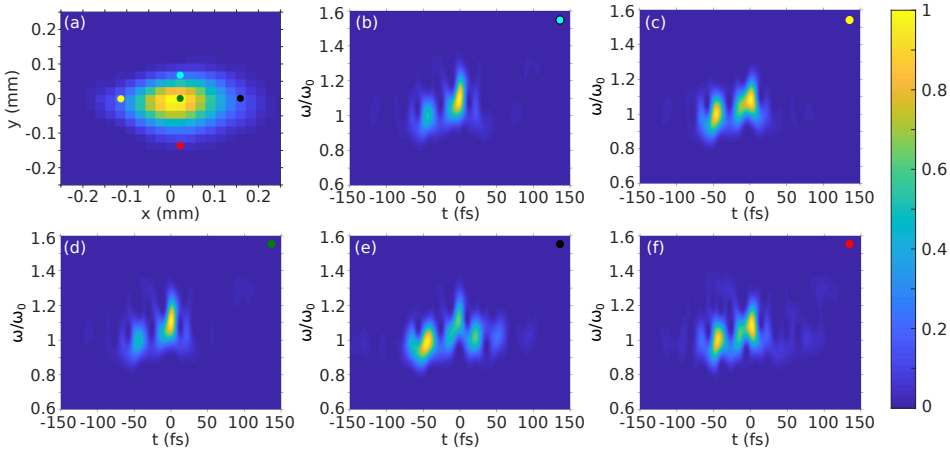

Figure 3.20: Spatially resolved time-frequency analysis. The beam profile features considerable pulse form variations. (a) Cross-section of the beam, (b-f) time-frequency representation of the pulse corresponding to the selected pixels.

The significance of the presented characterisation technique is threefold. Firstly, it opens up the path to in-depth investigation of filament dynamics, offering the possibility to know the electric field at any given point inside a filament. Secondly, it allows the user to identify and extract pulses with desired parameters, which may be generated at a certain point inside the filament, inaccessible without a termination procedure. Lastly, the numerical propagation, which can be adapted to include any sort and number of optical elements that the measured pulse meets, provides a means of predicting the spatially resolved electric field at any point in space. This means that one can assess the properties of the pulse, such as focusability or severity of spatio-temporal couplings, at points where direct measurement would be difficult, for example in high-vacuum chambers. It is worth adding that the presented technique is readily adaptable, easily accommodated to different beam focusing geometries. It is also applicable to liquid and solid filamentation media, where filament termination can be achieved by varying the medium length, making it an exceptionally versatile tool.

Chapter 4

Photoelectron interferometry using attosecond pulse trains

Attoscience has taken up the task of answering the most fundamental question regarding photoionisation: how does the potential landscape of an atom change as one of its electrons leaves it*? This entails accurately describing the reshaping of the atomic potential by the electromagnetic field that led to the ionisation, but also inferring the course of the dynamical rearrangement of charges and energy within the atom. In tackling this problem, use is made of the fact that the potential landscape of the ionised atom leaves an imprint on the phase of the outgoing electron wavepacket (EWP). The diagnostic tool of choice is photoelectron interferometry, a technique with excellent phase-sensitivity in common practical implementations. This chapter gives a brief theoretical description of photoionisation, as well as a presentation of the interferometric technique called RABBIT, used for EWP characterisation during the work on this thesis. Finally, we present the experimental RABBIT setup used in this thesis.

4.1 Laser-induced photoionisation: theoretical framework

To understand the basis for the experimental methods described later in this chapter, we first turn to a simple description of two-photon two-colour photoionisation. In our example, an atom absorbs an XUV (harmonic) photon with the energy $\hbar\Omega > I_p$ and an IR (laser) photon with energy $\hbar\omega$. The order in which the photons are absorbed

*Attoscience also generalises this question to multiple atomic ionisation, as well as photodissociation of molecules and molecular clusters.

is essentially irrelevant; however, cases where the IR photon is absorbed first, taking the atom into a virtual state, are much less probable than ionisation with the XUV photon, so only the latter will be considered. Assuming both fields linearly polarised along the $\hat{z}$ axis, the matrix element describing a two-photon transition from the bound ground state $|g\rangle$ to the final continuum state $|f\rangle$ via the intermediate state $|i\rangle$ can be expressed as[108]:

$$M_{g\to f}^{(\pm)}(\Omega) = \lim_{\varepsilon\to 0^+} \sum\!\!\!\!\!\!\int_i \frac{\langle f|\hat{z}|i\rangle \langle i|\hat{z}|g\rangle}{\mathrm{E}_g - \mathrm{E}_i + \hbar\Omega + i\varepsilon}, \tag{4.1}$$

where E_g and E_i are the ground and intermediate state energy, respectively, and the factor ε, which tends to zero from the positive side, serves to regularise the pole $\mathrm{E}_i = \mathrm{E}_g + \hbar\Omega$. The sum runs over bound, and the integral over continuum intermediate states. The second transition may take place by either absorption or emission of a photon, indicated by the subscript $\pm$.

Eq. 4.1 assumes the existence of one single continuum state $|f\rangle$ with the energy E_f. A more realistic approach takes into account all the different angular momenta of the intermediate and final states. Given that the absorption of a linearly polarised photon is accompanied by an angular momentum change of $\Delta l = \pm 1$, two-photon transitions from a ground state with the angular momentum l_g result in a final-state angular momentum spectrum $L \in \{l_g - 2, l_g, l_g + 2\}$*. Continuum states are characterised by the electron wave vector $\mathbf{k}$, so using $|f\rangle \equiv |\mathbf{k}\rangle$ the matrix element can be re-written as:

$$M_{\mathbf{k}g}^{(\pm)} \propto \sum_{\lambda,L} M_{\lambda Lm}^{(\pm)} Y_{Lm}(\theta,\phi), \tag{4.2}$$

where λ and L are the intermediate- and final-state angular momenta, and m the ground-state magnetic quantum number. Eq. 4.2 is referred to as partial wave expansion and $Y_{Lm}(\theta,\phi)$ represent spherical harmonics. The transition probability amplitude for reaching the final state is

$$\mathrm{A}_{\mathbf{k}g}^{(\pm)}(\tau) \propto F_{\mathrm{IR}}(\omega) F_{\mathrm{XUV}}(\Omega) e^{\pm i\omega\tau} M_{\mathbf{k}g}^{(\pm)}, \tag{4.3}$$

where $F_{\mathrm{XUV/IR}}$ is the XUV/IR spectral amplitude. Note that the result depends on the delay between the two fields, τ. As demonstrated below, this provides the basis for two-color photoelectron interferometry.

*with the obvious exception $L \in \{l_g, l_g + 2\}$ for $l_g \in \{0, 1\}$.

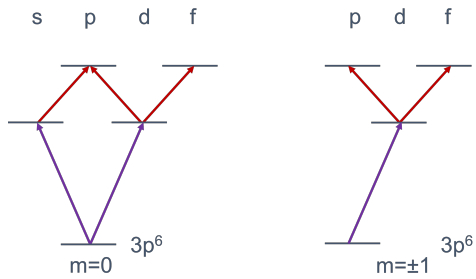

Figure 4.1: Channel-resolved two-photon transitions. Example: possible transitions from the $3p^6$ state in Ar for the case of XUV photon absorption followed by IR photon absorption.

The exposition developed above is limited to monochromatic IR and XUV radiation. This, however, does not correspond to real experimental conditions, where both photons come from short-pulsed sources described in Ch. 3 and hence have a finite spectral bandwidth (see Sect. 3.1). This can be accounted for by a convolution over the respective bandwidths of the IR and XUV pulses.

4.2 Reconstruction of Attosecond Beating By Interference of Two-photon transitions (RABBIT)

The comb-like structure of the HHG spectrum, S_{XUV}, is reflected on the spectrum of photoelectrons it generates, S_{PE}:

$$S_{\mathrm{PE}} = S_{\mathrm{XUV}} \cdot \sigma(\Omega), \tag{4.4}$$

where $\sigma(\Omega)$ is the energy-dependent ionisation cross-section of the target atom. The photoelectron spectrum thus consists of a series of peaks separated by $2\hbar\omega$, ω being the angular frequency of the IR field driving HHG. If $\sigma(\Omega)$ is well known, S_{PE} gives complete information about the XUV spectral amplitude and none about its phase. As first proposed by Véniard et al. [109], and experimentally demonstrated by Paul et al. [4], it is possible to access the XUV phase with the help of an additional IR field with photon energy $\hbar\omega$, at a variable delay with respect to the XUV field. As illustrated in Fig. 4.2, the addition of $\hbar\omega$ photons results in the appearance of so-called sidebands (SB) in the photoelectron spectrum stemming from two processes: (i) simultaneous absorption of an XUV photon from harmonic q–1 (H_{q-1}) and an IR photon, and (ii) absorption of an XUV photon from H_{q+1} followed by emission of an IR photon. There are thus

two* different quantum paths leading to the same state in the continuum (having a kinetic energy $E_{kin} = q\hbar\omega - I_p$, where I_p is the ionisation potential of the target gas). Delaying the IR field with respect to the XUV causes a modulation of the SB_q signal I_q according to:

$$I_q = |A_{q-1}^{(+)}|^2 + |A_{q+1}^{(-)}|^2 + 2|A_{q-1}^{(+)}||A_{q+1}^{(-)}|(\cos 2\omega\tau - \Delta\varphi), \tag{4.5}$$

where $A_{q\mp1}^{(\pm)}$ is the two-photon transition amplitude associated with the transition consisting of the absorption of a $H_{q\pm1}$ photon and the absorption (+) or emission (-) of an IR photon. The sideband oscillation phase, $\Delta\varphi$, originates from two contributions:

$$\Delta\varphi = \Delta\varphi_{XUV} + \Delta\varphi_A, \tag{4.6}$$

where $\Delta\varphi_{XUV} = \arg\left[F_{XUV}(\Omega_{q+1})\right] - \arg\left[F_{XUV}(\Omega_{q-1})\right] \approx 2\omega\tau_{XUV}$ is the group delay of the XUV APT (see Eq. 2.13) and $\Delta\varphi_A = \arg\left[M_{kq}^{(-)}(\Omega_{q+1})\right] - \arg\left[M_{kq}^{(+)}(\Omega_{q-1})\right]$ the so-called *atomic phase*, a consequence of photoelectron scattering on the atomic potential, with the addition of IR-induced transitions in the continuum.

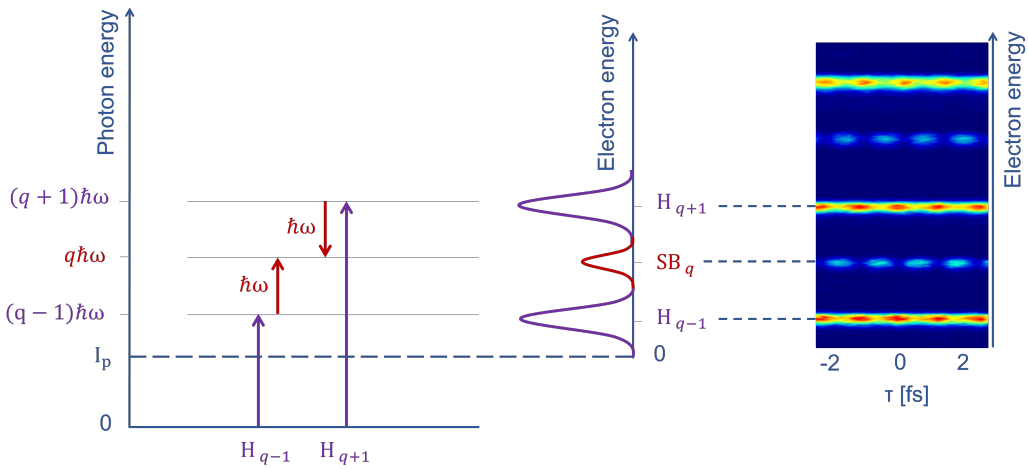

Figure 4.2: Principle of RABBIT. Sideband SB_q appears in the photoelectron spectrum as a result of the H_{q-1}+IR and H_{q+1} − IR transitions. The modulation of the sideband signal with the XUV-IR delay τ encodes information about the atomic potential.

*This statement is valid under the assumption that the IR intensity is insufficient for any higher-order processes.

In the absence of resonances (case colloquially referred to as "flat continuum"), $\Delta\varphi_{\mathrm{A}}$ is small compared to $\Delta\varphi_{\mathrm{XUV}}$[4]. Under the assumption $\Delta\varphi = \Delta\varphi_{\mathrm{XUV}}$, it is therefore possible to use the SB modulation phase to infer to a good approximation the temporal profile of the average pulse in a long APT. This is done by measuring the phase difference between adjacent SBs in the E_{kin} vs. τ[4,6] spectrogram. The protocol was coined Reconstruction of Attosecond Beating By Interference of Two-photon transitions (RABBIT**) by Muller in 2002[6]. It has since reversed its purpose, abandoning the approximation $\Delta\varphi_{\mathrm{A}} \approx 0$ and instead being used precisely to measure the atomic phase. Due to its sensitivity, it has become a ubiquitous tool in photoionisation dynamics studies. Ch. 5 presents results obtained in the Lund Attolab using RABBIT in the course of this thesis.

4.2.1 Rainbow RABBIT

So far, a sideband in the photoelectron spectrum was implicitly considered as a whole, disregarding any potential phase variations across its bandwidth. This is in line with the historical development of RABBIT as an experimental technique: for about 15 years, sideband phase analysis came down to integrating the peak over energy and assigning it a unique phase value. The development of photoelectron detectors has since offered the possibility to abandon this approach thanks to an increase in detection efficiency and energy resolution. In 2016, Gruson et al. introduced an energy--resolved variant of the RABBIT technique[11], often referred to as "rainbow RABBIT", which measures the phase for each resolved energy bin ("colour") within the sideband. Although challenging due to a much lower signal-to-noise ratio compared to energy-integrated RABBIT, its rainbow counterpart gives the possibility to investigate spectrally narrow resonances, as well as distinguish contributions from channels partially overlapping in the electron energy spectrum. An illustration of the rainbow RABBIT is given in Fig. 4.3, where the phase variation across the $1s4p\ ^1\mathrm{P}_1$ and $1s5p\ ^1\mathrm{P}_1$ resonances in helium is retrieved from the energy-resolved delay-dependent signal of SB16. This technique has been applied in Articles IV-VI, and VIII, see Ch. 5.

4.3 Experimental implementation

Any RABBIT setup contains an interferometer, where the driving pulse is split into the pump and probe pulses. High-order harmonics are generated in the pump arm and recombined with the temporally delayed probe in vacuum. Both pulses are focused into the target sample (gas/liquid jet or mechanically supported solid). A spectrometer

**also appearing as RABITT in earlier literature

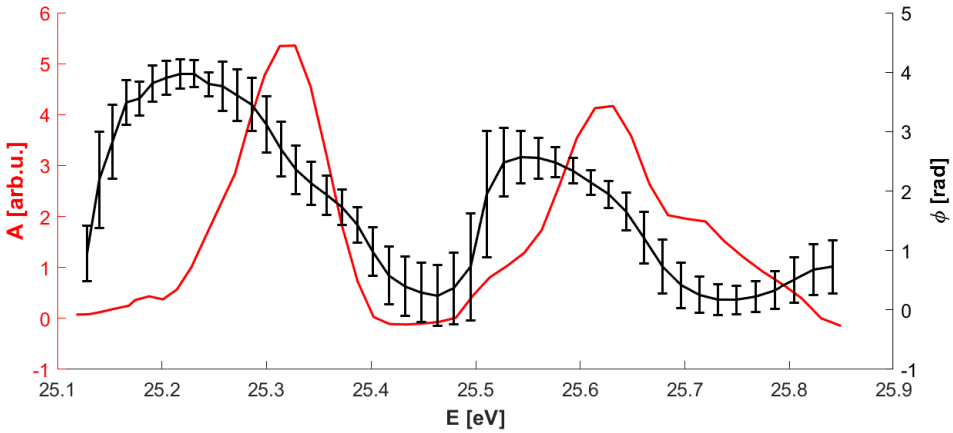

Figure 4.3: Rainbow RABBIT analysis of SB16 in helium. Amplitude (red, peaks not to scale) and phase (black) of SB16 when H15 (ω_{IR} =1.58 eV) is tuned to cover the 1s4p, 1s5p, and 1s6p Rydberg states. The two peaks of the amplitude are the signature of the 4p and 5p resonance (6p appears as a shoulder to 5p); the phase exhibits drops of approximately 3.5 rad across the 4p and 2.5 rad across the 5p resonance.

collects charged interaction products as the pump-probe delay is varied. The rest of this chapter presents the RABBIT setup in the Lund Attolab, used in Articles IV-VI, and VIII (see Chapter 5).

4.3.1 Interferometer

The RABBIT setup is based on a Mach-Zender interferometer with active delay- and beam-pointing stabilisation. A first beamsplitter plate (BS in Fig. 4.4) divides the beam into the "pump" arm, where laser pulses are converted into high-order harmonics, and the "probe" arm, where laser pulses are temporally delayed before combining with the harmonics to create sidebands. The usual pump : probe beamsplitting ratio is 70 : 30. The pump intensity is controlled using an aperture (A). The pump beam is sent on a silver mirror with a hole in the middle, which makes the beam annular, discarding its highest-intensity part. The beam then reflects off an $f = 0.5$ m silver mirror (FM 1) at a small angle and enters a vacuum chamber. Its focus is in the centre of a pulsed generation gas cell (GC) operating at a pressure of a few tens of mbar. The pulsed valve is synchronised to the laser frequency using a master clock based on pulses picked up by a photodiode back in the oscillator. The GC is between 0.6 and 1 cm long and its position can be controlled in all three dimensions using motorised stages for daily alignment (not depicted). After the harmonic generation, the pump beam enters a second vacuum chamber ("recombination chamber") where most of the remaining IR is blocked by a metallic filter (F), usually aluminium. The beam passes through the hole of a drilled silver mirror (HM in Fig. 4.4, for "holey mirror") and

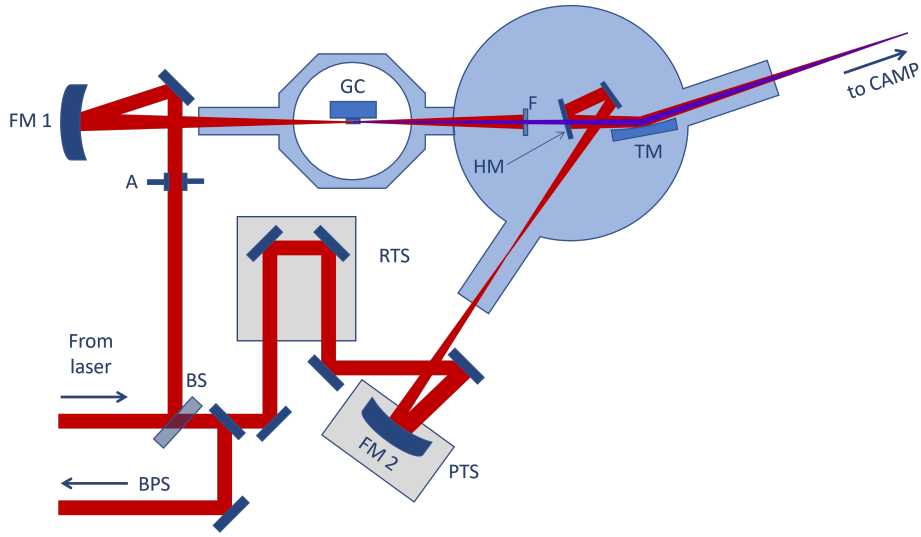

Figure 4.4: RABBIT interferometer. BS - beamsplitter, A - aperture, FM - focusing mirror, GC - generation cell, F - filter, HM - holey mirror, TM - toroidal mirror, BPS - beam-pointing stabilisation, RTS - rough translation stage, PTS - precision translation stage, CAMP - Chamber for Atomic and Molecular Physics, where interaction with target gas and photoelectron detection take place.

arrives at a gold-coated $f = 0.3$ m toroidal mirror (TM) at grazing incidence. The TM images the HHG plane in a $1:1$ configuration to the target gas, in the detection region of the following Chamber for Atomic and Molecular Physics (CAMP)*. The details concerning photoionisation and electron detection are presented in Sect. 4.3.2.

The probe arm contains the delay control and stabilisation units. The beam is first directed to a manual translation stage for rough delay control (RTS). It continues towards an automated piezoelectric precision translation stage (PTS) used to control the pump-probe delay with attosecond precision, required for proper sampling of SB oscillations, which have a 1.33 fs period for pulses with the central wavelength $\lambda_{c,\mathrm{IR}} = 800$ nm. The delay-stabilisation scheme is presented below in Sect.4.3.1. The delay range of the PTS is about 500 fs, corresponding to twice the traversed distance of $\approx 80\,\mu$m. The PTS supports an $f = 0.5$ m mirror focusing the probe beam as it enters the recombination chamber. This particular focusing is done with the purpose of creating a virtual source with a distance to the TM approximately equal to the one between the GC and TM. The probe beam is recombined with the pump by a reflection off the HM, which makes it annular. The HM is held by a motorised mount, enabling high-precision adjustments of the beam angle to ensure good overlap with the pump, which itself cannot be steered**. Finally, the probe is focused along with

*Piece of equipment standardised for ease of adaptation across the AMO community.

**XUV radiation is heavily absorbed in materials. The only possibility to manipulate it is by grazing-incidence reflections off metallic mirrors and even then the losses can be rather high[110].

the pump using the TM.

For the purpose of different RABBIT-based photoelectron spectroscopy experiments, probe arm adaptations are frequent. Control over the intensity is very important because an IR deficiency in the interaction region results in the loss of sidebands in the photoelectron spectrum, while its excess leads to undesirable higher-order processes. An aperture is unfortunately not a good means to employ because changes of IR diameter before focusing have a very pronounced effect on the IR focal volume in the interaction region. This is problematic due to the so-called volume averaging effect, where interaction conditions vary across the sampled gas volume, leading to a decrease of the sideband contrast. The solution is to build an attenuator from a $\lambda/2$-waveplate in combination with a transmission polariser, as was done for Article VIII (see also Chapter 5). This assembly can also be used for probe beam polarisation control. Another item that can be useful in the probe beam is a mechanical chopper - a metal disc with holes rotating at an adjustable frequency, used to block a desired share of probe pulses from reaching the interaction region. XUV+IR photoelectron spectra can then be recorded in alternation with XUV-only ones; this makes it possible to distinguish between contributions to photoelectron peaks in cases when sidebands originating from one channel overlap harmonic peaks resulting from another, like in Articles IV and VI. Lastly, various narrow-band interference filters are used when spectral precision in harmonic probing is needed. This, however, comes at a great cost for the probe intensity, so much so that it is often unfeasible outside regions with rather high ionisation cross-section.

Towards the end of this thesis, the setup was upgraded to provide better stability and precision. This upgraded apparatus was used in Article VIII.

Attosecond delay stability

The pump-probe delay stabilisation is done using a separate interferometer that shares the first beamsplitter with the pump-probe one. As highlighted in yellow in Fig. 4.5, it picks up a small fraction of the IR beams from the pump (before the filter) and the probe, combining them nearly collinearly on the chip of a CCD camera, where the ensuing fringe pattern is recorded. A feedback loop takes the fringe phase as input and acts on the piezoelectric stage in the probe arm of the RABBIT interferometer, maintaining the stability of the relative XUV-IR delay. The interferometer has been measured to have a 40 as RMS stability error over an hour of out-of-loop measurement.

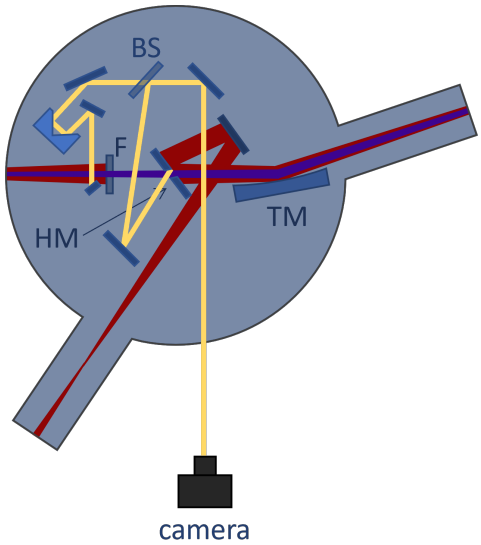

Figure 4.5: Stabilisation interferometer - part of the beam path not shared with the pump-probe interferometer. A small portion of the pump beam is taken out before the IR-blocking filter; in the probe arm, a small leakage through the recombination mirror hole is taken. BS recombines the two and the camera records the interference pattern to provide input for the delay stabilisation feedback loop. Note that the angle of HM is exaggerated for easier beam path illustration.

4.3.2 Photoelectron detection

Upon focusing with the toroidal mirror, the pump and probe beams pass through a differential pumping stage and enter the high-vacuum ($\sim 10^{-8}$ mbar without gas load, $\sim 10^{-6}$ mbar with it) CAMP chamber, where they interact with the target gas. A long nozzle dispenses the gas in the form of a continuous effusive jet. The resulting photoelectrons are then collected by high-resolution kinetic energy, or equivalently momentum, detectors attached to the CAMP. This section describes the types of electron spectrometer used in Articles IV-VI and VIII.

Magnetic bottle electron spectrometer

The Magnetic Bottle Electron Spectrometer (MBES) employs magnetic fields to collect electrons from the light-gas interaction region and guide them to a detector[111]. The kinetic energy of the electrons is inferred from the time it takes them to traverse the length of the MBES. As illustrated in Fig. 4.6, a strong permanent NdFeB magnet ($\sim$ 1T on the surface) creates an inhomogeneous field pushing the nascent photoelectrons into a long (2 m) tube. Once inside, they are guided by a weaker, homogeneous magnetic field generated by a solenoid wrapped around the tube (not

depicted in Fig. 4.6). A mu-metal (high magnetic permeability Ni-Fe alloy, gray in Fig. 4.6) case provides a shield from external magnetic fields, such as that of the Earth. At the end of this so-called flight (or drift) tube, the electrons reach a MicroChannel Plate (MCP) electron multiplier. This way, a detectable signal is generated from a single electron, received by an analog-to-digital converter and managed by a data acquisition card. The acquisition is triggered by laser pulses picked up by a photodiode, ensuring perfect synchronisation between the detection and the generation of events to detect.

The kinetic energies of photoelectrons generated by HHG radiation are non-relativistic (up to ≈ 100 eV in the Lund Attolab) and as such can be inferred from the electron time of flight using:

$$E_{\text{kin}} = \frac{m_e}{2}\left(\frac{L}{t + t_d}\right)^2, \tag{4.7}$$

where m_e and e are the electron mass and charge, respectively, L the flight length, t the measured time of flight, and t_d the sum of any delays caused by signal transport.

The data acquisition card has a finite sampling rate, f_s, which sets a lower limit to the electron time of flight delay discernible by the MBES, $\Delta t = 1/f_s$. The kinetic energy resolution is in turn limited to $\Delta E \sim L^2\, t^{-3} \Delta t$. It is clear that ΔE is not constant across the energy spectrum due to the cubic relation to the time of flight. It is therefore customary to express MBES resolution in terms of $E/\Delta E$, describing how the spectral resolution decreases with the increase of kinetic energy. The problem of lower resolution for high-energy electrons can be mitigated by applying a negative

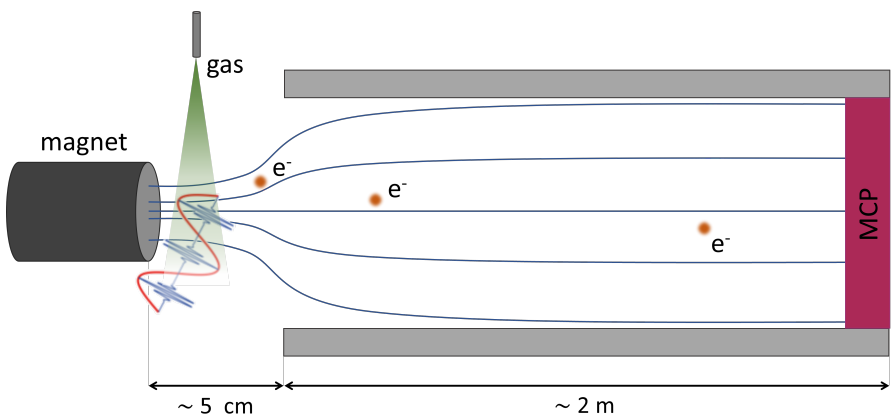

Figure 4.6: MBES operation principle. A bottle-shaped magnetic field guides electrons to an MCP, where their times of flight are detected.

voltage (often referred to as retarding or offset voltage) at the entrance to the flight tube, serving to slow electrons down. This method can be used to bring even the fastest electrons into the few-eV energy range (adding a linear correction to Eq. 4.7), with the caveat in that former low-energy electrons can no longer be detected.

Other factors limiting the energy resolution are the response function of the spectrometer, as well as the finite volume of the interaction region. These effects can be numerically removed from recorded data using deconvolution procedures, such as the iterative one often applied to Attolab data, based on the blind Lucy-Richardson algorithm[112,113]. The estimated resolution of the Attolab MBES is $E/\Delta E \geq 80$, which is a rather high number.

The described MBES instrument is a courtesy of Raimund Feifel and Richard Squibb from Gothenburg University.

Velocity-map imaging spectrometer

In instances when angular resolution is needed (e.g. experiments aiming at distinguishing photoelectrons having the same kinetic energy but different angular momenta), the angle-integrating MBES must be replaced by an instrument such as the Velocity-Map Imaging Spectrometer (VMIS)[114]. In it, an annular repeller electrode directs photoelectrons away from the interaction region and into a flight tube ($\sim$ 10 cm, significantly shorter than in MBES), where they are accelerated by another annular electrode called the extractor (see Fig. 4.7). Unlike the MBES, electrons are allowed a free radial expansion as they drift towards the MCP detector at the end of the flight tube. As a result, same-energy electrons retain a spherical locus throughout the flight. Their projection on the perpendicular plane is observed with a phosphor screen imaged by a CCD. An example of a VMIS image is shown in Fig 4.8.

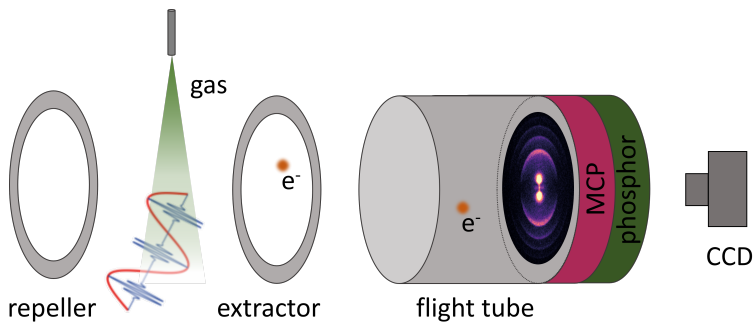

Figure 4.7: Principle of VMIS. An electrostatic lens made up of annular electrodes guides electrons towards an MCP followed by a phosphor screen and a camera. Same-energy electrons form ring-like structures on the detector.

In order to reconstruct the photoelectron momentum distribution from raw images, it is necessary to apply an inverse Abel transform algorithm [115]. There are different computational approaches to this, all of which produce certain artifacts upon image inversion. The type of error produced is specific to the applied method, meaning that misinterpretation of data can be avoided by a careful choice of algorithm. By far the fastest procedure, called pBASEX [116], makes use of the fact that any cylindrically symmetric distribution can be decomposed into a set of Legendre polynomials according to [117]:

$$\frac{d\sigma}{d\Omega} = \frac{\sigma_0}{4\pi}\left[1 + \sum_{n=1}^{\infty} \beta_i P_i(\cos\theta)\right], \tag{4.8}$$

where σ is the fully differential cross-section, Ω the solid angle, σ_0 the total cross-section, β_n the so-called n^{th} asymmetry parameter, θ the polar angle, and $P_n(\cos\theta)$ the n^{th} Legendre polynomial. The pBASEX algorithm tunes a set of asymmetry parameters up to a pre-determined order, in an attempt to fit the resulting distribution to the recorded raw image. In contrast with its speed (seconds to minutes for an entire RABBIT scan, depending on the image resolution), a big drawback of this method lies in the fact that it produces nonsensical information in the centre of the image, making it useless for observation of low-kinetic-energy electrons. The problem is aggravated if the signal in the image centre is very strong (low-kinetic-energy electrons from an atomic resonance or detector saturation due to other causes); in this case the mathematical artefacts appear even at larger radii and the image reconstruction is likely to be unreliable. In cases when computational speed can be sacrificed for low-energy resolution, the best solution are methods based on iterative reconstruction [118]. This type of algorithm is inaccurate in calculating the electron distribution along the polarisation axis, but these inaccuracies are usually limited to a few-degree

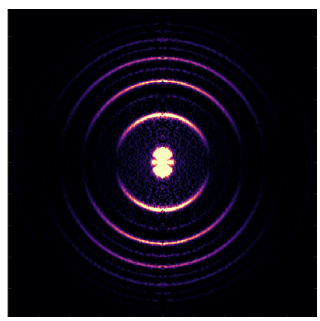

Figure 4.8: Iteratively inverted VMIS image. This photoelectron distribution was obtained by tuning H15 to the 3p resonance in He. The central feature is SB16, followed by alternating harmonic and sideband features as one radially moves out of the centre.

angle, which can be discarded from the data set without significantly compromising its completeness.

Taking the spot in the image corresponding to zero-kinetic-energy electrons as a reference, electrons with the energy E_k will form a ring with the radius

$$r = \sqrt{\frac{L^2 E_k}{eV}}, \tag{4.9}$$

where L is the flight tube length, e the electron charge, and V the voltage between the electrodes (typically $\sim$ kV).

Chapter 5

Studies of photoionisation dynamics in the time and frequency domain

As discussed in Chapter 1, one of the goals of attoscience is to gather time-resolved information about photoionisation. The first two sections of this chapter elaborate on the type of information we are currently able to obtain. The final section presents experimental results recently obtained in Lund, demarcating the frontiers of present-day attoscience.

5.1 Time delays in photoionisation

Having absorbed a photon with an energy in excess of the ionisation potential, the electron leaves the vicinity of the nucleus. As it scatters off the ionic potential*, the photoelectron wavepacket acquires an energy-dependent phase, as illustrated in Fig. 5.1. The ensuing group delay, equal to the energy-derivative of this phase, manifests itself as a time delay between the scattered EWP and its plane-wave counterpart travelling in field-free space. The total EWP delay can be decomposed into a long-range contribution, resulting from the asymptotic Coulomb potential at a large distance from the nucleus, and a short-range correction. It is impossible to define a distance at which the phase shift due to the infinite-range Coulomb potential has converged to a finite value; however, if considerations are restricted to a given angu-

*The process is often referred to as *half-scattering*, since the EWP only traverses half of the ionic potential.

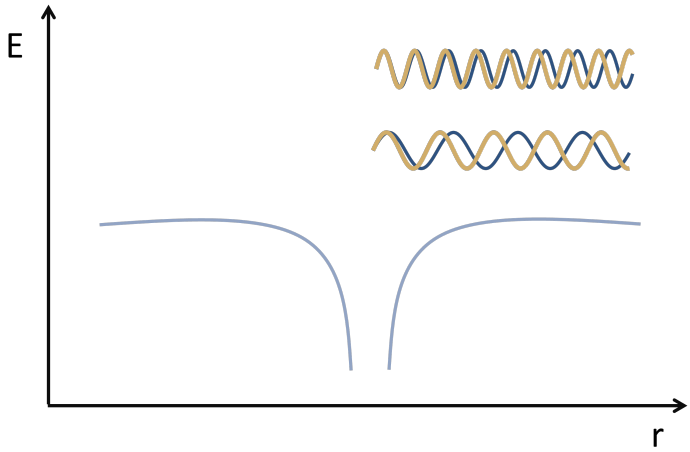

Figure 5.1: Electron wavepacket phase. As it moves away from the nucleus, the photoelectron wavepacket scatters off its attractive potential. This results in a phase shift between the energy-dependent phase the wavepacket acquires (yellow) compared to that of a wavepacket outside any field (blue).

lar momentum l, the asymptotic value of the radial wavefunction can be expressed as [108,119]:

$$\lim_{r\to\infty} R_l(k,r) = \sqrt{\frac{2}{\pi k}}\,\frac{1}{r}\,\sin(kr + \varphi_{\mathrm{EWP}}), \tag{5.1}$$

where k is the local momentum, connected to energy E and local potential $V(r)$ through

$$k = \frac{\sqrt{2m_e[E - V(r)]}}{\hbar}. \tag{5.2}$$

The EWP phase can be expanded into

$$\varphi_{\mathrm{EWP}} = \frac{Z\ln(2kr)}{k} + \eta_l(k) - \frac{\pi l}{2}, \tag{5.3}$$

The first term stems from the long-range Coulomb potential, with Z as the ion charge, the second term is the scattering phase, and the third originates from the centrifugal barrier. The corresponding group delay is [120]

$$\tau_{\mathrm{EWP}} = \hbar \frac{\partial}{\partial E}\left[\frac{Z\ln(2kr)}{k} + \eta_l(k) - \frac{\pi l}{2}\right] \tag{5.4}$$

$$= \hbar \left[\frac{\partial}{\partial E}\frac{Z\ln(2kr)}{k}\right] + \hbar \frac{\partial \eta_l}{\partial E} \tag{5.5}$$

$$= \Delta\tau_{\mathrm{Coul}}(k, r) + \tau_{\mathrm{W}}(k, l). \tag{5.6}$$

$\Delta\tau_{\mathrm{Coul}}(k, r)$ describes the universal distance-dependent delay caused by the attractive potential of the remaining ion, whereas $\tau_{\mathrm{W}}(k, l)$ is atom-specific. The latter consists of a universal Coulomb contribution $\sigma_l(k)$, equivalent to the delay upon scattering on the potential of the positive hydrogen ion, and $\delta_l(k)$, resulting from electron correlations, which cause a deviation from a perfect Coulomb potential in the vicinity of the ion. The latter can thus serve as a probe for the potential landscape experienced by the outgoing EWP. The group delay $\tau_{\mathrm{W}}(k, l)$ was initially introduced theoretically around 1950 by Eisenbud[121] and Wigner[122], followed by the work of Smith[123] and is therefore referred to as Wigner or Eisenbud-Wigner-Smith (EWS) delay. Given that it lies in the attosecond range, it has, however, only recently (2010) become experimentally accessible[7,124] owing to the development of ultrafast techniques such as RABBIT (see Sect. 4.2).

5.2 Measuring photoemission time delays using RABBIT

As described in the previous section, measuring photoionisation time delays is a means of probing the ionic potential. They were first recorded in 2010 by Schultze and colleagues[124], who measured the relative time delay of electron wavepackets from $2s$ and $2p$ subshells in neon. Since then, photoemission time delays have been recorded in a multitude of different atomic[7,125,126,127,128] or molecular[14,129,130] species in the gas phase, but also liquids[131] and solids[132,133]. This section discusses how the RABBIT technique (see Ch. 4) can be applied to study photoemission time delays, providing the necessary framework for the ensuing presentation of experimental results obtained in the scope of this thesis.

Single ionisation channel

Expression 4.2 introduces the overall matrix element for an XUV+IR two-photon transition as a sum over ionisation channels with different intermediate quantum numbers. It can be shown[108] that this matrix element involves two contributions, one

pertaining to single-photon ionisation by the XUV, and the other to the continuum--continuum (cc) transition triggered by the IR. Its phase is equal to the sum of single--XUV-photon and IR-induced phase terms. More specifically, the phases involved are:

a) phase of the XUV field,

b) scattering phase from ionisation by the XUV,

c) phase of the IR field,

d) cc-phase.

As detailed in Sect. 4.2, phase information can be experimentally accessed using the RABBIT method. The delay-dependent signal of SB_q (Eq 4.5) can be re-written more explicitly as*:

$$I_q = |A_{q-1}^{(+)}|^2 + |A_{q+1}^{(-)}|^2 + 2|A_{q-1}^{(+)}||A_{q+1}^{(-)}| \cos[2\omega(\tau - \tau_{\mathrm{XUV}} - \tau_{\mathrm{W}} - \tau_{\mathrm{cc}})] \quad (5.7)$$

and the stated group delays can be expressed through the corresponding phase-shifts using the finite difference approximation for the energy-derivative:

$$\tau_{\mathrm{W}} = \frac{\Delta\varphi_W}{2\omega}, \qquad \tau_{\mathrm{cc}} = \frac{\Delta\varphi_{cc}}{2\omega} \quad (5.8)$$

Their sum makes up the atomic delay, derived from the atomic phase introduced in Eq. 4.6:

$$\tau_{\mathrm{A}} = \tau_{\mathrm{W}} + \tau_{\mathrm{cc}}. \quad (5.9)$$

τ_{W} and τ_{cc} lie in the below-femtosecond range and tend to be large close to the ionisation threshold [108]. Neither can be individually accessed from a single RABBIT measurement of a sideband phase. The reason for this lies in the fact that, as indicated in Eq. 5.7, the extracted phase consists of multiple components, none of which can be directly distinguished or eliminated. This issue is currently circumvented using two mutually non-exclusive approaches - experimental and theoretical referencing, described in the following.

*The signs of the delay contributions can be found to differ across literature; this is a matter of convention applied to the direction of the time axis.

Since τ_{XUV} represents the imprint of the harmonic spectral phase on the EWP group delay and as such does not result from the ionisation process, it is desirable to eliminate it from the extracted time delay. A common practice is to reference the sideband of interest to the sideband of the same order, but generated in another target, where the atomic phase is approximately flat and the associated delay consequently close to zero. We apply this method in Article V by comparing SB $54-62$ in Xe with the ones in Ne, known to feature very small τ_{A} in the given energy range[134]. Otherwise, one can reference the measured SB signal to one from another ionisation process in the same target, like we do in Articles IV and VI.

The described procedure for the elimination of τ_{XUV} provides the value of the atomic time delay τ_{A} characteristic of the studied two-photon transition. It is important to stress that the result is in this case in the form of a *time delay difference* between two different transitions (for example, $\tau_{3s} - \tau_{3p}$ in Ar in Article VI). Assessing τ_{W}, which represents the single-photon transition time delay (or once again more precisely, time delay difference) can be done by subtracting analytically calculated values of τ_{cc} from the experimentally obtained ones for τ_{A}.

Ionisation via multiple channels

As discussed in Sect. 4.1, most cases of two-photon ionisation imply the existence of more than one intermediate as well as final states. Angle-integrated measurements (like those performed using an MBES, presented in Chapter 4.3.2) cannot directly distinguish electrons with the same kinetic energy originating from states with different l or m quantum numbers. For this reason, the contributions of different final states to the time-dependent yield of SB_q add up incoherently:

$$I_q = \sum_{L,m} \left| \sum_{\lambda} \left(A^{(+)}_{L\lambda m} + A^{(-)}_{L\lambda m} \right) \right|^2, \tag{5.10}$$

where $A^{(\pm)}_{L\lambda m}$ is the complex amplitude for the two-photon transition from the ground state with magnetic quantum number m via the intermediate state with the angular momentum λ to the final state with the angular momentum L. The superscript $(\pm)$ refers to the absorption $(+)$ or emission $(-)$ of the IR photon.

If the final states are several while there is a single intermediate state (as in the case of helium, right panel of Fig. 5.2), the two ionisation channels share the same Wigner phase, while the *cc* phase slightly depends on angular momentum. The presence of multiple intermediate states (like in argon, left panel of Fig 5.2) further complicates the situation, leading to a loss of sideband oscillation contrast and a global phase that

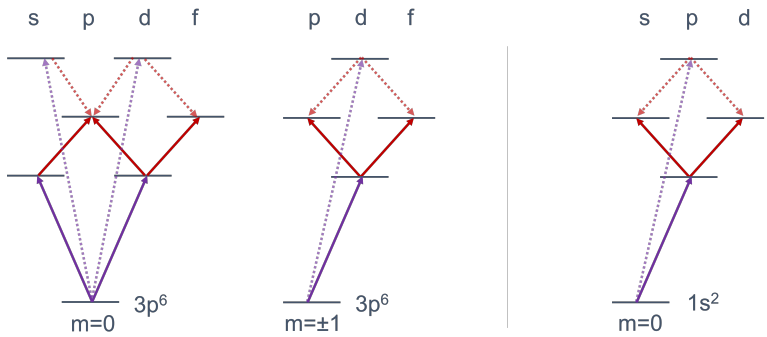

Figure 5.2: RABBIT scheme in case of multiple ionisation channels. Left: argon, right: helium. Solid line: absorption path, dashed line: emission path.

does not correspond to any of the phases of the individual channels. Namely, when performing RABBIT on such type of system, the photoelectron signal corresponding to a given final state consists of two or several contributions associated with differing atomic phases φ_{A}, all of which oscillate at twice the probe field frequency, but with different phases. In case of channels of comparable strength, this leads to interference, whereas in case of one strongly dominant channel, it is that channel that dictates the overall RABBIT phase. The recovery of the one-photon Wigner phases for each channel is thus impossible.

5.2.1 Angle-resolved measurements

Using an instrument like the VMIS, presented in Sect. 4.3.2, grants one access to the angular distribution of photoelectron momenta in the plane parallel to the pump and probe propagation and polarisation directions. The significant advantage presented by the angular resolution of the photoelectron signal lies in the fact that the different partial waves involved in the observed transition have different spatial probability distributions and therefore produce different photoelectron angular distributions (PADs) upon measurement. Due to their interference, their relative strengths and phases leave an imprint on the total PAD, which can in turn be used to retrieve information about the channel-wise ionisation dynamics.

As mentioned in Sect. 4.3.2, in cases where the PAD features cylindrical symmetry, it can be fully parametrised in terms of Legendre polynomials $P_n(\cos\theta)$ and asymmetry parameters β_n. One- (XUV) and two-photon (XUV+IR) PADs, corresponding to the absorption of harmonic $q \pm 1$ and creation of sideband q in the angle-resolved photoelectron spectrum, can thus be expressed as follows:

$$I_{q\pm1}(\theta) = \frac{\sigma_0^{(1)}}{4\pi}\left[1 + \beta_2^{(1)}\, P_2(\cos\theta)\right] \tag{5.11}$$

$$I_q(\theta) = \frac{\sigma_0^{(2)}}{4\pi}\left[1 + \beta_2^{(2)}\, P_2(\cos\theta) + \beta_4^{(2)}\, P_4(\cos\theta)\right], \tag{5.12}$$

where $\sigma_0^{(n)}$ is the angle-integrated n-photon ionisation cross-section, $\beta_i^{(n)}$ the i^{th}-order n-photon asymmetry parameters, $P_i(\cos\theta)$ the i^{th}-order Legendre polynomials, and θ the electron emission angle with respect to the polarisation direction. The azimuthal symmetry allowing the presented decomposition is granted assuming that the involved photons have linear, and moreover parallel, polarisations. Owing to the matching parity of the final-state PADs, the odd-order two-photon asymmetry parameters in Eq. 5.12 identically vanish. Note that the highest order of Legendre polynomials is equal to twice the number of photons involved in the transition[135], $n = 2N = 4$. The β-parameters provide a complete description of the PAD. They encode information about the relative phase of the partial waves and serve as a means of PAD reconstruction and comparison with theoretical calculations, also providing a convenient, compact way of quantifying angle distributions.

We now wish to extend the above considerations to the context of angle-resolved RABBIT measurements. The recorded two-photon PADs in this case result from the interference of one absorption and one emission quantum path for each angular momentum channel. In the total PAD, the final states with different angular momentum l add coherently, whereas the states with different magnetic quantum number m add incoherently. The time-delay-dependent angular distribution of photoelectrons from sideband q in its most general form thus reads:

$$I_q(\theta, \varphi, \tau) = \int_0^{2\pi} d\varphi \sum_m \left| \sum_{l,\lambda} \left[A^{(+)}_{l\lambda m}(\theta, \varphi, \tau) + A^{(-)}_{l\lambda m}(\theta, \varphi, \tau) \right] \right|^2, \tag{5.13}$$

where $A^{(\pm)}_{l\lambda m}$ represents the probability amplitude for a two-photon transition into a final state with angular momentum l via the emission $(-)$ or absorption $(+)$ path through the intermediate state with angular momentum λ from the initial state with magnetic quantum number m. As mentioned earlier, for parallel linear polarisations of the XUV and IR photons, the dependence on the azimuth φ vanishes and in analogy to the angle-integrated case described by Eq. 4.5, the time-dependent, angle-resolved signal of sideband q can be expressed as

$$I_q(\theta,\tau) = A(\theta) + B(\theta)\cos\left[2\omega\tau - C(\theta)\right], \tag{5.14}$$

where $C(\theta) = \Delta\varphi_{\mathrm{XUV}} - \Delta\varphi_{\mathrm{A}}(\theta)$. Note that in this expression $\Delta\varphi_{\mathrm{XUV}}$ does not depend on the emission angle θ. This is easily understood since its origin is in the HHG process, which leaves the same imprint on the electron wavepacket phase, no matter the angular channel. Thanks to that, the atomic phase $\Delta\varphi_{\mathrm{A}}(\theta)$ can be extracted from the measurement. The way of doing this is via so-called h-functions[136]:

$$I_q(\theta,\tau) = h_0 + h_2 P_2(\cos\theta) + h_4 P_4(\cos\theta), \tag{5.15}$$

which represent the projections of the PAD on the orthogonal Legendre polynomials of orders $0, 2$, and 4 and read:

$$h_i(\tau) = a_i + b_i\cos\left(2\omega\tau - \varphi_i\right). \tag{5.16}$$

As detailed in a recent article by Joseph and coworkers[136], several relevant parameters describing the two-photon ionisation process can be obtained by extracting the nine $(a_i, b_i, \varphi_i,\ i \in \{0,2,4\})$ parameters from the experimental data. The first step is to get the h-functions for the recorded time-dependent PAD from a numerical fit according to Eq. 5.15. For example, the Fourier transform of h_i gives access to a_i, which represent the mean value of the oscillatory signal or, in other words, the zero--frequency components in the oscillation spectrum. The delay-integrated values of PAD asymmetry parameters can then be recovered as:

$$\beta_2 = \frac{a_2}{a_0}, \quad \beta_4 = \frac{a_4}{a_0}. \tag{5.17}$$

The supplementary material of the Joseph article provides the expression for the phase $C(\theta)$ from our Eq. 5.14:

$$C(\theta) = -\arctan\left[\frac{b_0\sin\varphi_0 + b_2\sin\varphi_2 P_2(\cos\theta) + b_4\sin\varphi_4 P_4(\cos\theta)}{b_0\cos\varphi_0 + b_2\cos\varphi_2 P_2(\cos\theta) + b_4\cos\varphi_4 P_4(\cos\theta)}\right]. \tag{5.18}$$

The parameters b_i correspond to the oscillation amplitude of the respective h-functions, whereas φ_i represent the oscillation phase, meaning that they, too, are available from the h-function Fourier transform. This finally provides access to the angle-resolved atomic phase φ_{A}.

Although the method presented above gives information on the interference between the different partial waves involved in the studied two-photon transition, it still requires the support of theory to infer their respective contributions to the atomic phase and the associated photoemission time delays. Recently, techniques have emerged using global PAD fitting procedures to extract channel-specific one-photon-transition time delays[137,138].

5.3 Experimental studies

5.3.1 Shape resonance in molecular nitrogen

A shape resonance is a case where an electron, liberated from an atom or molecule using photons from a specific energy range above the I_p, gets temporarily trapped close to the ion due to the shape of the centrifugal barrier. In Article IV we apply the RABBIT technique to study the dynamics of photoionisation through the $3\sigma_g^{-1}$ shape resonance in N2. We detect photoelectrons in an angle-integrated manner using an MBES. In particular, we investigate time delays associated with different vibrational levels from two different states in order to infer the role of nuclear motion during the photoionisation process. We thereby test the limits of the Franck-Condon approximation, which states that molecular nuclei can be considered motionless on the time-scale of electronic transitions.

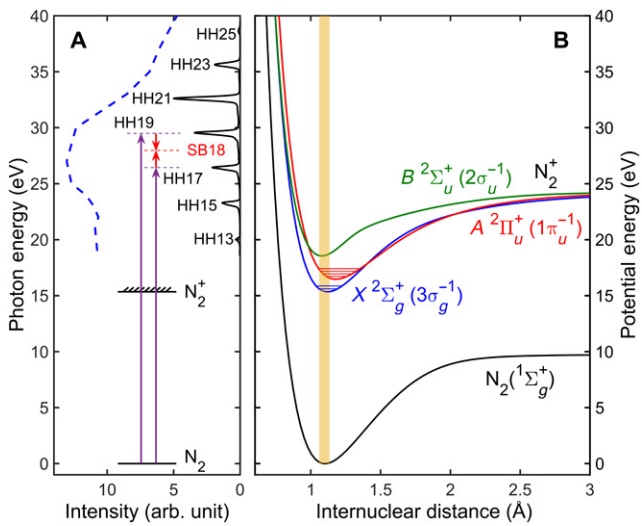

Figure 5.3: N2 photoionisation scheme. A) Harmonics of orders 13-25 are used to probe the $3\sigma_g$ shape resonance in $N2^+$ using the RABBIT technique, indicated in violet (XUV pump) and red (IR probe) arrows. Blue dashed line: photoionisation cross-section. B) Potential energy curves of the ground state of N2. Yellow-shaded area: Franck-Condon region. Adapted from Article IV.

As depicted in Fig. 5.3, we use harmonics of order $15-27$ of the fundamental IR field centred at $\hbar\omega = 1.55$ eV, generated in argon, to ionise N_2 from its ground state $^1\Sigma_g^+$. The resulting photoelectron spectrum features strong contributions from the $1\pi_u$ and $3\sigma_g$ orbitals, corresponding to ions in the $A^2\Pi_u^+$ and $X^2\Sigma_g^+$ states (in further text: A and X state, respectively). Each state further comprises several vibrational states, resolved in the photoelectron spectrum. The difference in energies of the A and X states (≈ 1.5 eV) is such that their features in the photoelectron spectrum overlap upon XUV+IR ionisation with the given photon energies. Since it is the one-photon ionisation peaks from one state that overlap the sidebands from the other and vice versa, we are able to disentangle them by blocking the probe beam in every other laser shot using a rotating mechanical "chopper", allowing us to record a differential photoelectron spectrum, as shown in Fig. 5.4 (b). Varying the pump-probe delay, we likewise record a differential RABBIT scan, shown in Fig. 5.4 (a), by subtracting the XUV-only signal from the XUV+IR one. This permits us to assign the observed photoelectron peaks to their respective states, displayed in Fig. 5.4 (c), and in turn measure the associated photoionisation time delays. We do so by extracting time-delay differences for $v' = 0$ and $v' = 1$ vibrational levels of the A and X state, shown in Fig. 5.5. It is worth noting that the orientations of the N_2 molecules in this experiment were random, and the electron emission angles unknown. For this reason, the measured two-photon molecular ionisation time delays cannot be decomposed as $\tau_{\mathrm{mol},2p} = \tau_{1p} + \tau_{cc}$. Nevertheless, they do reflect one-photon ionisation dynamics. We find that the delay between photoelectrons from $v' = 0$ levels of the two states reaches about $\tau_{\mathrm{X}}(v' = 0) - \tau_{\mathrm{A}}(v' = 0) = 60$ as for a photon energy of 32 eV (Fig. 5.5 (a)). Given that the shape resonance is only present in photoionisation

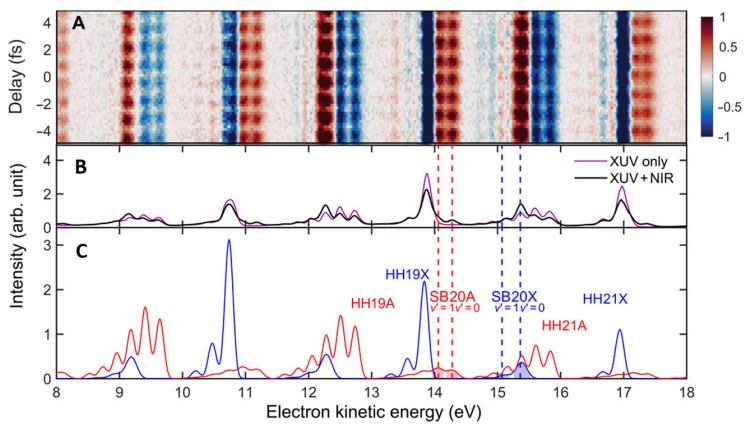

Figure 5.4: Photoelectron spectra in N2. A) Differential RABBIT spectrogram, obtained as a difference of XUV+NIR and XUV-only spectrograms. B) Photoelectron spectrum (PES) for XUV-only (violet) and XUV+NIR (black) photoionisation, averaged over all relative delays. C) Theoretical PES for XUV+NIR photoionisation to the X (blue) and A (red) states. Adapted from Article IV.

from the X state, this result is a direct measure of the delay caused by the centrifugal barrier. We go on to compare the time-delay differences associated with $v' = 0$ and $v' = 1$ vibrational levels in each of the A and X states (Fig. 5.5 (b,c)). In the case of the A state, the measured delay difference is constant as a function of energy and furthermore tends to zero, in accordance with the Franck-Condon principle. The X state, however, exhibits a molecular time delay difference variation up to 200 as between the $v' = 0$ and $v' = 1$ levels. We use theoretical calculations performed by the group of Fernando Martín from Universidad Autónoma in Madrid to show that this difference in photoemission delays originates from the fact that the internuclear distances in the two levels differ by 2 pm, effectively sustaining a wider potential barrier for the $v' = 0$ state compared to the one for $v' = 1$. As a result, the $v' = 0$ photoelectrons are delayed with respect to their $v' = 1$ counterparts, demonstrating that the Franck-Condon principle no longer holds in the vicinity of the $3\sigma_g$ shape resonance.

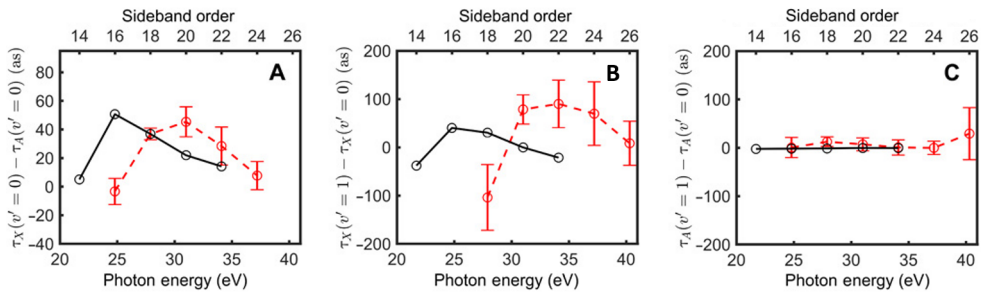

Figure 5.5: Relative molecular time delays in N2. Time-delay difference between (A) X and A states for v'=0, (B) v'=1 and v'=0 vibrational levels in the X state, (C) v'=1 and v'=0 vibrational levels in the A state. Red: experimental data, black: calculations. Adapted from Article IV.

5.3.2 Giant dipole resonance in xenon

In Article V, we study dynamics of photoionisation from the $4d$ shell in Xe in the photon energy range spanning from 70 to 100 eV. We focus on this particular energy region because it features multiple interesting phenomena:

a) the so-called giant dipole resonance, a spectrally broad (tens of eV) resonance sustained by the collective oscillation of all electrons from the $4d$ shell and resulting in a large enhancement of the photoionisation cross-section peaking around 100 eV;

b) an anomalous branching ratio of Xe^+ states subject to spin-orbit (S-O) splitting, $^2D_{5/2}$ and $^2D_{3/2}$, caused by relativistic effects close to the ionisation threshold;

c) opening of several Auger decay channels, where electrons from the $5s$ and $5p$ shell recombine with the $4d^{-1}$ hole, transferring part of their energy to another electron, which is then liberated from the ionic potential (see Fig. 5.6).

We use the RABBIT technique to measure the energy-dependent photoionisation time delay resulting from the combination of the above-listed processes. A rather challenging aspect of this experiment is the spectral congestion caused by the presence of the different Auger channels, as well as the S-O splitting. To facilitate the assignment of different photoelectron peaks, we resort to coincidence spectroscopy. In this technique, the density of the target gas and the XUV flux are reduced to the point where the incidence of photoionisation is significantly lower than one event per laser shot. That way, although most of the shots recorded by the MBES (see Sect. 4.3.2) carry no information and thus get discarded, the ones that do carry information almost surely correspond to a single ionisation event. In these conditions, simultaneous detection of two electrons can with a high degree of certainty be ascribed to Auger decay, rather than two uncorrelated single ionisation events in two different atoms or a double photoionisation of one atom. The resulting coincidence map is shown in Fig. 5.7.

Performing a cosine fit on the time-dependent signal of the sidebands in the photoelectron spectrum, we infer the associated energy-dependent ionisation time-delays. We reference these delays to the one of the $2p$ shell in neon, known to exhibit an atomic delay close to zero in the energy range of interest[128]. This allows us not only to give an absolute value to the measured time delay, but also to cancel out the attochirp. The extracted photoionisation time delay difference $\tau_{\mathrm{Xe}(4d)} - \tau_{\mathrm{Ne}(2p)}$ thus reflects the absolute time delays in Xe. As shown in Fig. 5.8 (a) and (b), for photon energies above 80 eV, the absolute time delays for the two Auger electrons, $\tau[4d_{5/2}]$ and $\tau[4d_{3/2}]$,

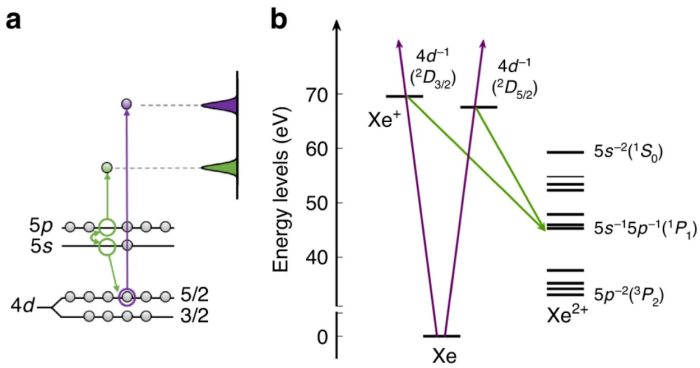

Figure 5.6: Xe 4d ionisation scheme. a) Direct photoionisation (violet) and Auger decay processes (green) initiated by absorption of harmonic radiation; b) Xe energy diagram detailing the direct and Auger ionisation paths (violet and green, respectively). Taken from Article V.

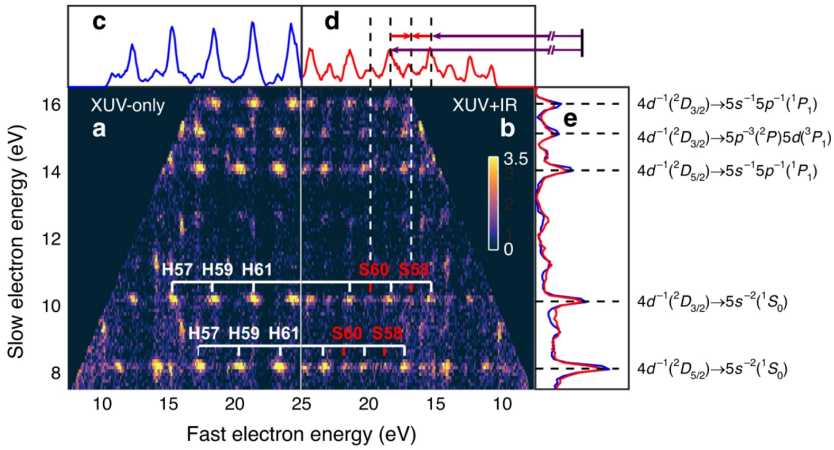

Figure 5.7: Two-electron coincidence map. Coincidence map for a) XUV only, b) XUV+IR. Projections on the fast electron energy axis for c) XUV only and d) XUV+IR. The applied RABBIT scheme is indicated by violet (XUV) and red (IR) arrows. Projections on the slow electron energy axis (e) for XUV-only (blue) and XUV+IR (red), showing peaks originating from different Auger channels. Taken from Article V.

are approximately constant and equal. Close to the ionisation threshold, however, there is a noticeable variation of both $\tau[4d_{5/2}]$ and $\tau[4d_{3/2}]$. To understand the origin of these modulations, we use a variant of the random phase approximation with exchange method accounting for relativistic effects[139]. We are able to link the delay deviation observed at low energies to a spin-flip, an effect forbidden for pure dipole transitions, where the electron spin is affected by the magnetic field induced by the ultrafast orbital motion. The spin-flip is in our case present in the $4d_{5/2} \rightarrow \varepsilon f_{5/2}$ ionisation channel, which has a rather strong contribution close to the ionisation threshold. At higher photon energies, photoionisation is dominated by $4d_{3/2} \rightarrow \varepsilon f_{5/2}$ and $4d_{5/2} \rightarrow \varepsilon f_{7/2}$ channels. We conclude that the delay modulations for photon energies below 80 eV originate from the interference of the this spin-orbit-induced transition with the pure dipole transitions involving the giant resonance.

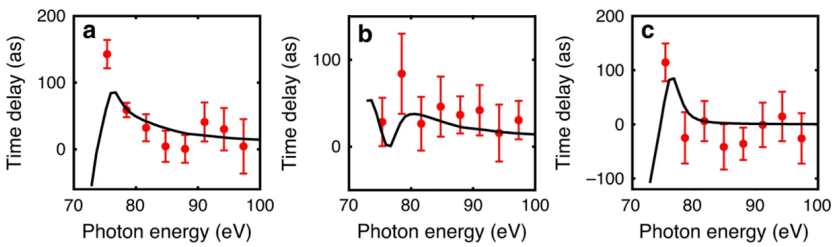

Figure 5.8: Photoemission time delays in Xe. Time-delay differences: a) $\tau_A[\text{Xe}(4d_{3/2})] - \tau_A[\text{Ne}(2p)]$, b) $\tau_A[\text{Xe}(4d_{5/2})] - \tau_A[\text{Ne}(2p)]$, c) $\tau_A[\text{Xe}(4d_{3/2})] - \tau_A[\text{Xe}(4d_{5/2})]$. Red: experimental data, black: calculations. Adapted from Article V.

5.3.3 3s and 3p Cooper minima in argon

One very interesting feature in the photoionisation of argon is the appearance of Cooper minima (CM)[140] in the cross-sections for ionisation from the $3s$ and $3p$ shells. Namely, the matrix element for the $3p \rightarrow \varepsilon d$ transition changes sign for a photon energy of approximately 53 eV, causing the cancellation of the corresponding ionisation cross-section. Inter-channel coupling leads to a "replica" of the CM in the $3s$ shell, cancelling the $3s \rightarrow \varepsilon p$ cross-section at a photon energy of 42 eV.

The atomic delays around CMa, known to also exist in other atoms[141], are experimentally very elusive for a rather clear reason - the number of photoelectrons tends to zero as one approaches the energy of interest. Previous studies[7,125] have therefore been limited to the energy region spanning from 30 to 40 eV, approaching, but not reaching the $3s$ CM. In Article VI, we extend this region to cover both CMa in Ar, measuring the photoemission time delay difference between electrons from the $3s$ and $3p$ channel using photon energies from 35 to 70 eV.

Apart from the $3s/3p$ photoionisation cross-section approaching zero, time-delay extraction around CMa is further complicated by two circumstances:

a) The ionisation potentials for the $3s$ and $3p$ channels differ by $I_{p,3s} - I_{p,3p} = (29.4 - 15.76)\,\text{eV} = 13.48\,\text{eV} = 9\,\hbar\omega - 0.47$ eV for $\hbar\omega = 1.55$ eV, corresponding to a central laser wavelength of $\lambda = 800$ nm, as in our experiment. This means that the peaks in the photoelectron spectrum originating from single-photon ionisation from the $3p$ channel partially overlap the sideband peaks from the $3s$ channel and vice versa. Given that the photoionisation cross-section of the $3p$ channel is significantly higher than that of the $3s$, it is the extraction of the $3s$ delay that is more severely hindered, especially in the respective CM region.

b) Several shake-up channels cause significant $3s$ signal contamination; these are most notably the $3s^2 3p^4(^1D)3d(^2S)$ (also referred to as $3p^{-2}3d$ or just $3d$ in Article VI) channel with $I_{p,3d} = 38.6$ eV and the $3s^2 3p^4(^1D)4p(^2P)$ (alternatively $3p^{-2}4p$ or $4p$) channel, opening at $I_{p,4p} = 37.1$ eV. As shown in Fig. 5.9 (a), the two dominate over $3s$ in the CM region, around 14 eV photoelectron energy.

The above obstacles are somewhat mitigated by the use of a two-metre-long MBES, which offers a spectral resolution of $E/\Delta E \geq 80$ (see Sect. 4.3.2). For measurements involving higher-energy photons, retarding potential was applied to shift the sidebands of interest to lower kinetic energies and thereby increase the resolution.

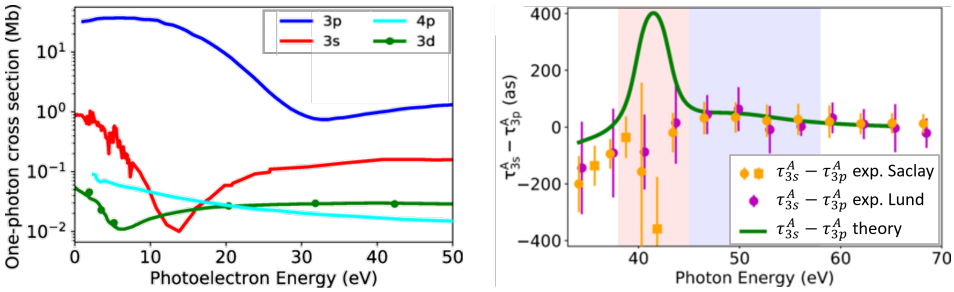

Figure 5.9: Photoionisation of Ar around the 3s and 3p Cooper minima. a) One-photon cross-section for different ionisation channels. The 4p and 3d shake-up channels dominate over 3s around the CM (~ 14 eV photoelectron energy). b) Atomic photoionisation time-delay difference between electrons from the 3s and 3p shells. Shaded areas represent the CM energy regions in the 3s (red) and 3p (blue) channel. Scattered points show experimental data from Lund (violet) and Saclay (yellow), the green curve shows the theoretical calculation. Adapted from Article VI.

Fig. 5.9 (b) displays the atomic time delay difference $\tau^A_{3s} - \tau^A_{3p}$, independently measured by our team in Lund and the team from CEA Saclay in France, along with the theoretical calculations based on two-photon two-colour random phase approximation with exchange[142] performed by the group of Eva Lindroth from Stockholm University. Away from the $3s$ CM, the experimental data from both groups agree well with the theoretical predictions. A slightly improved agreement (not shown in Fig. 5.9) is reached by including the effect of the $4p$ shake-up channel in the region below 40 eV. Around the $3s$ CM, the data from the two experimental groups agree well with each other, however there is a noticeable disagreement with the theory. This discrepancy might originate from an intricate interplay between the dephased $3s$ and shake-up channels, which add up incoherently in our angle-integrated measurement.

5.3.4 Rydberg states in helium

Article VIII describes a study of resonant two-photon ionisation of helium via the $1snp\,^1\mathrm{P}_1$, $n \in \{3, 4, 5\}$ intermediate states (in further text: $3p, 4p,$ and $5p$ resonance). We use RABBIT to inspect the phase of the Rydberg states, approaching the task in two different ways: *(i)* VMIS-based angle-resolved measurement with moderate spectral resolution and *(ii)* MBES-based angle-integrated measurement with high spectral resolution. With the help of calculations based on many-body perturbation theory, we investigate the nature of the observed phase variations across the energy range containing the resonances of interest.

As it can be seen in Fig. 5.10, we tune the 15^{th} harmonic of the fundamental IR field to excite the different resonances. With the tunability and spectral bandwidth that we have, we can choose between populating $3p$ only, coherently $3p$ and $4p$, $4p$ only or coherently $4p$ and $5p$. With a weak probe laser pulse we promote the excited-state

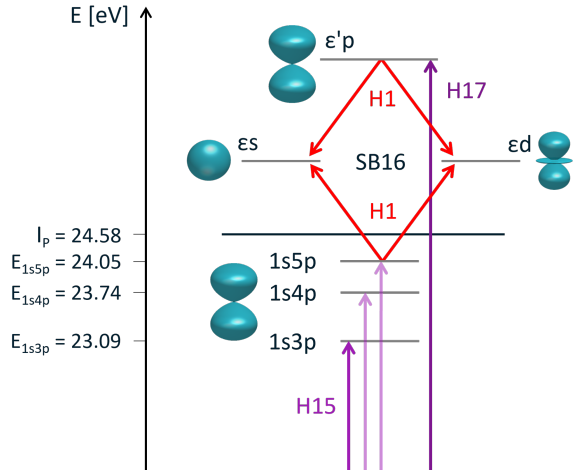

Figure 5.10: Experimental scheme. H15 is tuned into resonance with the $1snp$, n=3-5 Rydberg states of He, whilst H17 ionises the atom. A weak H1 (fundamental) signal is combined with the harmonics, creating SB16 through s and d angular momentum channels.

electrons into the εs and εd continuum states. At the same time, we use harmonic 17 to directly ionise helium from the ground state into the $\varepsilon' p$ continuum. In combination with the probe, it creates another quantum path to εs and εd, resulting in a sideband in the photoelectron spectrum with an intensity dependent on the XUV-IR delay. In the first experimental configuration, we use a VMIS, presented in Sect. 4.3.2, to record the angle-resolved photoelectron spectrum (PES) as a function of the delay.

In Fig. 5.11 one can see the VMIS images taken while tuning H15 to different Rydberg states. A significant signal enhancement is observed as H15 is tuned into resonance with each state. Note that this zoom, easily achieved by tuning the voltages on the VMIS electrodes, is for illustration purposes only. For proper image inversion all harmonics appearing in the angle-resolved PES must be recorded. Given that in this

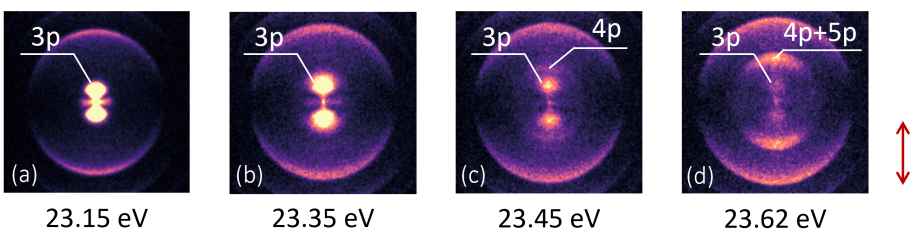

Figure 5.11: VMIS images of SB16 upon tuning H15 across Rydberg states in He. Energy of H15 is indicated below each image. (a) and (b) only 3p resonance visible; (c) 3p and 4p resonances; (d) mostly 4p and 5p resonance populated. Central part of non-inverted VMIS images only. The red arrow indicates the polarisation direction.

experiment we were interested in very low kinetic energy electrons (< 0.8 eV), we needed the largest zoom possible. We therefore used Xe or Kr for HHG, which resulted with only three or four harmonic peaks in the PES. An example of appropriate zoom can be seen in Fig. 4.8, where the PES was obtained using harmonics generated in Ar.

The angle-and-energy-resolved phase of SB16 around the $4p$ resonance recorded with the VMIS is displayed in Fig. 5.12. The experimental values are compared to a calculation based on the variant of the random phase approximation with exchange (RPAE) method where correlations induced by both photons involved in the observed transition are taken into account [142]. The data with a satisfactory signal-to-noise ratio are well reproduced by the theory. A phase jump of $-\pi$ rad can be seen in the experimental data for angles up to 60° at the resonant energy (25.35 eV). At energies below the resonance, a phase jump of similar magnitude can be observed towards higher angles, as expected from Fano's propensity rule for transitions involving an s and a d channel in the final state [143].

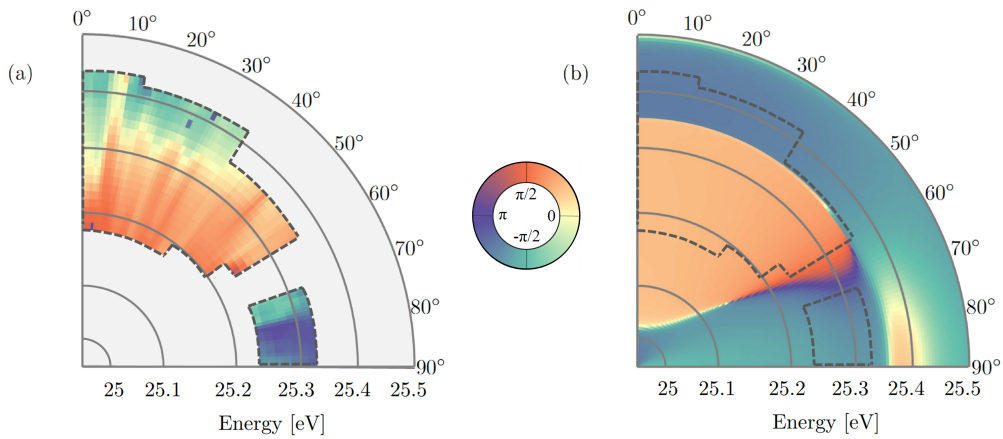

Figure 5.12: Angle-and-energy-resolved phase around the 4p resonance. A phase jump in energy of approximately $-\pi$ rad is observed at resonance, and in angle around 65°. (a) VMIS data, areas with low signal-to-noise ratio filtered out. (b) theoretical calculation. The colour scale is common for the two panels.

Fig. 5.13 shows the amplitude and phase of 2ω oscillations of SB16 obtained from the angle-integrated signal measured with the VMIS. Resonant amplitude enhancements are accompanied by drops in the phase value by about $-\pi$ rad. This can be understood by considering the two-photon transition matrix element given in Eq. 4.1 in the case of a resonant intermediate state in the absorption path. At resonance energies, $M^{(+)}_{g\to f}$ diverges since $E_g + \hbar\Omega = E_i$. This causes sudden phase jumps of $-\pi$ rad, described by the theoretical calculations.

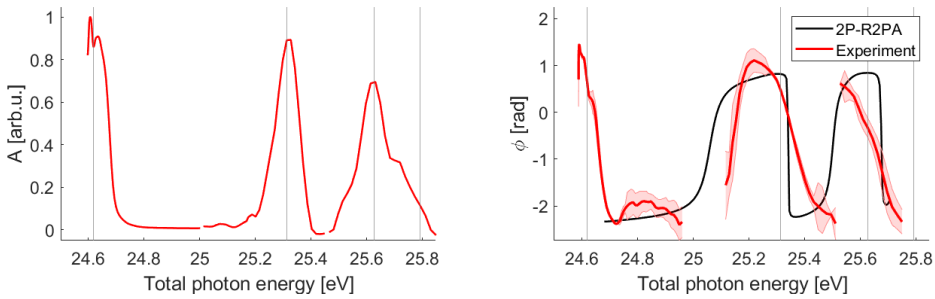

Figure 5.13: Angle-integrated 2ω-amplitude and phase of SB16. Left: resonant amplitude enhancement can be seen in the experimentally obtained peaks (peak values not to scale). Right: the measured (red) and calculated (black) phase feature jumps of $-\pi$ rad across resonances and $+\pi$ rad in between. Phase of SB16 is referenced to that of the non-resonant SB18. Grey lines indicate the energies of $1snp$, n=3-6 resonances as provided by the NIST database [144], with the addition of the energy corresponding to the frequency of the probe.

The phase jumps of $+\pi$ rad, seen in between each two resonances, are a consequence of the fact that $M^{(+)}_{g\to f} \xrightarrow{E_g+\hbar\Omega-E_i\to 0^+} +\infty$ and $M^{(+)}_{g\to f} \xrightarrow{E_g+\hbar\Omega-E_i\to 0^-} -\infty$, meaning that the transition amplitude crosses zero between two resonances, accompanied with a sign change opposite to the one at resonance. RPAE calculations suggest that this phase jump should be smoother than the resonant one. This can be explained by looking at Fig. 5.14, which shows the calculated relative strength of the s and the d channel, as well as their respective phases. Although channel-wise phase jumps are sharp, it is their relative position and strength that determine the character of the total phase variation. Between the $3p$ and $4p$ resonance, up to around 25 eV, the s channel dominates over d. Thereafter, the d channel, in this region out of phase with s, takes over and the total phase gradually rises. A nearly-constant-phase plateau fol-

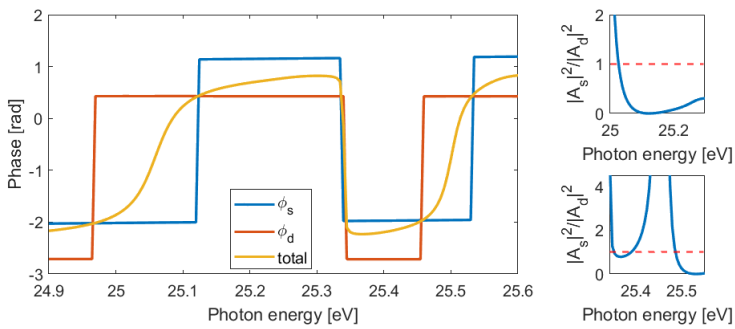

Figure 5.14: Calculated angle-integrated s and d channel phase and relative strength. The position and slope of the total phase variations are determined by the phases and relative strength of the s and the d channel. The red dashed line in the panels on the right indicates equal s and d channel amplitudes.

lows, where the s and d channel are approximately in phase. At resonance (25.35 eV), the two channels feature a phase jump almost exactly at the same energy, leading to a sudden total phase jump of $-\pi$ rad. Finally, between the $4p$ and $5p$ resonance, at energies above 25.5 eV, a behaviour analogous to the one between $3p$ and $4p$ is observed.

Looking again at Fig. 5.13, one can see that the slopes of the phase jumps, in particular at resonances, are not well reproduced by the calculations. To overcome the possibly insufficient spectral resolution of the VMIS, we use an MBES to measure the phase of SB16 while tuning H15 around the $4p$ resonance. As illustrated in Fig. 5.15, this measurement shows different phase variations at resonance (with a linear slope) and in between resonances (non-linear). This observation is in accordance with recent works by Autuori[145] and Drescher[146].

To better understand the phase variation at resonance, we improve our model by including higher-order terms of perturbation theory for the dressing IR field. We do so by adding a correction to the denominator in the two-photon transition matrix element, substituting the Rydberg state energy, E_i, with $E_i+\delta_i+i\gamma_i$. This correction allows us to take into account the AC Stark shift (δ_i) and the broadening induced by the dressing field (γ_i). This results in an additional phase shift:

$$\chi_i = \mathrm{arctg}\,\frac{\gamma_i}{E_g + \hbar\Omega - (E_i + \delta_i + i\gamma_i)}, \tag{5.19}$$

causing the phase to vary as $\mathrm{arctg}(\gamma_i/x)$ close to resonance (x denoting the energy difference in the denominator, which goes to zero at resonance). The ionisation-induced broadening γ_i thus has a direct impact on the phase slope, which varies as $-1/\gamma_i$ around the resonance. In Fig. 5.15 we demonstrate this effect by comparing the cal-

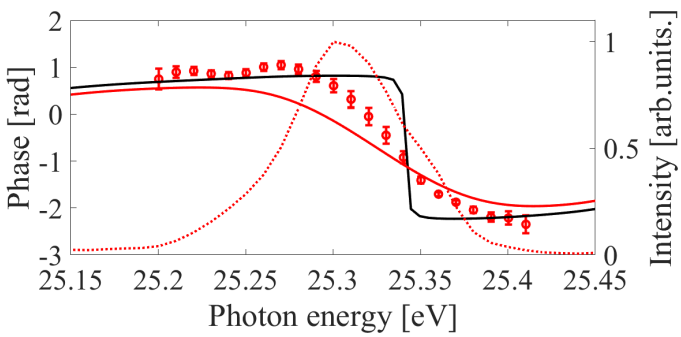

Figure 5.15: Power broadening of the 4p state. Red data points: SB16 phase measured by the MBES, referenced to non-resonant SB18. Red dashed curve: experimental 2ω amplitude. Solid curves: calculated phase of SB16 with $\gamma_i = 10$ meV (red) and without (black) power-induced broadening.

culations with and without the γ_i correction. It can be seen that a (slightly overestimated) broadening of 10 meV has a measurable impact on the phase slope around the resonance.

Our work illustrates the amount of detail involved in a photoionisation process that can be accessed using different state-of-the-art tools. In addition, it demonstrates the exchange between experiment and theory, necessary to gain understanding of the various features of resonant photoionisation.

Chapter 6

Summary and outlook

This thesis deals with several subjects that fall within the scope of ultrafast science, illustrating its multifaceted character. Generally speaking, technological developments and scientific ideas propel each other forward; different articles from this thesis tend to find their place on one of the two sides of this interplay.

As novel light sources emerge, it becomes necessary to develop techniques to characterise, and ultimately control and optimise, the pulses they deliver. To be interesting from a practical point of view, such a technique should fulfill multiple requirements. It needs to be compact and easy to implement, while at the same time providing fast and reliable results. In articles I-III we address each of these criteria, proposing improvements to the d-scan as a well-established, mature pulse characterisation method. Article I thus proposes a rapid and robust pulse reconstruction algorithm directly applicable to an existing piece of d-scan hardware. Article II presents an innovative single-shot d-scan set-up, minimising the number of required optical components and consequently the needed space. In Article III, we extend the model which is at the base of the d-scan pulse retrieval to enable the determination of the full electric field waveform of pulses with octave-spanning spectra.

The interest of the community in the d-scan has not waned since the beginning of my PhD[90,147]. On the contrary, there have been new users worldwide, while diverse improvements have taken place in groups more experienced with the technique. As new sources of coherent light emerge, d-scan will likely be further adapted. Recent advances include extension into the mid-IR[148] and deep UV[87] spectral regions. The exploration of different non-linear phenomena for d-scan also continues, as for example signaled by the work involving self-diffraction d-scan[88]. Further activities will certainly be directed towards eliminating the constraints on the pulse measurement,

like in the proposed self-calibrating d-scan[149], as well as introducing innovative approaches to pulse retrieval, such as a recent one based on neural networks[150]. Finally, d-scan is likely to become increasingly popular among users needing a means of direct feedback in their pulse optimisation procedure. Its benefit for this purpose has lately been demonstrated in a piece of work addressing the elimination of pulse train instabilities[151], but also experienced by members of our group while working on Articles I-III and VII.

Another study in my thesis has been dedicated to pulse characterisation, however on another level. The work summarised in Article VII concerns a novel way of combining several pre-existing techniques with a numerical algorithm to create a tool capable of 4D characterisation of laser pulses undergoing filamentation. The result of the diagnostic method we propose is the possibility to determine the spatially resolved electric field at any chosen point inside a femtosecond filament. This has multiple implications, calling both for direct applications as for further developments. Namely, filamentation has so far been somewhat underrepresented as a spectral broadening method in applications involving high-order non-linear interactions, such as HHG. The reason for this is that the intricate filament dynamics offer little control over the output pulse parameters; at the same time, the investigation of these dynamics has so far been hindered by the inability to perform experimental studies of pulses inside the filament. Our first hope is therefore that the method we propose will kindle interest in experimental investigations of filament dynamics, finally providing the long-awaited means of direct comparison with simulations. Secondly, one could foresee that applications of pulses modified by filamentation might diversify, triggered by the possibility to identify and extract pulses with desirable characteristics from the inside of a filament. Furthermore, recent technological developments have yielded highly stable, comparatively simple, powerful and inexpensive ytterbium-doped lasers, which deliver pulses readily compressed down to the $30-40$ fs range using multi-pass cells[152]; as an alternative to a second multi-pass cell stage[153], our scheme offers the possibility to further compress these pulses down to the few-cycle regime using filamentation, while at the same time monitoring for potential spatio-temporal couplings. Thirdly, our method is in principle highly versatile and may attract the attention of groups working with different laser pulse characteristics, beam focusing geometries or filament generation media. Lastly, our own work could be further improved. For instance, a more sophisticated, two-stage differential pumping scheme could be developed to allow the use of larger pinholes for filament termination. Another very interesting idea would be to adapt our set-up to not only observe the filament core, but also the much less understood conical emission.

Moving on to the topic of photoionisation dynamics -the second major part of my thesis work-, in Articles IV-VI, and VIII we have focused on exploring the role of

electron correlations in measured photoemission time delays. We used the RABBIT technique to study different noble-gas atoms and a small molecule, each time in an energy region where interesting phenomena occur. In Article IV, we investigate the dynamics of photoionisation through a shape resonance in molecular nitrogen. We measure the time delays associated with different vibrational levels of the state involving the resonance, and discover that their difference is a consequence of the different inter-nuclear distances for the observed levels. This is in direct collision with the Franck-Condon principle, revealing one limitation of the widely used assumption that nuclei can be considered motionless upon electronic transitions. In Article V, we investigate the interplay between different ionisation mechanisms in xenon over a wide photon energy range. We apply the coincidence technique to overcome spectral congestion, caused by the presence of spin-orbit splitting, as well as multiple Auger decay channels. Supported by theoretical calculations, we are able to disentangle the different contributions to the photoelectron spectrum and elucidate the underlying interfering ionisation mechanisms. Article VI is a study of Cooper minima in argon, where we measure photoemission time delays around these challenging features, where the ionisation cross-section goes to zero. We use theoretical tools to demonstrate a large degree of signal contamination by shake-up channels, which cannot be directly probed. Finally, in Article VIII, we explore ionisation through low Rydberg states of helium. Performing separate measurements, we obtain angularly resolved phase information with a moderate spectral resolution or angle-integrated information with a high spectral resolution. This provides us a deep understanding of the interplay between the two angular channels involved in the two-photon ionisation from the ground state through the Rydberg states. At the same time, we are able to point out the effects of the pulses driving the ionisation, such as power-broadening and Stark shifting.

One thing in common for the experiments briefly summarised above is that they all require very high-standard measurement capacities, mainly the interferometric stability and spectral resolution. During my PhD (after the completion of Articles IV-VI), my colleagues have conducted a major upgrade of the Lund Attolab beamline, further improving these two important features. The MBES was tuned so as to maximise its spectral resolution, which enabled the detailed observations shown in Article VIII. Combined with the experience that our group has with the RABBIT technique, in particular coincidence spectroscopy as well as spectral filtering and chopping of the probe pulses, the high energy resolution of the MBES provides us with a tool to study spectrally challenging subjects. Future investigations may address spin-orbit-split states, autoionising states or molecular ionisation. One of the mentioned Attolab upgrades includes the possibility to increase the laser repetition rate from 1 to 3 kHz. This option, which we have so far not thoroughly exploited, will grant us a significant improvement in measurement statistics. This will be an

additional asset in experiments requiring narrowband and/or chopped probe pulses, as well as coincidence spectroscopy. A possible powerful development could be to combine angular and high spectral resolution, either in a single, novel detector or by placing an MBES and a VMIS one after the other.

Acknowledgements

"The most important asset in research are not the instruments, it is the people." Those are sincere, often repeated words of the head and founder of my group. They reflect the philosophy based on which she has shaped the atmosphere at work throughout the years (although she will feel humbled by what I am writing here and hurry to claim that it is *us* who have shaped it, not her). Thank you, Anne L'Huillier, for your ever-present tactfulness and your rock-solid support in matters scientific and personal. My gratitude is also due to Cord Arnold, who has endured the task of being my principal supervisor like a champion and whose understanding was at times more abundant than I deserved. The lessons I learned from my relationship with the two of you will stay with me for years to come.

I would like to thank Katalin Varjú for giving me the opportunity to work with ELI and introducing me to Anne. I am grateful to John Tisch for such an enjoyable initiation to attoscience, without which I certainly would not have ended up in Lund. I also hereby thank Milorad Kurajica for not asking many questions about the parachute jump I made into my Master's thesis defence.

Many thanks to the former and current members of my awesome team, Mattias Ammitzböll, David Busto, Hugo Laurell, Sizuo Luo, Saikat Nandi, Robin Weissenbilder, Shiyang Zhong, and since recently also Vénus Poulain. I have been incredibly lucky to work with such talented people like you, not only for all the things I have been able to learn from you, but also for your kindness and support. Special thanks to you, Robin, for accomplishing your Malmö mission, for your dedication to the gallery and for being the perfect flatmate. David, mi hermano de pelota, te agradezco enormemente por todo tu ayuda durante estos años.

Thank you, Eva Lindroth, for all your kind help and patience. Thank you, Per, for your witty understatements and clever use of subtext. One has a lot to learn from you and it is always a pleasure to have you around. Merci, Mathieu Gisselbrecht, de ne plus jamais me laisser te parler en anglais à partir du moment ou tu as entendu mon premier mot de français.

I also need to express my gratitude to Miguel Miranda, Chen Guo, and Richard Squibb for sharing their wizardry with us Muggles, as well as Balázs Major for his help taming my filament. Thank you, Christoph Jusko, for pushing in the same direction as I until the end of the filamentation project and becoming a friend on our way there.

My years at Fysicum have been wonderful outside the lab, too! The fun was never-ending with my 11 Hz crew, who have adopted me so early on. Filippo Campi and Jan Lahl would often make my day with their sharp wit. Piotr Rudawski, your support

was exceptionally important to me during my Master's. Thank you for your patience and all the lovely moments my family got to spend with yours. Fabian Brunner, I enjoyed so much being around such a gracious and smart person like yourself. I hope we will meet up more often now that we live closer to each other. Jasper Peschel, you have been part of my life in so many ways in the past few years and some of our conversations still sometimes provoke my thought. Thank you for always being so inspiringly present, whether you're building a pillow tent, discussing political or ethical issues, or distributing yet another round of cocktails. Hampus Wikmark Kreuger, the fun with you is so much beyond the (abundant!) ha-has. Thank you for extending the palette of flavours I experienced in Sweden by 98.5% and never declining a discussion about the use of subjunctives (they *are*, after all, the most important thing in the world - if we don't count mustard seeds, of course). Sylvain Maclot, I have decided that you need to deserve your acknowledgement (see below).

Apart from those already mentioned, I would like to thank the rest of you who have contributed to the atmosphere of inclusion, acceptance and constructive and joyful exchange that our group is so widely famous for: Elisa Appi, Samuel Bengtsson, Hugo Dacasa Pereira, Ron Demjaha, Dominik Hoff, Maria Hoflund, Johan Mauritsson, Sara Mikaelsson, Alexander Permogorov, Marius Plach, Ann-Kathrin Raab, Daniel Díaz Rivas, Emma Simpson, Ivan Sytcevich (huge spasibo for the help with the pre-print), and Anne-Lise Viotti (quelle bombe L'Opaline, merci !), as well as former group members Hélène Coudert-Alteirac, Anne Harth, Christoph Heyl, Neven Ibraković, Marcus Isinger, Fabian Langer, Maïté Louisy, Anna Olofsson, Jan Vogelsang, and Esben Witting Larsen.

I have also had the pleasure to get to know some delightful people outside my immediate group. Jan Marcus Dahltröm, I had so much fun every time we would discuss physics. In hindsight, I should have bugged you way more. Thanks to Mattias Bertolino and Stefan Carström for the cool chats. Special thanks go to Xiaocui Wang for the lovely moments we spent together. Last but not least, I thank Claes-Göran Wahlström for offering a firm yet fair leading hand to Fysicum for the most part of my PhD, as well as Anne Petersson-Jungbeck and Åke Johansson for all their much-needed help.

Hvala, Šibi, što si me poslao u London, a tebi, Svetislave, što si me istresao iz gaća kad god je zatrebalo.

Vuče i Anatole, ruku na srce, pre bi se moglo reći da ova teza potoji uprkos, nego zahvaljujući vama. Zahvalnost vam stoga više sleduje za to što ste je postavili u jedan sasvim nov kontekst, učinivši želju za istraživanjem sporednom stavkom u mom životu. Neizmerno se radujem svim zajedničkim trenucima koji nam predstoje, tokom kojih ću, nadam se, uspeti da vam prenesem ljubav za traženjem odgovora na vaša

“Mama, kako..?” i “A zbog čega..?”

Silvan, gde da počnem? Tvoja ljubav i podrška su u korenu izmenile moj život, uključujući i mnoge aspekte ovog doktorata. Ni za šta na svetu ne bih menjala nijednu od mnogih, tako važnih odluka koje smo zajedno doneli, iako nam je retko koja u datom trenutku pojednostavila situaciju. Neizmerno sam zahvalna za sve tvoje strpljenje i razumevanje i nadam se da ću tokom narednih decenija uspeti da ti uzvratim makar jedan njihov deo.

Finalement, merci Mamika et Grand-Père, d’avoir tenu la baraque !

References

[1] A. H. Zewail. Laser femtochemistry. *Science*, 242(4886):1645–1653, 1988.

[2] A. McPherson, G. Gibson, H. Jara, U. Johann, T.S. Luk, I.A. McIntyre, K. Boyer, and C.K. Rhodes. Studies of multiphoton production of vacuum-ultraviolet radiation in the rare gases. *J. Opt. Soc. Am. B*, 4(4):595–601, 1987.

[3] M. Ferray, A. L'Huillier, X.F. Li, L.A. Lompre, G. Mainfray, and C. Manus. Multiple-harmonic conversion of 1064 nm radiation in rare gases. *J. Phys. B*, 21 (3):L31–L35, 1988.

[4] P. M. Paul, E. S. Toma, P. Breger, G. Mullot, F. Augé, Ph. Balcou, H. G. Muller, and P. Agostini. Observation of a train of attosecond pulses from high harmonic generation. *Science*, 292(5522):1689–1692, 2001.

[5] F. Calegari, G. Sansone, S. Stagira, C. Vozzi, and M. Nisoli. Advances in attosecond science. *Journal of Physics B: Atomic, Molecular and Optical Physics*, 49: 062001, 03 2016.

[6] H.G. Muller. Reconstruction of attosecond harmonic beating by interference of two-photon transitions. *Applied Physics B*, 74:s17–s21, 06 2002.

[7] K. Klünder, J. M. Dahlström, M. Gisselbrecht, T. Fordell, M. Swoboda, D. Guénot, P. Johnsson, J. Caillat, J. Mauritsson, A. Maquet, R. Taïeb, and A. L'Huillier. Probing single-photon ionization on the attosecond time scale. *Phys. Rev. Lett.*, 106:143002, 2011.

[8] E. P. Månsson, D. Guénot, C. L. Arnold, D. Kroon, S. Kasper, J. M. Dahlström, E. Lindroth, A. S. Kheifets, A. L'Huillier, S. R. Sörensen, and M. Gisselbrecht. Double ionization probed on the attosecond timescale. *Nature Physics*, 10:207–211, 2014.

[9] M. Kotur, D. Guénot, A. Jimenez-Galan, D. Kroon, E. W. Larsen, M. Louisy, S. Bengtsson, M. Miranda, J. Mauritsson, C. L. Arnold, S. E. Canton, M. Gisselbrecht, T. Carette, J. M. Dahlström, E. Lindroth, A. Maquet, L. Argenti,

F. Martín, and A. L'Huillier. Spectral phase measurement of a fano resonance using tunable attosecond pulses. *Nature Communications*, 7, 2016.

[10] S. Heuser, Á. Jiménez Galán, C. Cirelli, C. Marante, M. Sabbar, R. Boge, M. Lucchini, L. Gallmann, I. Ivanov, A. S. Kheifets, J. M. Dahlström, E. Lindroth, L. Argenti, F. Martín, and U. Keller. Angular dependence of photoemission time delay in helium. *Phys. Rev. A*, 94:063409, 2016.

[11] V. Gruson, L. Barreau, Á. Jiménez-Galan, F. Risoud, J. Caillat, A. Maquet, B. Carré, F. Lepetit, J.-F. Hergott, T. Ruchon, L. Argenti, R. Taïeb, F. Martín, and P. Salières. Attosecond dynamics through a fano resonance: Monitoring the birth of a photoelectron. *Science*, 354(6313):734–738, 2016.

[12] I. Jordan, M. Huppert, S. Pabst, A. S. Kheifets, D. Baykusheva, and H. J. Wörner. Spin-orbit delays in photoemission. *Phys. Rev. A*, 95:013404, 2017.

[13] S. Haessler, B. Fabre, J. Higuet, J. Caillat, T. Ruchon, P. Breger, B. Carré, E. Constant, A. Maquet, E. Mével, P. Salières, R. Taïeb, and Y. Mairesse. Phase-resolved attosecond near-threshold photoionization of molecular nitrogen. *Physical Review A (Atomic, Molecular, and Optical Physics)*, 80:011404–, 07 2009.

[14] M. Huppert, I. Jordan, D. Baykusheva, A. von Conta, and H. J. Wörner. Attosecond delays in molecular photoionization. *Phys. Rev. Lett.*, 117:093001, 2016.

[15] S. Beaulieu, A. Comby, A. Clergerie, J. Caillat, D. Descamps, N. Dudovich, B. Fabre, R. Géneaux, F. Légaré, S. Petit, B. Pons, G. Porat, T. Ruchon, R. Taïeb, V. Blanchet, and Y. Mairesse. Attosecond-resolved photoionization of chiral molecules. *Science*, 358(6368):1288–1294, 2017.

[16] L. Cattaneo, J. Vos, R. Bello, A. Palacios, S. Heuser, L. Pedrelli, M. Lucchini, C. Cirelli, F. Martín, and U. Keller. Attosecond coupled electron and nuclear dynamics in dissociative ionization of h2. *Nature Physics*, 14, 2018.

[17] R. Locher, L. Castiglioni, M. Lucchini, M. Greif, L. Gallmann, J. Osterwalder, M. Hengsberger, and U. Keller. Energy-dependent photoemission delays from noble metal surfaces by attosecond interferometry. *Optica*, 2(5):405–410, 2015.

[18] L. Kasmi, M. Lucchini, L. Castiglioni, P. Kliuiev, J. Osterwalder, M. Hengsberger, L. Gallmann, P. Krüger, and U. Keller. Effective mass effect in attosecond electron transport. *Optica*, 4(12):1492–1497, 2017.

[19] I. A. Walmsley and C. Dorrer. Characterization of ultrashort electromagnetic pulses. *Adv. Opt. Photon.*, 1(2):308–437, 2009.

[20] S. Ghimire, A.D. DiChiara, E. Sistrunk, P. Agostini, L.F. DiMauro, and D.A. Reis. Observation of high-order harmonic generation in a bulk crystal. *Nat. Phys.*, 7:138–141, 2014.

[21] T.T. Luu, Z. Yin, A. Jain, T. Gaumnitz, Y. Pertot, J. Ma, and H.J. Wörner. Extreme–ultraviolet high–harmonic generation in liquids. *Nat. Commun.*, 9 (3723), 2018.

[22] K.C. Kulander, K.J. Schafer, and J.L. Krause. Dynamics of short-pulse excitation, ionization and harmonic conversion. In *Super-intense laser-atom physics*, pages 95–110. Springer, 1993.

[23] P. B. Corkum. Plasma perspective on strong field multiphoton ionization. *Phys. Rev. Lett.*, 71:1994–1997, 1993.

[24] M. Lewenstein, Ph. Balcou, M.Yu. Ivanov, A L'Huillier, and P.B. Corkum. Theory of high-harmonic generation by low-frequency laser fields. *Phys. Rev. A*, 49:2117–2132, 1994.

[25] O. Kfir, P. Grychtol, E. Turgut, R. Knut, D. Zusin, D. Popmintchev, T. Popmintchev, H. Nembach, J. Shaw, A. Fleischer, H. Kapteyn, M. Murnane, and O. Cohen. Generation of bright phase-matched circularly- polarized extreme ultraviolet high harmonics. *Nature Photonics*, 9, 12 2014.

[26] Z.-Y. Chen and A. Pukhov. Bright high-order harmonic generation with controllable polarization from a relativistic plasma mirror. *Nature Communications*, 7, 2016.

[27] G. Ma, W. Yu, M.Y. Yu, B. Shen, and L. Veisz. Intense circularly polarized attosecond pulse generation from relativistic laser plasmas using few-cycle laser pulses. *Opt. Express*, 24(9):10057–10065, 2016.

[28] J.L. Krause, K.J. Schafer, and K.C. Kulander. High-order harmonic generation from atoms and ions in the high intensity regime. *Phys. Rev. Lett.*, 68:3535–3538, 1992.

[29] C.M. Heyl, C.L. Arnold, A. Couairon, and A. L'Huillier. Introduction to macroscopic power scaling principles for high-order harmonic generation. *J. Phys. B*, 50, 2016.

[30] H. Wikmark, C. Guo, J. Vogelsang, P. W. Smorenburg, H. Coudert-Alteirac, J. Lahl, J. Peschel, P. Rudawski, H. Dacasa, S. Carlström, S. Maclot, M. B. Gaarde, P. Johnsson, C. L. Arnold, and A. L'Huillier. Spatiotemporal coupling of attosecond pulses. *Proceedings of the National Academy of Sciences*, 116(11): 4779–4787, 2019.

[31] M. D. Perry and J. K. Crane. High-order harmonic emission from mixed fields. *Phys. Rev. A*, 48:R4051–R4054, 1993.

[32] J. Mauritsson, P. Johnsson, E. Gustafsson, A. L'Huillier, K. J. Schafer, and M. B. Gaarde. Attosecond pulse trains generated using two color laser fields. *Phys. Rev. Lett.*, 97:013001, 2006.

[33] W. Hong, P. Lu, P. Lan, Q. Zhang, and X. Wang. Few-cycle attosecond pulses with stabilized-carrier-envelope phase in the presence of a strong terahertz field. *Opt. Express*, 17(7):5139–5146, 2009.

[34] S. Odžak and D. B. Milošević. High-order harmonic generation in the presence of a static electric field. *Phys. Rev. A*, 72:033407, 2005.

[35] E. Frumker, C. T. Hebeisen, N. Kajumba, J. B. Bertrand, H. J. Wörner, M. Spanner, D. M. Villeneuve, A. Naumov, and P. B. Corkum. Oriented rotational wave-packet dynamics studies via high harmonic generation. *Phys. Rev. Lett.*, 109:113901, 2012.

[36] T. T. Luu and H. J. Wörner. Observing broken inversion symmetry in solids using two-color high-order harmonic spectroscopy. *Phys. Rev. A*, 98:041802, 2018.

[37] R.W. Boyd. *Nonlinear Optics*. Academic Press, 1992.

[38] P. B. Corkum, N. H. Burnett, and M. Y. Ivanov. Subfemtosecond pulses. *Opt. Lett.*, 19(22):1870–1872, 1994.

[39] G. Sansone, E. Benedetti, F. Calegari, C. Vozzi, L. Avaldi, R. Flammini, L. Poletto, P. Villoresi, C. Altucci, R. Velotta, S. Stagira, S. De Silvestri, and M. Nisoli. Isolated single-cycle attosecond pulses. *Science*, 314(5798):443–446, 2006.

[40] T. Pfeifer, A. Jullien, M.J. Abel, P.M. Nagel, L. Gallmann, D.M. Neumark, and S.R. Leone. Generating coherent broadband continuum soft-x-ray radiation by attosecond ionization gating. *Opt. Express*, 15(25):17120–17128, 2007.

[41] H. Vincenti and F. Quéré. Attosecond lighthouses: How to use spatiotemporally coupled light fields to generate isolated attosecond pulses. *Phys. Rev. Lett.*, 108:113904, 2012.

[42] A. Baltuska, T. Udem, M. Uiberacker, M. Hentschel, E. Goulielmakis, C. Gohle, R. Holzwarth, V. Yakovlev, A. Scrinzi, T. Haensch, and F. Krausz. Attosecond control of electronic processes by intense light fields. *Nature*, 421: 611–5, 03 2003.

[43] C. Guo, A. Harth, S. Carlström, Y.-C. Cheng, S. Mikaelsson, E. Marsell, C. Heyl, M. Miranda, M. Gisselbrecht, M. B. Gaarde, K. J. Schafer, A. Mikkelsen, J. Mauritsson, C. L. Arnold, and A. L'Huillier. Phase control of attosecond pulses in a train. *Journal of Physics B: Atomic, Molecular and Optical Physics*, 51(3):034006, 2018.

[44] K. Varjú, Y. Mairesse, B. Carré, M. B. Gaarde, P. Johnsson, S. Kazamias, R. López-Martens, J. Mauritsson, K. J. Schafer, PH. Balcou, A. L'huillier, and P. Salières. Frequency chirp of harmonic and attosecond pulses. *Journal of Modern Optics*, 52(2-3):379–394, 2005.

[45] D. Strickland and G. Mourou. Compression of amplified chirped optical pulses. *Opt. Commun.*, 56(3):219–221, 1985.

[46] O. Martinez. 3000 times grating compressor with positive group velocity dispersion: Application to fiber compensation in 1.3-1.6 μm region. *IEEE Journal of Quantum Electronics*, 23(1):59–64, 1987.

[47] A. Couairon and A. Mysyrowicz. Femtosecond filamentation in transparent media. *Physics Reports*, 441(2):47–189, 2007.

[48] G. Fibich and A. L. Gaeta. Critical power for self-focusing in bulk media and in hollow waveguides. *Opt. Lett.*, 25(5):335–337, 2000.

[49] R. Szipöcs, K. Ferencz, C. Spielmann, and F. Krausz. Chirped multilayer coatings for broadband dispersion control in femtosecond lasers. *Opt. Lett.*, 19(3): 201–203, 1994.

[50] Yu. E. Geints, A. M. Kabanov, A. A. Zemlyanov, E. E. Bykova, O. A. Bukin, and S. S. Golik. Kerr-driven nonlinear refractive index of air at 800 and 400 nm measured through femtosecond laser pulse filamentation. *Applied Physics Letters*, 99(18):181114, 2011.

[51] S Couris, M Renard, O Faucher, B Lavorel, R Chaux, E Koudoumas, and X Michaut. An experimental investigation of the nonlinear refractive index (n2) of carbon disulfide and toluene by spectral shearing interferometry and z-scan techniques. *Chemical Physics Letters*, 369(3):318–324, 2003.

[52] M. Nisoli, S. De Silvestri, O. Svelto, R. Szipöcs, K. Ferencz, Ch. Spielmann, S. Sartania, and F. Krausz. Compression of high-energy laser pulses below 5 fs. *Opt. Lett.*, 22(8):522–524, 1997.

[53] F. Belli, A. Abdolvand, W. Chang, J. C. Travers, and P. St.J. Russell. Vacuum-ultraviolet to infrared supercontinuum in hydrogen-filled photonic crystal fiber. *Optica*, 2(4):292–300, 2015.

[54] J.C. Travers, W. Chang, J. Nold, N. Y. Joly, and P.St.J. Russell. Ultrafast nonlinear optics in gas-filled hollow-core photonic crystal fibers. *J. Opt. Soc. Am. B*, 28(12):A11–A26, 2011.

[55] M. Nurhuda, A. Suda, S. Bohman, S. Yamaguchi, and K. Midorikawa. Optical pulse compression of ultrashort laser pulses in an argon-filled planar waveguide. *Phys. Rev. Lett.*, 97:153902, 2006.

[56] J. Chen, A. Suda, E. J. Takahashi, M. Nurhuda, and K. Midorikawa. Compression of intense ultrashort laser pulses in a gas-filled planar waveguide. *Opt. Lett.*, 33(24):2992–2994, 2008.

[57] J. Schulte, T. Sartorius, J. Weitenberg, A. Vernaleken, and P. Russbueldt. Nonlinear pulse compression in a multi-pass cell. *Opt. Lett.*, 41(19):4511–4514, 2016.

[58] M. Hanna, X. Délen, L. Lavenu, F. Guichard, Y. Zaouter, F. Druon, and P. Georges. Nonlinear temporal compression in multipass cells: theory. *J. Opt. Soc. Am. B*, 34(7):1340–1347, 2017.

[59] L. Lavenu, M. Natile, F. Guichard, Y. Zaouter, X. Delen, M. Hanna, E. Mottay, and P. Georges. Nonlinear pulse compression based on a gas-filled multipass cell. *Opt. Lett.*, 43(10):2252–2255, 2018.

[60] P. E. Ciddor. Refractive index of air: new equations for the visible and near infrared. *Appl. Opt.*, 35(9):1566–1573, 1996.

[61] C. Mansfield and E. Peck. Dispersion of helium. *J. Opt. Soc. Am.*, 59(2):199–203, 1969.

[62] A. Bideau-Mehu, Y. Guern, R. Abjean, and A. Johannin-Gilles. Measurement of refractive indices of neon, argon, krypton and xenon in the 253.7-140.4 nm wavelength range. Dispersion relations and estimated oscillator strengths of the resonance lines. *Journal of Quantitative Spectroscopy and Radiative Transfer*, 25 (5):395–402, 1981.

[63] C.Z. Tan. Determination of refractive index of silica glass for infrared wavelengths by ir spectroscopy. *Journal of Non-Crystalline Solids*, 223(1):158–163, 1998.

[64] E. A. J. Marcatili and R. A. Schmeltzer. Hollow metallic and dielectric waveguides for long distance optical transmission and lasers. *Bell System Technical Journal*, 43(4):1783–1809, 1964.

[65] M. Nisoli, S. De Silvestri, and O. Svelto. Generation of high energy 10 fs pulses by a new pulse compression technique. *Applied Physics Letters*, 68(20):2793–2795, 1996.

[66] B. E. A. Saleh and M. C. Teich. *Fundamentals of photonics; 2nd ed.* Wiley, New York, NY, 2007.

[67] H. Liang, P. Krogen, R. Grynko, O. Novak, C.-L. Chang, G. J. Stein, D. Weerawarne, B. Shim, F. X. Kärtner, and K.-H. Hong. Three-octave-spanning supercontinuum generation and sub-two-cycle self-compression of mid-infrared filaments in dielectrics. *Opt. Lett.*, 40(6):1069–1072, 2015.

[68] M. Mlejnek, M. Kolesik, J. V. Moloney, and E. M. Wright. Optically turbulent femtosecond light guide in air. *Phys. Rev. Lett.*, 83:2938–2941, 1999.

[69] F. Courvoisier, V. Boutou, J. Kasparian, E. Salmon, G. Méjean, J. Yu, and J.-P. Wolf. Ultraintense light filaments transmitted through clouds. *Applied Physics Letters*, 83(2):213–215, 2003.

[70] K.G. Makris, Z. Musslimani, D.N. Christodoulides, and S. Rotter. Constant-intensity waves and their modulation instability in non-hermitian potentials. *Nature communications*, 6:7257, 2015.

[71] A. Braun, G. Korn, X. Liu, D. Du, J. Squier, and G. Mourou. Self-channeling of high-peak-power femtosecond laser pulses in air. *Opt. Lett.*, 20(1):73–75, 1995.

[72] F. DeMartini, C. H. Townes, T. K. Gustafson, and P. L. Kelley. Self-steepening of light pulses. *Phys. Rev.*, 164:312–323, 1967.

[73] S. C. Rae and K. Burnett. Detailed simulations of plasma-induced spectral blueshifting. *Phys. Rev. A*, 46:1084–1090, 1992.

[74] M. Mlejnek, E. M. Wright, and J. V. Moloney. Dynamic spatial replenishment of femtosecond pulses propagating in air. *Opt. Lett.*, 23(5):382–384, 1998.

[75] M. Mlejnek, E.M. Wright, and J.V. Moloney. Power dependence of dynamic spatial replenishment of femtosecond pulses propagating in air. *Opt. Express*, 4 (7):223–228, 1999.

[76] D.J. Kane and R. Trebino. Characterization of arbitrary femtosecond pulses using frequency-resolved optical gating. *IEEE Journal of Quantum Electronics*, 29(2):571–579, 1993.

[77] R. Trebino and D. J. Kane. Using phase retrieval to measure the intensity and phase of ultrashort pulses: frequency-resolved optical gating. *J. Opt. Soc. Am. A*, 10(5):1101–1111, 1993.

[78] R. Trebino, K.W. DeLong, D N. Fittinghoff, J. N. Sweetser, M.A. Krumbügel, B.A. Richman, and D.J. Kane. Measuring ultrashort laser pulses in the time-frequency domain using frequency-resolved optical gating. *Review of Scientific Instruments*, 68(9):3277–3295, 1997.

[79] K.W. DeLong, D.N. Fittinghoff, R. Trebino, B. Kohler, and K. Wilson. Pulse retrieval in frequency-resolved optical gating based on the method of generalized projections. *Opt. Lett.*, 19(24):2152–2154, 1994.

[80] C. Iaconis and I. A. Walmsley. Spectral phase interferometry for direct electric-field reconstruction of ultrashort optical pulses. *Opt. Lett.*, 23(10):792–794, 1998.

[81] V.V. Lozovoy, I. Pastirk, and M. Dantus. Multiphoton intrapulse interference. iv. ultrashort laser pulse spectral phase characterization and compensation. *Opt. Lett.*, 29(7):775–777, 2004.

[82] M. Miranda, T. Fordell, C. L. Arnold, A. L'Huillier, and H. Crespo. Simultaneous compression and characterization of ultrashort laser pulses using chirped mirrors and glass wedges. *Opt. Express*, 20(1):688–697, 2012.

[83] M. Miranda, C. L. Arnold, T. Fordell, F. Silva, B. Alonso, R. Weigand, A. L'Huillier, and H. Crespo. Characterization of broadband few-cycle laser pulses with the d-scan technique. *Opt. Express*, 20(17):18732–18743, 2012.

[84] F. Silva, M. Miranda, S. Teichmann, M. Baudisch, M. Massicotte, F. Koppens, J. Biegert, and H. Crespo. Pulse measurement from near to mid-ir using third harmonic generation dispersion scan in multilayer graphene. In *2013 Conference on Lasers Electro-Optics Europe International Quantum Electronics Conference CLEO EUROPE/IQEC*, pages 1–1, 2013.

[85] M. Hoffmann, T. Nagy, T. Willemsen, M. Jupé, D. Ristau, and U. Morgner. Pulse characterization by thg d-scan in absorbing nonlinear media. *Opt. Express*, 22(5):5234–5240, 2014.

[86] A. Tajalli, B. Chanteau, M. Kretschmar, H..G. Kurz, D. Zuber, M. Kovačev, U. Morgner, and T. Nagy. Few-cycle optical pulse characterization via cross-polarized wave generation dispersion scan technique. *Opt. Lett.*, 41(22):5246–5249, 2016.

[87] A. Tajalli, T. K. Kalousdian, M. Kretschmar, S. Kleinert, U. Morgner, and T. Nagy. Full characterization of 8 fs deep uv pulses via a dispersion scan. *Opt. Lett.*, 44(10):2498–2501, 2019.

[88] M. Canhota, F. Silva, R. Weigand, and H.M. Crespo. Inline self-diffraction dispersion-scan of over octave-spanning pulses in the single-cycle regime. *Opt. Lett.*, 42(15):3048–3051, 2017.

[89] J. A. Nelder and R. Mead. A simplex method for function minimization. *The computer journal*, 7(4):308–313, 1965.

[90] I. Sytcevich, C. Guo, S. Mikaelsson, J. Vogelsang, A.-L. Viotti, B. Alonso, R. Romero, P. T. Guerreiro, Í. J. Sola, A. L'Huillier, H. Crespo, M. Miranda, and C. L. Arnold. Characterizing ultrashort laser pulses with second harmonic dispersion scans. *J. Opt. Soc. Am. B*, 38(5):1546–1555, 2021.

[91] D. Fabris, W. Holgado, F. Silva, T. Witting, J. W. G. Tisch, and H. Crespo. Single-shot implementation of dispersion-scan for the characterization of ultrashort laser pulses. *Opt. Express*, 23(25):32803–32808, 2015.

[92] M. Rhodes, Z. Guang, and R. Trebino. Spatiotemporal coupling effects in ultrashort pulses and their visualization. In *Real-time Measurements, Rogue Phenomena, and Single-Shot Applications II*, volume 10089, pages 87 – 93. International Society for Optics and Photonics, SPIE, 2017.

[93] S. Akturk, X. Gu, P. Bowlan, and R. Trebino. Spatio-temporal couplings in ultrashort laser pulses. *Journal of Optics*, 12(9):093001, 2010.

[94] G. Pariente, V. Gallet, A. Borot, O. Gobert, and F. Quéré. Space–time characterization of ultra-intense femtosecond laser beams. *Nature Photonics*, 10, 07 2016.

[95] A. Borot and F. Quéré. Spatio-spectral metrology at focus of ultrashort lasers: a phase-retrieval approach. *Opt. Express*, 26(20), 2018.

[96] P. Gabolde and R. Trebino. Single-shot measurement of the full spatio-temporal field of ultrashort pulses with multi-spectral digital holography. *Opt. Express*, 14 (23), 2006.

[97] M. Miranda, M. Kotur, P. Rudawski, C. Guo, A. Harth, A. L'Huillier, and C. L. Arnold. Spatiotemporal characterization of ultrashort laser pulses using spatially resolved fourier transform spectrometry. *Opt. Lett.*, 39(17):5142–5145, 2014.

[98] C. D'Amico, A. Houard, M. Franco, B. Prade, A. Mysyrowicz, A. Couairon, and V. T. Tikhonchuk. Conical forward thz emission from femtosecond-laser-beam filamentation in air. *Phys. Rev. Lett.*, 98:235002, 2007.

[99] V.P. Kandidov, O.G. Kosareva, I.S. Golubtsov, W. Liu, A. Becker, N. Akozbek, C.M. Bowden, and S.L. Chin. Self-transformation of a powerful femtosecond

laser pulse into a white-light laser pulse in bulk optical media (or supercontinuum generation). *Applied Physics B*, 77:149, 2003.

[100] D.S. Steingrube, E. Schulz, T. Binhammer, T. Vockerodt, U. Morgner, and M. Kovačev. Generation of high-order harmonics with ultra-short pulses from filamentation. *Opt. Express*, 17(18):16177–16182, 2009.

[101] D.S. Steingrube, E. Schulz, T. Binhammer, M.B. Gaarde, A. Couairon, U. Morgner, and M. Kovačev. High-order harmonic generation directly from a filament. *New Journal of Physics*, 13(4):043022, 2011.

[102] D.S. Steingrube, M. Kretschmar, D. Hoff, E. Schulz, T. Binhammer, P. Hansinger, G.G. Paulus, U. Morgner, and M. Kovačev. Sub-1.5-cycle pulses from a single filament. *Opt. Express*, 20(21):24049–24058, 2012.

[103] S. Tzortzakis, B. Prade, M. Franco, A. Mysyrowicz, S. Hüller, and P. Mora. Femtosecond laser-guided electric discharge in air. *Phys. Rev. E*, 64:057401, 2001.

[104] J. Kasparian, M. Rodriguez, G. Méjean, J. Yu, E. Salmon, H. Wille, R. Bourayou, S. Frey, Y.-B. André, A. Mysyrowicz, R. Sauerbrey, J.-P. Wolf, and L. Wöste. White-light filaments for atmospheric analysis. *Science*, 301(5629): 61–64, 2003.

[105] E. Schulz, D. S. Steingrube, T. Binhammer, M. B. Gaarde, A. Couairon, U. Morgner, and M. Kovačev. Tracking spectral shapes and temporal dynamics along a femtosecond filament. *Opt. Express*, 19(20):19495–19507, 2011.

[106] M. Kolesik, J. V. Moloney, and M. Mlejnek. Unidirectional optical pulse propagation equation. *Phys. Rev. Lett.*, 89:283902, 2002.

[107] J. M. Brown, A. Couairon, P. Polynkin, and M. B. Gaarde. Analysis of the angular spectrum for ultrashort laser pulses. *J. Opt. Soc. Am. B*, 36(2):A105–A111, 2019.

[108] J.M. Dahlström, D. Guénot, K. Klünder, M. Gisselbrecht, J. Mauritsson, A. L'Huillier, A. Maquet, and R. Taïeb. Theory of attosecond delays in laser-assisted photoionization. *Chemical Physics*, 414:53–64, 2013.

[109] V. Véniard, R. Taïeb, and A. Maquet. Phase dependence of (N+1)-color (N>1) ir-uv photoionization of atoms with higher harmonics. *Phys. Rev. A*, 54:721–728, 1996.

[110] M.C. Hettrick, S.A. Flint, and J. Edelstein. Grazing incidence reflection coefficients of rhodium, osmium, platinum, and gold from 50 to 300 Å. *Appl. Opt.*, 24(22):3682–3685, 1985.

[111] A.M. Rijs, E.H.G. Backus, C.A. de Lange, N.P.C. Westwood, and M.H.M. Janssen. 'magnetic bottle' spectrometer as a versatile tool for laser photoelectron spectroscopy. *Journal of Electron Spectroscopy and Related Phenomena*, 112(1):151–162, 2000.

[112] W.H. Richardson. Bayesian-based iterative method of image restoration. *J. Opt. Soc. Am.*, 62(1):55–59, 1972.

[113] L.B. Lucy. An iterative technique for the rectification of observed distributions. *The Astronomical Journal*, 79:745–754, 1974.

[114] A.T.J.B. Eppink and D.H. Parker. Velocity map imaging of ions and electrons using electrostatic lenses: Application in photoelectron and photofragment ion imaging of molecular oxygen. *Review of Scientific Instruments*, 68(9):3477–3484, 1997.

[115] L. Montgomery Smith, D. R. Keefer, and S.I. Sudharsanan. Abel inversion using transform techniques. *Journal of Quantitative Spectroscopy and Radiative Transfer*, 39(5):367–373, 1988.

[116] G. A. Garcia, L. Nahon, and I. Powis. Two-dimensional charged particle image inversion using a polar basis function expansion. *Review of Scientific Instruments*, 75(11):4989–4996, 2004.

[117] J. Cooper and R.N. Zare. Angular distribution of photoelectrons. *The Journal of Chemical Physics*, 48(2):942–943, 1968.

[118] M. J. J. Vrakking. An iterative procedure for the inversion of two-dimensional ion/photoelectron imaging experiments. *Review of Scientific Instruments*, 72(11): 4084–4089, 2001.

[119] L.D. Landau and E.M. Lifshitz. *Quantum Mechanics: Non-Relativistic Theory*. Course of Theoretical Physics. Elsevier Science.

[120] Renate Pazourek, Stefan Nagele, and Joachim Burgdörfer. Attosecond chronoscopy of photoemission. *Rev. Mod. Phys.*, 87:765–802, 2015.

[121] L. Eisenbud. Formal properties of nuclear collisions, PhD thesis. *Princeton University*, 1948.

[122] E.P. Wigner. Lower limit for the energy derivative of the scattering phase shift. *Phys. Rev.*, 98:145–147, 1955.

[123] F.T. Smith. Lifetime matrix in collision theory. *Phys. Rev.*, 118:349–356, 1960.

[124] M. Schultze, M. Fieß, N. Karpowicz, J. Gagnon, M. Korbman, M. Hofstetter, S. Neppl, A. L. Cavalieri, Y. Komninos, Th. Mercouris, C. A. Nicolaides, R. Pazourek, S. Nagele, J. Feist, J. Burgdörfer, A. M. Azzeer, R. Ernstorfer, R. Kienberger, U. Kleineberg, E. Goulielmakis, F. Krausz, and V. S. Yakovlev. Delay in photoemission. *Science*, 328(5986):1658–1662, 2010.

[125] D. Guénot, K. Klünder, C. L. Arnold, D. Kroon, J.M. Dahlström, M. Miranda, T. Fordell, M. Gisselbrecht, P. Johnsson, J. Mauritsson, E. Lindroth, A. Maquet, R. Taïeb, A. L'Huillier, and A.S. Kheifets. Photoemission-time-delay measurements and calculations close to the 3*s*-ionization-cross-section minimum in Ar. *Phys. Rev. A*, 85:053424, 2012.

[126] M. Ossiander, F. Siegrist, V. Shirvanyan, R. Pazourek, A. Sommer, T. Latka, A. Guggenmos, S. Nagele, J. Feist, J. Burgdoerfer, R. Kienberger, and M. Schultze. Attosecond correlation dynamics. *Nature Physics*, 13(3):280–285, 2017.

[127] D. Guénot, D. Kroon, E. Balogh, E.W. Larsen, M. Kotur, M. Miranda, T. Fordell, P. Johnsson, J. Mauritsson, M. Gisselbrecht, K. Varjù, C.L. Arnold, T. Carette, A.S. Kheifets, E. Lindroth, A. L'Huillier, and J.M. Dahlström. Measurements of relative photoemission time delays in noble gas atoms. *Journal of Physics B: Atomic, Molecular and Optical Physics*, 47(24):245602, 2014.

[128] M. Isinger, R.J. Squibb, D. Busto, S. Zhong, A. Harth, D. Kroon, S. Nandi, C.L. Arnold, M. Miranda, J.M. Dahlström, E. Lindroth, R. Feifel, M. Gisselbrecht, and A. L'Huillier. Photoionization in the time and frequency domain. *Science*, 358(6365):893–896, 2017.

[129] J. Vos, L. Cattaneo, S. Patchkovskii, T. Zimmermann, C. Cirelli, M. Lucchini, A. Kheifets, A. S. Landsman, and U. Keller. Orientation-dependent stereo wigner time delay and electron localization in a small molecule. *Science*, 360 (6395):1326–1330, 2018.

[130] A. Chacón and C. Ruiz. Attosecond delay in the molecular photoionization of asymmetric molecules. *Opt. Express*, 26(4):4548–4562, 2018.

[131] I. Jordan, M.Huppert, D. Rattenbacher, M. Peper, D. Jelovina, C. Perry, A. von Conta, A. Schild, and H.J. Wörner. Attosecond spectroscopy of liquid water. *Science*, 369(6506):974–979, 2020.

[132] A. Cavalieri, N. Mueller, T. Uphues, V. Yakovlev, A. Baltuska, B. Horvath, B. Schmidt, L. Blümel, R. Holzwarth, S. Hendel, M. Drescher, U. Kleineberg, P. Echenique, R. Kienberger, F. Krausz, and U. Heinzmann. Attosecond spectroscopy in condensed matter. *Nature*, 449:1029–32, 2007.

[133] M. Ossiander, J. Riemensberger, S. Neppl, M. Mittermair, M. Schaeffer, A. Duensing, M. Wagner, R. Heider, M. Wurzer, M. Gerl, M. Schnitzenbaumer, J. Barth, F. Libisch, C. Lemell, J. Burgdörfer, P. Feulner, and R. Kienberger. Absolute timing of the photoelectric effect. *Nature*, 561, 2018. doi: 10.1038/s41586-018-0503-6.

[134] M. Isinger, D. Busto, S. Mikaelsson, S. Zhong, C. Guo, P. Salières, C. L. Arnold, A. L'Huillier, and M. Gisselbrecht. Accuracy and precision of the RABBIT technique. *Philosophical Transactions of the Royal Society A: Mathematical, Physical and Engineering Sciences*, 377(2145):20170475, 2019.

[135] K.L. Reid. Photoelectron angular distributions: developments in applications to isolated molecular systems. *Molecular Physics*, 110(3):131–147, 2012.

[136] J. Joseph, F. Holzmeier, D. Bresteau, C. Spezzani, T. Ruchon, J.F. Hergott, O. Tcherbakoff, P. D'Oliveira, J.C. Houver, and D. Dowek. Angle-resolved studies of XUV–IR two-photon ionization in the RABBITT scheme. *Journal of Physics B: Atomic, Molecular and Optical Physics*, 53(18):184007, 2020.

[137] J. Fuchs, N. Douguet, S. Donsa, F. Martín, J. Burgdörfer, L. Argenti, L. Cattaneo, and U. Keller. Time delays from one-photon transitions in the continuum. *Optica*, 7(2):154–161, 2020.

[138] J. Peschel, D. Busto, M. Plach, M. Bertolino, M. Hoflund, S. Maclot, J. Vinbladh, H. Wikmark, F. Zapata, E. Lindroth, M. Gisselbrecht, J.M. Dahlström, A. L'Huillier, and P. Eng-Johnsson. Complete characterization of multi-channel single photon ionization, 2021.

[139] J. Vinbladh. Two photon above threshold ionization in a relativistic framework: Attosecond delays in high Z elements, PhD thesis, 2018.

[140] J.W. Cooper. Photoionization from outer atomic subshells. a model study. *Phys. Rev.*, 128:681–693, 1962.

[141] S. Saha, J. Vinbladh, J. Sörngård, A. Ljungdahl, and E. Lindroth. Angular anisotropy parameters for photoionization delays. *Phys. Rev. A*, 104:033108, 2021.

[142] J. Vinbladh, J.M. Dahlström, and E. Lindroth. Many-body calculations of two-photon, two-color matrix elements for attosecond delays. *Phys. Rev. A*, 100:043424, 2019.

[143] D. Busto, J. Vinbladh, S. Zhong, M. Isinger, S. Nandi, S. Maclot, P. Johnsson, M. Gisselbrecht, A. L'Huillier, E. Lindroth, and J.M. Dahlström. Fano's propensity rule in angle-resolved attosecond pump-probe photoionization. *Phys. Rev. Lett.*, 123:133201, 2019.

[144] https://www.nist.gov/pml/atomic-spectra-database.

[145] A. Autuori, D. Platzer, M. Lejman, G. Gallician, L. Maëder, A. Covolo, L. Bosse, M. Dalui, D. Bresteau, J.-F. Hergott, O. Tcherbakoff, H.J.B. Marroux, V. Loriot, F. Lépine, L. Poisson, R. Taïeb, J. Caillat, and P. Salières. Anisotropic dynamics of two-photon ionization: An attosecond movie of photoemission. *Science Advances*, 8(12):eabl7594, 2022.

[146] L. Drescher, T. Witting, O. Kornilov, and M.J.J. Vrakking. Phase dependence of resonant and antiresonant two-photon excitations. *Phys. Rev. A*, 105:L011101, 2022.

[147] E. Escoto, A. Tajalli, T. Nagy, and G. Steinmeyer. Advanced phase retrieval for dispersion scan: a comparative study. *J. Opt. Soc. Am. B*, 35(1):8–19, 2018.

[148] N.C. Geib, R. Hollinger, E. Haddad, P. Herrmann, F. Légaré, T. Pertsch, C. Spielmann, M. Zürch, and F. Eilenberger. Discrete dispersion scan setup for measuring few-cycle laser pulses in the mid-infrared. *Opt. Lett.*, 45(18):5295–5298, 2020.

[149] B. Alonso, Í. Sola, and H. Crespo. Self-calibrating d-scan: Measuring ultrashort laser pulses on-target using an arbitrary pulse compressor. *Scientific Reports*, 8, 2018.

[150] S. Kleinert, A. Tajalli, T. Nagy, and U. Morgner. Rapid phase retrieval of ultrashort pulses from dispersion scan traces using deep neural networks. *Opt. Lett.*, 44(4):979–982, 2019.

[151] B. Alonso, S. Torres-Peiró, R. Romero, P.T. Guerreiro, A. Almagro-Ruiz, H. Muñoz Marco, P. Pérez-Millán, and H. Crespo. Detection and elimination of pulse train instabilities in broadband fibre lasers using dispersion scan. *Scientific Reports*, 10, 2020.

[152] A.-L. Viotti, M. Seidel, E. Escoto, S. Rajhans, W.P. Leemans, I. Hartl, and C.M. Heyl. Multi-pass cells for post-compression of ultrashort laser pulses. *Optica*, 9 (2):197–216, 2022.

[153] P. Balla, A. Bin Wahid, I. Sytcevich, C. Guo, A.-L. Viotti, L. Silletti, A. Cartella, S. Alisauskas, H. Tavakol, U. Grosse-Wortmann, A. Schönberg, M. Seidel, A. Trabattoni, B. Manschwetus, T. Lang, F. Calegari, A. Couairon, A. L'Huillier, C.L. Arnold, I. Hartl, and C.M. Heyl. Postcompression of picosecond pulses into the few-cycle regime. *Opt. Lett.*, 45(9):2572–2575, 2020.

Scientific publications

Author contributions

Article I: Fast iterative retrieval algorithm for ultrashort pulse characterization using dispersion scans

In this article we propose a novel, fast iterative algorithm for ultrashort pulse characterisation using dispersion scan. The performance of the algorithm is demonstrated for the retrieval of d-scan traces of pulses from an OPCPA, as well as pulses from a hollow core fibre.

I participated to the design and optimisation of the HCF setup, as well as the measurements performed for this publication. I contributed to the writing of the manuscript through discussions and feedback.

Article II: Compact single-shot d-scan setup for the characterization of few-cycle laser pulses

This article presents a new scheme for single-shot d-scan measurements, significantly more compact compared to its predecessors. The design is based on a deliberate introduction of strong astigmatism into the beam, which allows us to image the output of the SHG crystal in one direction while focusing it in the other direction.

I participated to the assembling of the d-scan setup and the imaging spectrometer, as well as the experimental work on testing the assembly. I contributed to the writing of the manuscript through discussions and feedback.

Article III: All-optical measurement of the complete waveform of octave-spanning ultrashort light pulses

In this work we present a d-scan-based technique for measuring the complete electric field of octave-spanning ultrashort pulses. We verify its validity using pulses from a hollow-core fibre compressor at the University of Porto, Portugal.

I took part in setting up the d-scan and performing the experiment. I contributed to the writing of the manuscript through discussions and feedback.

Article IV: Attosecond timing of electron emission from a molecular shape resonance

This article uses the RABBIT scheme to study the changes of the centrifugal barrier sustaining a shape resonance in valence-ionised N_2, induced by nuclear motion. We record a bond lengthening of 2%, which delays the escaping electron by as much as 200 attoseconds, demonstrating a limit of the Franck-Condon principle.

I took part in the experimental work and contributed to the writing of the manuscript through feedback.

Article V: Attosecond electron–spin dynamics in Xe 4d photoionization

In this work we study the dynamics of Xe 4d photoionisation by combining RABBIT and the coincidence technique. We use time-frequency analysis to identify two interfering ionisation mechanisms: the broad giant dipole resonance, and a narrow resonance induced by spin-flip transitions.

I took part in the experiments and participated to the writing of the manuscript through feedback.

Article VI: Attosecond photoionization dynamics in the vicinity of the Cooper minima in argon

We use rainbow-RABBIT to measure photoionisation time delays between the 3s and 3p subshells of argon over a large 34-eV energy range covering the Cooper minima in each subshell. Our calculations include the strong shake-up channels producing photoelectrons that overlap with the ones from the 3s subshell, securing a good agreement with the experiment.

I took a large role in data acquisition and analysis. I contributed to the discussions about data interpretation and the writing of the manuscript.

Article VII: 4D spatio-temporal characterization of ultrashort light pulses undergoing filamentation (submitted manuscript)

In this article we present a method capable of characterising the complete 3D electric field of pulses driving filamentation, with the additional possibility to extract pulses at virtually any position within the filament. The proposed technique is tested against a sample filament, demonstrating access to information in spatial, temporal, spectral, as well as $k_\perp$ domains, and compared to simulations for macroscopic validation.

I had a leading role in this study. I participated to the design of the experimental setup, helped build the d-scan part, and personally built and tested all other parts except the spatio-temporal interferometer. Together with another student, I performed the data acquisition and analysis. I did most of the data interpretation, and wrote large parts of the manuscript with the help of my main supervisor.

Article VIII: Resonant two-photon ionisation of helium atoms studied by attosecond interferometry (manuscript in preparation)

We study resonant two-photon ionisation of helium via the 1s3p, 1s4p, and 1s5p resonant states. We perform angle-resolved measurements using a VMIS, as well as high-spectral-resolution MBES measurements to disentangle the interplay between the *s* and *d* ionisation channels in the case of the 4p state. We use a theoretical model to interpret the physical meaning of the experimental results.

I had the leading role in this study. I took the experimental data together with my team. I analysed the VMIS data and led the theoretical interpretation of all data with the help of a postdoc and my assistant supervisor. I wrote parts of the manuscript.

Printed by Media-Tryck, Lund 2022 NORDIC SWAN ECOLABEL 3041 0903

LUND UNIVERSITY
Faculty of Engineering, LTH
Department of Physics
Division of Atomic Physics

ISBN 978-91-8039-274-7
ISSN 0281-2762
Lund Reports on Atomic Physics, LRAP 582 (2022)